# Plasma Instabilities from blazar-induced pair beams propagating through IGM

## Particle-in-Cell Simulations

DISSERTATION

zur Erlangung des akademischen Grades
Doktor der Naturwissenschaften
(Dr. rer. nat.)
in der Wissenschaftsdisziplin Theoretische
Astroteilchenphysik

eingereicht an der
Mathematisch-Naturwissenschaftlichen Fakultät
der Universität Potsdam

von

IMAN RAFIGHI

Potsdam, 02.10.2018

Hauptbetreuer: Prof. Martin Pohl
weitere Gutachter: Prof. Dieter Horns & Prof. Christoph Pfrommer

I would like to dedicate this thesis to my loving wife …

# Declaration

I hereby declare that except where specific reference is made to the work of others, the contents of this dissertation are original and have not been submitted in whole or in part for consideration for any other degree or qualification in this, or any other university. This dissertation is my own work and contains nothing which is the outcome of work done in collaboration with others, except as specified in the text and Acknowledgements.

October 2018

# Table of contents

**List of figures** **vii**

**List of tables** **xi**

**1 Introduction** **1**

**2 Background** **3**

2.1 Blazars . . . . . . . . . . . . . . . . . . . . . . . . . . . . . 3

2.2 Cosmic voids and intergalactic medium . . . . . . . . . . . . . . . . . 6

2.3 Cosmic microwave background . . . . . . . . . . . . . . . . . . . . . 8

2.4 Extragalactic background light . . . . . . . . . . . . . . . . . . . . . 10

2.5 Blazar-induced pair beams . . . . . . . . . . . . . . . . . . . . . . . 11

2.6 Relevant plasma instabilities . . . . . . . . . . . . . . . . . . . . . . 13

**3 Analytical model** **15**

3.1 Kinetic representation . . . . . . . . . . . . . . . . . . . . . . . . 16

3.2 Linear Landau damping . . . . . . . . . . . . . . . . . . . . . . . . 21

3.3 Overview of relevant plasma studies . . . . . . . . . . . . . . . . . . 23

3.3.1 Reactive vs Kinetic regime . . . . . . . . . . . . . . . . . . . 23

3.4 Monoenergetic pair beams . . . . . . . . . . . . . . . . . . . . . . . 24

3.4.1 The electrostatic instability . . . . . . . . . . . . . . . . . . . 24

3.4.2 Weibel mode . . . . . . . . . . . . . . . . . . . . . . . . . . 26

3.5 The electrostatic instability for realistic pair beams . . . . . . . . . . . 30

3.5.1 Linear growth rate . . . . . . . . . . . . . . . . . . . . . . . 30

3.5.2 Electrostatic instability for a beam without perpendicular momentum spread . . . . . . . . . . . . . . . . . . . . . . . . . . . 31

3.5.3 Electrostatic instability for a beam with a finite perpendicular momentum spread . . . . . . . . . . . . . . . . . . . . . . . . . 32

**4 Particle-in-Cell Plasma Simulations 37**
- 4.1 Plasma Simulations Models . . . . . 37
- 4.2 The Principles of Particle-in-Cell Simulations . . . . . 38
  - 4.2.1 Core collisionless algorithm . . . . . 39
- 4.3 Particle-in-Cell Simulations with EPOCH . . . . . 44
  - 4.3.1 Features of EPOCH . . . . . 45
  - 4.3.2 EPOCH Characteristics . . . . . 45
  - 4.3.3 Our modifcation to EPOCH . . . . . 49
  - 4.3.4 Technical Investigations . . . . . 49

**5 Simulations 57**
- 5.1 Monoenergitc beam simulations . . . . . 57
  - 5.1.1 Condition for the kinetic regime . . . . . 58
  - 5.1.2 Choice of parameters for PIC simulations . . . . . 58
  - 5.1.3 The simulation setup . . . . . 61
  - 5.1.4 Discussion of simulation results . . . . . 63
  - 5.1.5 Summary . . . . . 75
- 5.2 The electrostatic instability for realistic pair beams . . . . . 76
  - 5.2.1 Choice of parameters . . . . . 76
  - 5.2.2 Simulation setup . . . . . 77
  - 5.2.3 Simulations . . . . . 80
  - 5.2.4 Summary . . . . . 88

**6 Summary and conclusions 89**

**References 93**

**Appendix A Appendix for monoenergetic beams 103**
- A.1 Derivation of the dispersion equation for $p_{\perp,b} = p_{\|,p} = p_{\perp,p} = 0$ and $k_{\|} = 0$ 103
- A.2 Derivation of the dispersion equation for $p_{\|,b} = 0$ and $k_{\|} = 0$ . . . . . 104
- A.3 Approximation for $\alpha_{kin}$ at large values of $\mu_R$ . . . . . 105

**Appendix B Realistic pair beams 107**
- B.1 Realistic pair spectrum . . . . . 107
- B.2 Approximation for the stellar radiation spectrum at redshift 0.2 . . . . . 111
- B.3 Approximation for the pair distribution function . . . . . 112

**Publications 113**

# List of figures

2.1 Sketches of the unified AGN model. . . . . . . . . . . . . . . . . . . . . . . . 4
2.2 Growth of sources at high-energy $\gamma$ rays. . . . . . . . . . . . . . . . . . . . 5
2.3 N-body simulation Millennium. . . . . . . . . . . . . . . . . . . . . . . . . 7
2.4 Map of cosmic microwave background temperature. . . . . . . . . . . . . . . 9
2.5 EBL intensity measurements. . . . . . . . . . . . . . . . . . . . . . . . . . 10
2.6 Cascade emission from a TeV blazar and Fermi upper limits. . . . . . . . . 12
2.7 A Sketch of the filamentation, two-stream, oblique and Weibel modes. . . . 13

3.1 A Sketch of the resonant and non-resonant particles. . . . . . . . . . . . . . 21
3.2 Schematic representations of the cold and waterbag distribution functions. . 26
3.3 Growth rate of the electrostatic instability for parallel wave vectors for beam with no angular spread and distribution function that was determined by Vafin et al. (2018) (equation B.13, red line) and Schlickeiser et al. (2012a) (equation B.14, black line), respectively. . . . . . . . . . . . . . . . . . . . 33
3.4 (a) Normalized growth rate, $\omega_i/(\pi\omega_p(n_b/n_p))$, for a beam with no angular spread and the distribution function from equation (B.14) (Schlickeiser et al. (2012a), $M_c = 2\times10^6$, $\tau_0 = 10^3$, $\alpha = 1.8$). (b) Same as in (a), but for a beam with no angular spread and a distribution function derived by us (equation B.13). . . . . . . . . . . . . . . . . . . . . . . . . . . . . 34
3.5 (a) Normalized growth rate, $\omega_i/(\pi\omega_p(n_b/n_p))$, for a beam with a finite angular spread and the distribution function of equation (B.14). (b) Same as for (a), but for the distribution function of equation (B.13) determined by us. 34

4.1 Block diagram of the core routines in a PIC code. . . . . . . . . . . . . . . 39
4.2 Shape functions. . . . . . . . . . . . . . . . . . . . . . . . . . . . . . . . 41
4.3 Schematic illustration of the 3D Yee grid . . . . . . . . . . . . . . . . . . . 42
4.4 Schematic illustration of the leapfrog integration method . . . . . . . . . . 43
4.5 Illustration of the 2D Yee grid . . . . . . . . . . . . . . . . . . . . . . . . 46

4.6 Analytic dispersion curves for (a) 2nd order schemes. (b) 4th order schemes (c) 6th order schemes. . . . . . . . . . . . . . . . . . . . . . . . . . . . 52
4.7 2D Fourier spectra of the electric field illustrating the artificial cherenkov radiation. . . . . . . . . . . . . . . . . . . . . . . . . . . . . . . . . . 53

5.1 Function $\alpha_{kin}(\Gamma)$: dashed dotted black line $\mu_R = 2.5$; dashed black line $\mu_R = 10$; dotted black line $\mu_R = 100$. Function $\alpha_\varepsilon(\Gamma)$: green line $k_B T_p/(m_e c^2) = 4 \times 10^{-3}$; red line $k_B T_p/(m_e c^2) = 10^{-4}$; blue line $k_B T_p/(m_e c^2) = 10^{-5}$; brown line $k_B T_p/(m_e c^2) = 10^{-6}$. The black point illustrates the parameters chosen for simulation run 1 that satisfies all criteria. . . . . . . . . . . . 59
5.2 Dependence of all three constraints on the beam Lorentz factor. The green line represents $\alpha_{kin}$, the red line $\alpha_\varepsilon$, and the blue line $\alpha_W$. $\mu_R = 2.5$, $k_B T_p/(m_e c^2) = 4 \times 10^{-4}$. The black dot indicates parameter values of run 2. 60
5.3 Same as figure 5.2, but for $\mu_R = 10$, $k_B T_p/(m_e c^2) = 4 \times 10^{-3}$. The black dot indicates parameter values of run 3. . . . . . . . . . . . . . . . . . . . . . . 60
5.4 Same as figure 5.2, but for $\mu_R = 10$, $k_B T_p/(m_e c^2) = 10^{-3}$. The black dot indicates parameter values of run 4. . . . . . . . . . . . . . . . . . . . . . . 61
5.5 Panels(a)-(c) 2D plot of the electric field $E_x$ for three different plasma times of $\omega_{pe}t = 488, 4222, 16238$ in units of $\omega_{p,e} c m_e/e$, (d): 2D plot of the transverse magnetic field $B_z$ at $\omega_{pe}t = 16238$ in units of $\omega_{p,e} m_e/e$ for run 1. . . . . . . 64
5.6 Figure (a):Two-dimensional Fourier spectrum of $\mathbf{E} \parallel \mathbf{k}$ at $\omega_{pe}t = 4222$ in units of $\omega_{p,e} c m_e/e$, Figure (b): Time evolution of the energy densities of electric and magnetic field, respectively, in SI units for run 1. . . . . . . . . 65
5.7 Beam momentum distribution for run 1 at two points in time: (a) for $p_x$, (b) for $p_y$. . . . . . . . . . . . . . . . . . . . . . . . . . . . . . . . . . . . 66
5.8 Figure (a):Two-dimensional Fourier spectrum of $\mathbf{E} \parallel \mathbf{k}$ at $\omega_{pe}t = 5036$ in units of $\omega_{p,e} c m_e/e$, Figure (b): Time evolution of the energy densities of electric and magnetic field, respectively, in SI units for run 2. . . . . . . . . 68
5.9 Panels(a)-(c) 2D plot of the electric field $E_x$ for three different plasma times of $\omega_{pe}t = 564, 4025, 10714$ in units of $\omega_{p,e} c m_e/e$, (d): 2D plot of the transverse magnetic field $B_z$ at $\omega_{pe}t = 10714$ in units of $\omega_{p,e} m_e/e$ for Run3. . . . . . . 69
5.10 Figure (a):Two-dimensional Fourier spectrum of $\mathbf{E} \parallel \mathbf{k}$ at $\omega_{pe}t = 2448$ in units of $\omega_{p,e} c m_e/e$, Figure (b): time evolution of the energy densities of electric and magnetic field, respectively, in SI units for run 3. . . . . . . . . 70
5.11 Beam momentum distribution in $p_y$ for run 3 at two points in time. . . . . 71
5.12 Time evolution of the momentum spread of the beam, $p_{\mathrm{rms}}$, for run 3. . . . 71

5.13 Panels(a)-(c) 2D plot of the electric field $E_x$ for three different plasma times of $\omega_{pe}t = 256, 985, 2187$ in units of $\omega_{p,e}cm_e/e$, (d): 2D plot of the transverse magnetic field $B_z$ at $\omega_{pe}t = 2187$ in units of $\omega_{p,e}m_e/e$ for Run 4. . . . . . . 72
5.14 Figure (a):Two-dimensional Fourier spectrum of $\mathbf{E} \parallel \mathbf{k}$ at $\omega_{pe}t = 401$ in units of $\omega_{p,e}cm_e/e$, Figure (b): Time evolution of the energy densities of electric and magnetic field, respectively, in SI units for run 4. . . . . . . . . . . . . 73
5.15 Momentum distribution for run 4 at two points in time: (a) for $p_x$ of IGM, (b) for $p_y$ of Beam. . . . . . . . . . . . . . . . . . . . . . . . . . . . . 74
5.16 Time evolution of the momentum spread of the beam, $p_{\rm rms}$, for run 4. . . . 74
5.17 Composite beam distribution function used for PIC simulations. Red: beam 1 ($T_b = 200$ keV, $\Gamma_1 = 5$, $w_1 = 0.9$). Green: beam 2 ($T_b = 200$ keV, $\Gamma_2 = 20$, $w_2 = 0.1$). Black: the total distribution. . . . . . . . . . . . . . . . . . . . . . 78
5.18 Normalized growth rate, $\omega_i/(\pi\omega_p(n_b/n_p))$, for the composite distribution function used in PIC simulations and displayed in figure 5.17. . . . . . . . 78
5.19 Electric field power spectrum from test runs to check the resolution of grid frequencies for different skin lengths, all other parameters are fixed. . . . . 79
5.20 Time evolution of the energy densities of electric and magnetic field, respectively, in SI units for run 1 (dashed lines) and run 2 (solid lines). . . . . . 80
5.21 (a) Two-dimensional Fourier spectrum of $\mathbf{E} \parallel \mathbf{k}$ (in units $(\omega_{p,e}cm_e/e)^2$) at $\omega_{p}t \approx 10152$ for run 1. (b) The same as (a), but for run 2. . . . . . . . . . . 81

B.1 EBL energy-density spectrum for different models. Blue: the Wien-type distribution used by Schlickeiser et al. (2013); (see also Eq. B.10). Red: stellar radiation model by Finke et al. (2010) at redshift 0.2. Black: our analytical approximation for the red line (Appendix B.2). Magenta: empirical model of the X-ray background (Fabian and Barcons, 1992). . . . . . . . . 110
B.2 Normalized pair spectrum at the distance 50 Mpc from the source. Red: numerical solution of Eq. (B.9) using the Finke model model and the CXB fit. Blue: our approximation for the red curve (Eq. (B.13)). Black: pair spectrum for the EBL approximation by Schlickeiser et al. (2013). . . . . . 111

# List of tables

4.1 Sobol algorithm with the flipping method. . . . . . . . . . . . . . . . . . . . 49
4.2 Test parameters . . . . . . . . . . . . . . . . . . . . . . . . . . . . . . . . 54
4.3 Test parameters . . . . . . . . . . . . . . . . . . . . . . . . . . . . . . . . 55

5.1 Simulation parameters . . . . . . . . . . . . . . . . . . . . . . . . . . . . . 62
5.2 Simulation parameters for composite beams with $\Gamma_1 = 5$ and $\Gamma_2 = 20$. . . . . 80

B.1 Fitting parameters for the approximation Eq. (B.12) . . . . . . . . . . . . . . 111
B.2 Fitting parameters for the approximation Eq. (B.13) . . . . . . . . . . . . . . 112

# Chapter 1

# Introduction

Astroparticle physics is considered a young field of science. It all started when astrophysicists turned their endeavours from traditional astrophysical issues to new phenomena, such as cosmic rays which was brought to the community in the early twentieth century by F. Hess (1912). Modern gamma-ray telescopes, both ground telescopes and satellites, provide the main stream of data for astrophysicists in quest of detecting the sources of gamma rays such as active galactic nuclei (AGN).

Blazars are one of the candidates for the high energy gamma rays. They are a sub-class of active galactic nuclei, i.e. galaxies with an accreting supermassive black hole in which the central core, emits a long jet of relativistic plasma perpendicular to the plane of the accretion disk of the black hole. Many blazars have been detected with gamma-ray telescopes such as HESS, VERITAS, MAGIC and Fermi satellite as sources of gamma-rays with the energy $E \geq 100$ GeV (de Naurois (2015)). Of interest are BL Lac objects with an intrinsic emission spectrum harder than $E^{-2}$ that extends to at least a few TeV, so that the cascade emission falls into the energy band accessible with the *Fermi*-LAT. This leads to a broad pair spectrum ($10^1 < \gamma < 10^8$, where $\gamma$ is the gamma factor of the pairs).

These created pairs are the subject of many investigations, as they can be affected by several physical processes: (i) inverse-Compton scattering (ICS), (ii) deflection by the intergalactic magnetic field (IGMF), or (iii) collective plasma effects. The ICS would result in gamma-ray emission with characteristic energy in the GeV band but as indicated by Fermi-LAT data, the GeV gamma-ray emission is suppressed, meaning that the ICS is not the fastest of the three processes. The effect of deflection by the IGMF has been well investigated by researchers such as Neronov and Semikoz (2009); Neronov and Vovk (2010); Taylor et al. (2011) which has led to its constraints. However, these constraints on the IGMF are valid only under the assumptions that the multi-TeV gamma-ray emission persists on long timescales and that the pairs lose their energy only due to ICS. This latter assumption is crucial and remains debatable.

The importance of collective plasma effects has been pointed out by several authors such as Broderick et al. (2012); Miniati and Elyiv (2013); Schlickeiser et al. (2012b). In fact, the pairs can induce electrostatic and electromagnetic instabilities (Breizman, 1990; Breizman and Riutov, 1974; Bret, 2006; Bret et al., 2004, 2005, 2010; Godfrey et al., 1975; Lominadze and Mikhailovskii, 1979). In this case, wave-particle interactions can reduce the energy of the pairs by 30-50 % as discussed by Bret et al. (2010); Schlickeiser (2010); Schlickeiser et al. (2002). Therefore, the collective plasma effects can also substantially suppress the GeV-band gamma-ray emission affecting as well the IGMF constraints.

Using Particle in cell (PIC) simulations, we have revisited the issue of plasma instabilities induced by electron-positron beams in the fully ionized intergalactic medium. This problem is related to pair beams produced by TeV radiation of blazars. The realistic beams cannot be simulated, because the density ratio is too small. To proceed with the problem, we find different parameters, for which the pair beam can be simulated with the available computational resources and which, at the same time, preserve the underlying physics of the realistic pair-beams. The main objective of our study is to clarify the feedback of the beam-driven instabilities on the pairs. The parameters of the simulated beam-plasma system provide an adequate physical picture that can be extrapolated to realistic blazar-induced pairs. The issue of finding the proper parameters which can be simulated is considered in sections 3.4 and 5.1 for the case of a mono-energetic pair-beam distribution, whereas the realistic pair-beam distribution is highly non- monoenergetic. The analytical models for the latter case are presented in section 3.5 and the relevant simulations are discussed in section 5.2. Then we pursued with our studies accounting for a realistic energy distribution to clarify its impact on the nonlinear beam evolution.

In the following chapters, an introduction of the relevant literature is presented in chapter 2. In chapter 3, an introduction of analytical works of others is discussed and followed by our new analytical model of the beam, both for the case of monoenergetic and a realistic wide beam. In chapter 4, the simulation method of PIC is introduced. Later on, we discuss the technical issues and code modifications we did for a realistic simulation based on our needs of the mode. Then it is followed by the analytical models being investigated via PIC simulations in 2-dimensional simulation box in chapter 5. Ultimately the summary and conclusions are presented in chapter 6.

# Chapter 2

# Background

In following sections a brief introduction to blazars, intergalactic medium and pair beam production is presented.

## 2.1 Blazars

Blazars are powerful sources of electromagnetic radiation in the distant universe, ranging up to the highest energies i.e TeV band. They are a class of radio loud active galactic nuclei with an emitting jet along the line of sight to the observer.

About 3% of all galaxies have a core, or nucleus emitting a very bright jet in central region which can be characterised as AGN (see figure 2.1a). An important feature of their intense emission is the fact that its electromagnetic spectrum ranges from the radio up to the highest energy gamma rays.

A wide range of pictures for AGN exits. One could refer to the observed spectral range, its emission line properties and its luminosity. We can also categorize them as radio loud or radio quiet:

- The **Radio loud AGNs** show large-scale vertical and highly relativistic jets from the center of the galaxy, which can travel up to Megaparsec scales. Where $V_{jet} > 0.7c$ and $\Gamma > 1$ ( see, Schlickeiser (2002)).
- The **Radio quite AGNs** have no visible jet structure and for reasons which are justified below, we will not consider them in this work.

In 1995 the “unified AGN picture” was proposed by Urry and Padovani (1995), based on the orientation of the active galaxy with respect to the observer on Earth. This implies

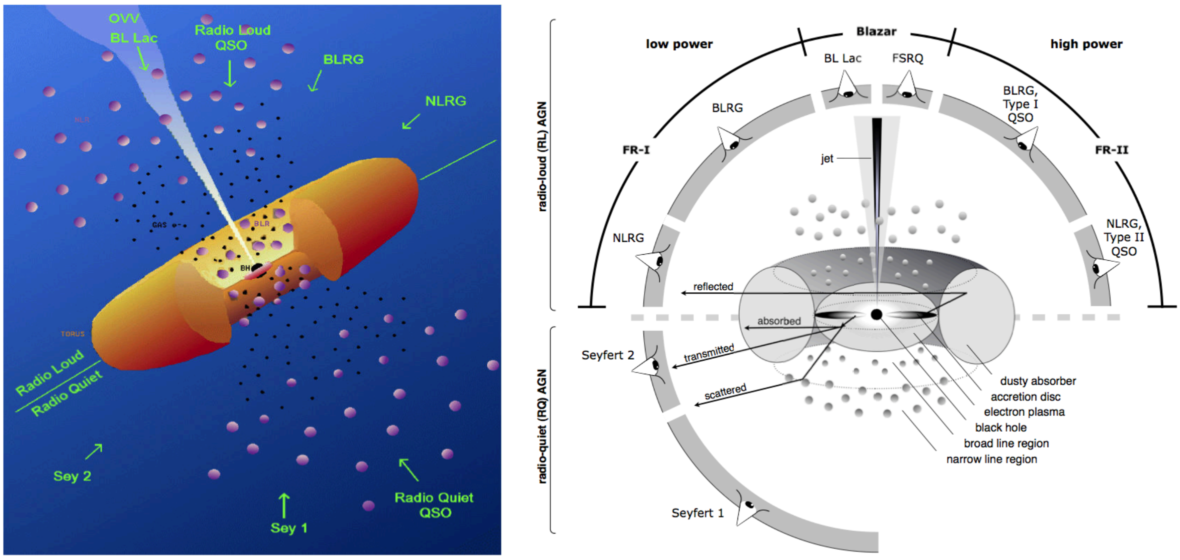

(a) (b)

Fig. 2.1 Sketches of the unified AGN model. Figure (a) taken from Urry and Padovani (1995), Figure (b) taken from Beckmann and Shrader (2013).

that most AGNs are not classified as blazars to observer on Earth. The sketch in figure 2.1b represents different observational properties.

AGN consists of a host galaxy with a central supermassive black hole with masses of the order of $10^8 - 10^{10} M_\odot$ which converts the potential energy of matter in an accretion process to radiation and particle outflow. The system is surrounded by an accretion disk of ionized gas. Further out, the system is surrounded by an extended molecular torus, containing fast moving gas clouds. This results in broad line emission, also the so-called narrow line regions consisting of slower gas clouds. There are still many open issues on the topic (Beckmann and Shrader (2013)). Until 1991 with Compton Gamma Ray Observatory (CGRO), five gamma ray emitting AGNs were observed. (Bassani and Dean (1983)). Four of them are with energies up to KeV while only the quasar 3C 273 was detected at $\geq 35 MeV$.

Within one year of EGRET (Energetic Gamma ray Experiment Telescopepointing) in operation, more than 14 $\gamma$-ray emitting AGN in range of 100 MeV and 5 GeV were found. Summing up to 66 high-confidence and 27 low-confidence detections of blazars by the end of the CGRO mission (see figure 2.2). Meanwhile the ground-based Atmospheric Cherenkov Technique (ACT) (de Naurois and Mazin, 2015) detected Very High Energies $(VHE; \sim 100 GeV)$ of the Crab nebula (Weekes et al. (1989)) and Mrk 421 (Punch et al. (1992)). Collaboration (2015a) presented their studies regarding the high-confidence clean sample of the Third Large Area Telescope Catalog of Active Galactic Nuclei (3LAC). They

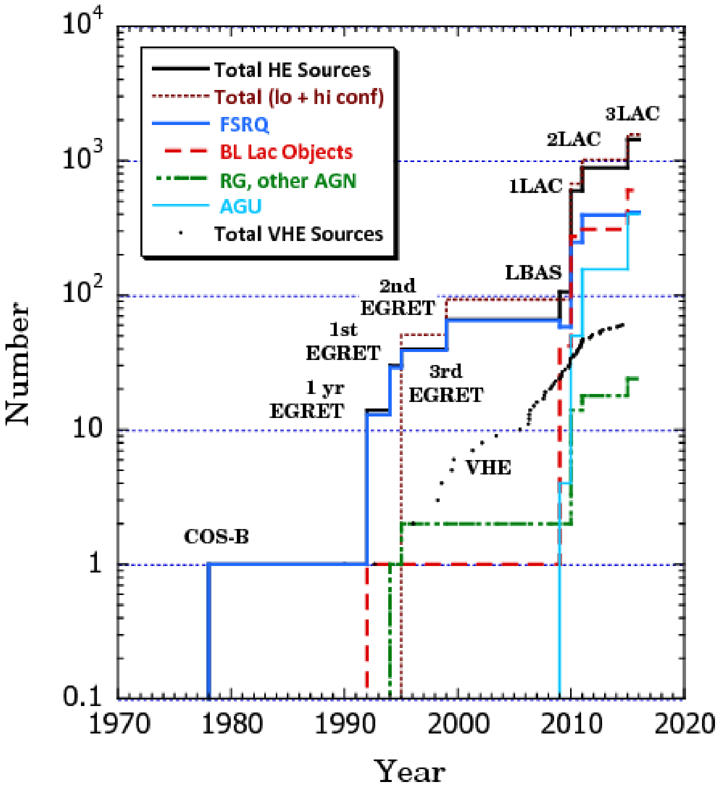

Fig. 2.2 Growth of sources at high-energy (HE), $\gtrsim$ 100 MeV, $\gamma$ rays. The number of sources reported in the different catalogs and lists, as noted in the figure, are from the 1st EGRET Catalog Fichtel et al. (1994); 2nd EGRET Catalog Thompson et al. (1995); 3rd EGRET catalog Hartman et al. (1999) ; LAT Bright AGN Sample (LBAS) Abdo et al. (2009), First LAT AGN Catalog (1LAC) Abdo (2010), 2LAC Collaboration (2011), and the 3LAC Collaboration (2015b). Figure taken from Dermer and Giebels (2016)

used the first four years of the Fermi-LAT data listing 1444 $\gamma$-ray AGNs. The list consists of 30% FSRQ, 40% BL Lacertae objects, 30% blazars of unknown type (weak-lined BL Lac or strong-lined FSRQ). It also consists of 24 non-blazar AGNs which are mainly radio galaxies, radio-loud narrow line Seyfert galaxies and candidate Seyfert AGNs.

About 10% of the AGNs are *radio-loud* with observable collimated radio jets up to megaparsec scales from the galactic center, along the rotation axis of the black hole. The jet is brightest for the observer on earth within an opening angle of $\theta_{jet} \simeq \frac{1}{\Gamma}$, where $\Gamma$ is the Lorentz factor of the jet outflow. The smaller angle cases are namely flat spectrum radio quasars (FSRQ) and BL Lacertae objects (BL Lacs for short). FSRQs emit broad emission lines typical of quasars while BL Lacertae objects are characterized by extremely weak or even absent emission lines in their optical spectra. FSRQs are typically more powerful than

BL Lacs and their radiative output tend to be more dominated by the high-energy emission. BL Lacs are on average with larger energies of the emitted $\gamma$-ray photons and they are in fact the majority of the blazars detected at VHE.

A "double humped" shape is seen in entire electromagnetic spectrum of the smooth SED of blazars. Beamed synchrotron radiation of relativistic $e^{\pm}$ pairs is well understood as the low energy part of the spectrum with a peak between IR and the UV-soft X-ray band. However, the underlined physics of the second hump with a peak at $\gamma$-ray band is still a big debate.

In leptonic models, inverse-Compton (IC) radiation from the same leptons producing the low-energy component is treated as the source of the emission (Maraschi et al. (1992)). However, Böttcher et al. (2013) explained the emission in hadronic scenarios by synchrotron emission due to losing energy from high-energy hadrons (protons) (for large enough magnetic field(Aharonian, 2000) or photo-meson reactions (Mannheim, 1993)).

Summarising, blazars [1] are quite small but interesting fraction of the entire population of active galactic nuclei (AGN). Blazars are a subclass of AGNs (FSRQ and BL lack objects) with a jet from the radio frequencies up to the TeV range gamma rays. The modern $\gamma$ ray telescopes H.E.S.S., Magic and Veritas and the LAT instrument on board the of the Fermi satellite have detected about 30 cosmological blazars with strong TeV emission (H.E.S.S. Collaboration, 2014; Hinton and Hofmann, 2009). Until now, five FSRQs, S3 0218+35 at $z \approx 0.95$, PKS 1441+25 at $z \approx 0.93$, 3C 279 at $z \approx 0.54$ , 4C+21.35 at $z \approx 0.43$, PKS 1510-089 at $z \approx 0.36$ have been detected at VHE and a total of 62 blazars [2] .

As we will see in the later chapters, the TeV emission from more distant blazars cannot reach Earth because of gamma-gamma attenuation with the EBL restricting the TeV flux of sources more distant than $z \approx 0.16$.

## 2.2 Cosmic voids and intergalactic medium

The intergalactic medium (IGM) is a dilute medium among the cosmic voids of galaxies accommodating the bulk mass of the Universe. Today's perception is that the IGM is occupied by approximately half of the dark matter while the intergalactic baryon fraction is probably much higher. At redshifts $z \leq 20$ or so, without the existence of galaxies, the term "intergalactic" is not valid but limited to the epoch after the beginning of reionization up to $z \sim 147$. Thereafter, the free electron ratio became too low to sustain the coupling of the cosmic gas temperature to the CMB temperature.

---

[1] The name blazar is derived from "BL Lacertae" and "quasar".

[2] http://tevcat.uchicago.edu

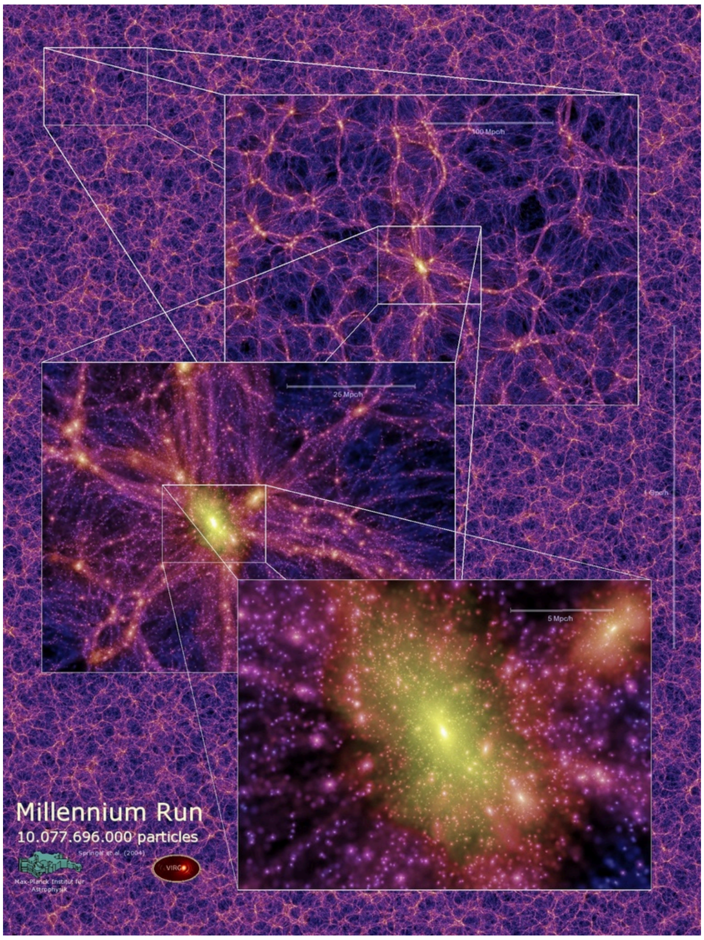

Fig. 2.3 Cosmological N-body simulation "Millennium" revealing the large scale structure of the universe. Figure taken from Springel et al. (2005)

After the Big Bang, there was an era of recombination of cosmic gas upto reshifts of $z \sim 1100$. Then there was the era of formation of the first stars from primordial gas possibly in the rarest peak in the cosmological density field at a redshift of $z \sim 70$ (Naoz et al. (2006)). Gradually, more and more stars formed in the Universe known as POPIII star formation at $z \sim 20-30$ (Trenti and Stiavelli (2009)).

The cosmic gas cooled adiabatically to $\sim 2$ K with the expansion of the Universe at $z = 10$ (Kulkarni et al. (2015)). It is from these cold conditions that the IGM emerged largely as a result of gravity on the primordial matter fluctuations. By the time of formation of first galaxies in the Universe , IGM was exposed to metal enrichment and their radiative backgrounds. Initially, the $\sim 10$ eV and soft X-ray backgrounds heated the gas such that the 21 cm line of atomic hydrogen is detectable (Furlanetto et al. (2006); Madau et al. (1997)). Then, approximately all intergalactic hydrogen was photoionized by the 13.6 eV photons, leading to a cosmological ionization which increased the temperature of IGM to orders of $10^4 K$.

There has been successful studies of the IGM at intermediate redshifts $2 < z < 5$, explaining the statistics of $Ly\alpha$ absorption of intergalactic hydrogen (Vogt et al. (1994)), leading to resolved studies of the $Ly\alpha$ forest absorption (Hu et al. (1995); Kim et al. (1997); Kirkman and Tytler (1997)).

There has been rather much debates on the observations of IGM amongst astrophysicists. Studies such as the cosmological hydrodynamic or N-body simulations explore the spatial structure of the universe via gravitational effects. These computer simulations provide an illustration of the non-homogeneous universe, where most of the matter is gathered in filaments. Springel et al. (2005) presented the well-known "Millennium" N-body simulations (see figure 2.3). Later, the more advanced simulations "Illustris" project led to accurate values for the cosmic star formation rate and for galactic luminosities (Vogelsberger et al. (2014)).

Most of the parameters of the IGM are not known precisely. Here, some of the relevant parameters to this work are presented. The average baryon density in the IGM of cosmic voids is $\simeq 10^{-7} cm^{-3}$ (Madau (2000)). But the uncertainty for the IGM temperature is higher, varying between $10^4 - 10^5$K, depending on the redshifts (Chang et al. (2012); Rudie et al. (2012)).

Generally, the dilute plasma in IGM is considered as a background radiation source in cosmic voids. In the next sections, a brief introduction of the cosmic microwave background (CMB) and extragalactic background light (EBL) is presented as the two other sources of radiation fields in the IGM.

## 2.3 Cosmic microwave background

The cosmic microwave background (CMB) resembles a relic of the evolution of the early Universe and a proof of the Big Bang. It is a bath of baryons and photons with an isotropic radiation of microwave photons that permeates the entire Universe. Shortly after the Big Bang, the Universe cooled down to a point where Thomson scattering stopped and neutral hydrogen atoms were formed. The photons decoupled from baryons with an infinite mean free path leading to a transparent Universe for the first time ever known as CMB.

The temperature of the Universe using the Saha-equation for the equilibrium ionization fraction of hydrogen ($X_e = 0.1$) and the known parameters of baryon-to-photon ratio ($\eta \simeq 6.05 \times 10^{-10}$ (Kolb and Turner, 1990)), approximately at z = 1100 of the end of recombination

---

[3] CMB temperature www.cosmos.esa.int

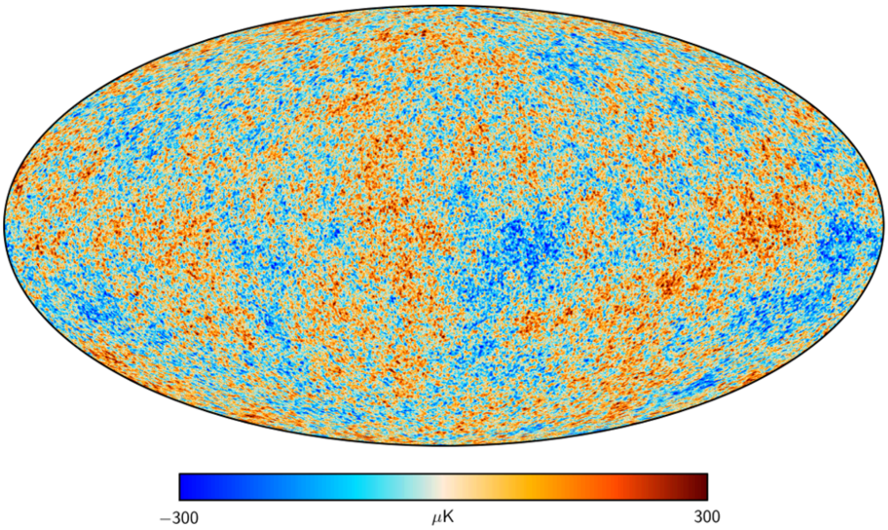

Fig. 2.4 All-sky image of the cosmic microwave background measured by the Planck satellite.[3]Figure taken from Planck Collaboration (2016)

epoch, would be $T_R \approx 3000K$ via

$$\frac{1-X_e}{X_e^2} = 4\sqrt{2}\zeta(3)\Pi^{-1}\eta\frac{T^{3/2}}{m_e}\exp(\frac{13.6eV}{T}). \tag{2.1}$$

Today, due to red-shift expansion of space-time, its average temperature is measured $\mathrm{T}_0 \simeq 2.726\mathrm{K}$ (Fixsen (2009)).

$$1+z_R = \frac{a(t_0)}{a(t_R)} = \frac{T_R}{T_0} \approx 1100 \tag{2.2}$$

Using Planck satellite ( see figure 2.4) and SMICA semi–blind spectral– matching algorithm (Planck Collaboration, 2016), a uniform infrared black-body radiation of the CMB is observed from the early times of the recombination epoch.

Considering the fact that CMB is a black body through integrating Planck formula for describing the energy density :

$$\varepsilon(\nu)d\nu = \frac{8\pi h}{c^3}\frac{\nu^3}{e^{\frac{h\nu}{KT}}-1}d\nu, \tag{2.3}$$

where $h$ is the Planck constant, $c$ is speed of light and $\nu$ is frequency. Integrating over all frequencies, one can derive:

$$\varepsilon_{rad} = \alpha T^4 \tag{2.4}$$

where $\alpha$ is the radiation constant. Thus, the energy density of CMB photons is proportional to $T^4$. Also the average photon energy of CMB is small, $E_{avg} \approx 3K_BT \approx 7 \times 10^{-4}$ eV while the energy of a baryon is $E_b = 939$ MeV.

Also, we note that an interesting feature of CMB map is being uniform while there is a partial anisotropy in the temperature $\simeq 10^{-5}$ which was precisely detected by Cosmic Background Explorer (COBE) satellite (Mather et al. (1990)).

## 2.4 Extragalactic background light

Extragalactic background light (EBL) is another notable radiation field in cosmic voids, ranking second after the CMB. EBL has a full electromagnetic spectrum, from radio to gamma-rays, as the integrated intensity of light throughout the history of the universe. However, it is sometimes defined as the extragalactic intensity spectrum from UV to infrared (Dwek and Krennrich (2013)).

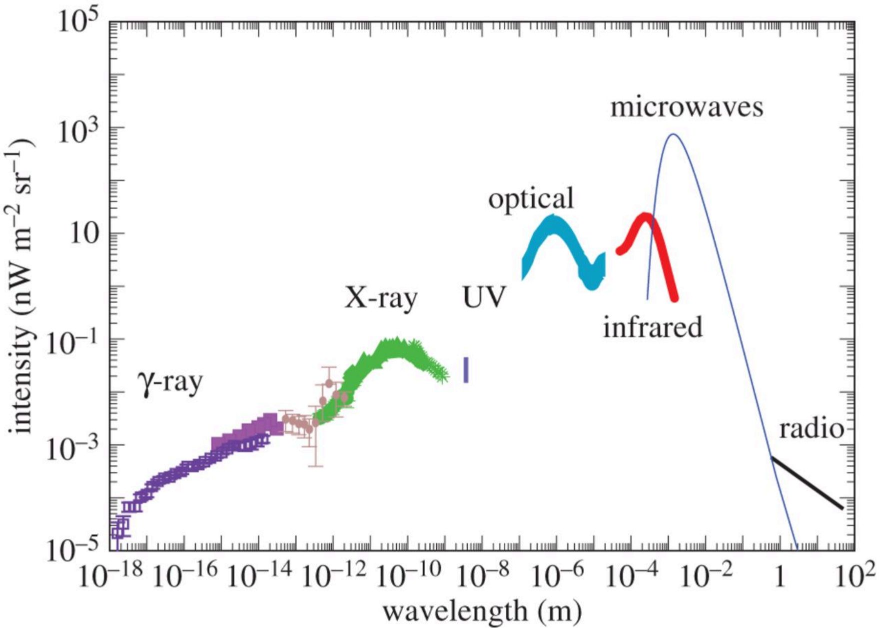

Fig. 2.5 Intensity of the extragalactic background as a function of wavelength in SI units). Figure taken from Cooray (2016)

The current EBL intensity measurements are illustrated in figure 2.5, where the spectral intensity is plotted as a function of the wavelength of background in SI units. The figure is estimated using a statistical average of existing results from the literature (Cooray (2016)). We note two peaks, one at $1\mu m$ from stars and $100\mu m$ from the thermal emission from dust (Primack et al. (2008)).

Direct absolute intensity measurements (such as Zodiacal light due to high signal noise at optical and infrared in the solar system and Milky Way) is difficult comparing to Galactic emission at radio, infra-red, X-ray or gamma rays. However, an instance of such EBL indirect measurements is deriving the number density of infra-red photons leading to electron-positron pair-production by interactions with TeV photons, using absorbed TeV spectra of TeV sources such as blazars and AGNs at cosmological distances. These limits the travelling distance of gamma rays. The soft X-ray/extreme UV extragalactic background at wavelengths of 10 to 100 nm is still unexplored and difficult because of the absorption of the extragalactic photons by the intervening neutral intergalactic medium and the interstellar medium of our galaxy.

## 2.5 Blazar-induced pair beams

Many blazars have been detected as sources of gamma-rays with the energy $E \geq 100$ GeV (de Naurois (2015)) with modern gamma-ray telescopes such as HESS, VERITAS, MAGIC and Fermi LAT instrument. Some of these blazars have photon emission boosted to TeV when observed in the line of sight of jet axis, such as Intermediate-Frequency-Peaked (IBL blazars) and High-Frequency-Peaked BL Lacertae objects (HBL blazars).

As mentioned in section 2.4, the universe is transparent for electromagnetic radiation only up to $\sim 100$ GeV. Above this energy, the photons undergo electron-positron pair production via $\gamma_{\mathrm{TeV}} + \gamma_{\mathrm{EBL}} \longrightarrow \mathrm{e}^- + \mathrm{e}^+$ with the condition that the center of momentum energy of these very-high energy gamma rays and EBL photon exceeds the threshold energy, i.e. $\sqrt{2\mathrm{E}_\gamma \mathrm{E}_{\mathrm{EBL}}(1-\cos\theta)} > 2m_e c^2$. Consequently, these $\gamma$ rays get annihilated as they pass through the EBL. The produced pairs are ultra-relativistic with the typical Lorentz factor $10^5 < \Gamma < 10^7$ in direction of the initial TeV photon (Miniati and Elyiv (2013); Schlickeiser et al. (2012a)). The mean free path for these high energy gamma rays in the TeV range is approximately:

$$l_{\gamma\gamma} \sim 80(1+z)^{-\xi}(E_\gamma/10TeV)^{-1}Mpc \tag{2.5}$$

where $\xi = 4.5$ and $\xi = 0$ for $z \leq 1$ and $z \geq 1$ respectively. (Kneiske, T. M. et al. (2004); Neronov and Semikoz (2009)).

The created pairs beams are subject of many investigations, as they can be affected by several physical processes: (i) inverse-Compton scattering (ICS), (ii) deflection by the intergalactic magnetic field (IGMF), or (iii) collective plasma effects.

For the ICS scenario, let us assume 1 TeV gamma rays (corresponding to $\Gamma \simeq E_\gamma/2m_e c^2 \simeq 10^6$). Also assuming, $E_{CMB} \simeq 10^{-3} eV$(in absence of IGMF and due to ICS with the CMB) then the cascaded photons will have typical energies of approximately $E_{IC} \simeq 2\gamma^2 E_{CMB} = 2$

GeV. Primary gamma rays with $E_\gamma = 40$ TeV produce cascade emission above 100 GeV, where the sensitivity of Fermi-LAT deteriorates. The ICC produces multiple GeV gamma rays from the initial TeV gamma ray accordingly. (for a more detailed description, the interested reader can refer to the works by Aharonian et al. (1994); Elyiv et al. (2009); Plaga (1995) and Neronov and Vovk (2010)). Thus, the TeV source would be accompanied by a GeV halo which is not detected (Abdo (2010); Neronov and Semikoz (2009)). In short, the ICS would result in a gamma-ray emission with the characteristic energy in the GeV band, but as indicated by Fermi-LAT data, the GeV gamma-ray emission is suppressed meaning that the ICS is not the fastest of the three processes (see figure 2.6).

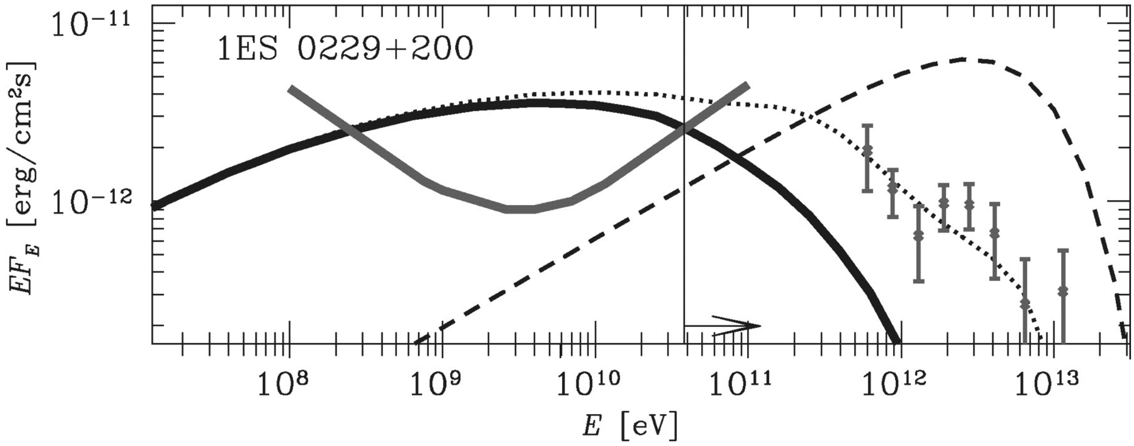

Fig. 2.6 Cascade emission from a TeV blazar (thick solid black curves) with Fermi upper limits (gray curves) and HESS data (gray data points). Thin dashed curve shows the primary (unabsorbed) source spectra. Dotted curve shows the spectra of electromagnetic cascade initiated by pair production on EBL. Vertical line with arrow shows the energies below which the cascade emission should be suppressed. Figure taken from Neronov and Vovk (2010).

The effect of deflection by the IGMF has been also well investigated (Neronov and Semikoz (2009); Neronov and Vovk (2010); Taylor et al. (2011)). The estimated magnitude for these homogeneous fields on the Mpc scale typically ranges from $10^{-17} - 10^{-15}$ G. In this scenario, the electron-positron pairs are deflected away so that the up-scattered beam of gamma rays are not observed by the observer on Earth (Dermer et al. (2011); Neronov and Semikoz (2009); Neronov and Vovk (2010); Taylor et al. (2011)). However, these constraints on the IGMF are valid only under the assumptions that the multi-TeV gamma-ray emission persists on long timescales and that the pairs lose their energy only due to ICS. This latter assumption is crucial and remains debatable.

The importance of collective plasma effects, i.e. the stability of the beam interacting with an unmagnetized IGM, has been pointed out by several authors (Broderick et al.

(2012); Miniati and Elyiv (2013); Schlickeiser et al. (2012b)). In fact, the pairs can induce electrostatic (two-stream, oblique) and electromagnetic (filamentation, Weibel) instabilities (Breizman (1990); Breizman and Riutov (1974); Bret (2006); Bret et al. (2004, 2005, 2010); Godfrey et al. (1975); Lominadze and Mikhailovskii (1979)). In this case, wave-particle interactions can reduce the energy of the pairs by 30-50 % (Bret et al. (2010); Schlickeiser et al. (2002)). Therefore, the collective plasma effects can also substantially suppress the GeV-band gamma-ray emission affecting as well the IGMF constraints.

This is the main focus of the thesis, where the analytical model and particle-in-cell (PIC) simulations are considered for the relevant plasma instabilities along with presentation of the relevant reviews. In the next section of this chapter, an overview of two-stream, oblique, filamentation and Weibel instabilities is presented.

## 2.6 Relevant plasma instabilities

Our universe is the biggest laboratory for plasma systems such as stars, galaxies and intergalactic medium. There are so many kinds of plasma instabilities in the literature which does not fit the scale of this thesis. However, a brief introduction of instabilities relevant to this thesis is presented here, including two electrostatic instabilities (two-stream and oblique) and two electromagnetic instabilities (filamentation and Weibel).

Streaming instabilities depend on important parameters such as direction of the beam propagation, the species of the particles such as electrons or protons, the beam/plasma density ratio, the presence of a current, presence or absence of background magnetic fields and the temperature (where here, the beam is called cold such that the thermal temperate is low in comparison with it is bulk velocity, else it is called hot).

In figure 2.7, a sketch of these instabilities is illustrated. Let's consider the simple case of the counter streaming electron beam propagating against another electron beam, where both beams are cold without any background magnetic field. The instabilities have different names such that for $k \parallel v_b$ and $\delta B = 0$ they are known as the **two-stream instability** or so-called "Buneman instability" (Buneman, 1959), or of $k \perp v_b$ for the **filamentation instability**. The modes at intermediate angles $\mathbf{k} \cdot \mathbf{v}_b$, i.e between 0 and $\frac{\pi}{2}$, are called **oblique** modes consisting of density, electric and magnetic perturbations, and they can be in some cases be faster than the two-stream and filamentation modes (Bret et al. (2010)).

Generally for the **Weibel** instability, the distribution function with anisotropies can drive instabilities. Here, the electron temperatures are assumed such that $T_z = T_x = T_\perp$ and $T_y = T_\parallel > T_\perp$ and a magnetic fluctuations of $\mathbf{B} = \mathrm{B_z cos(kx)}\mathbf{z}$. The magnetic field perturbations focus electrons into current bundles such that they amplify the magnetic field

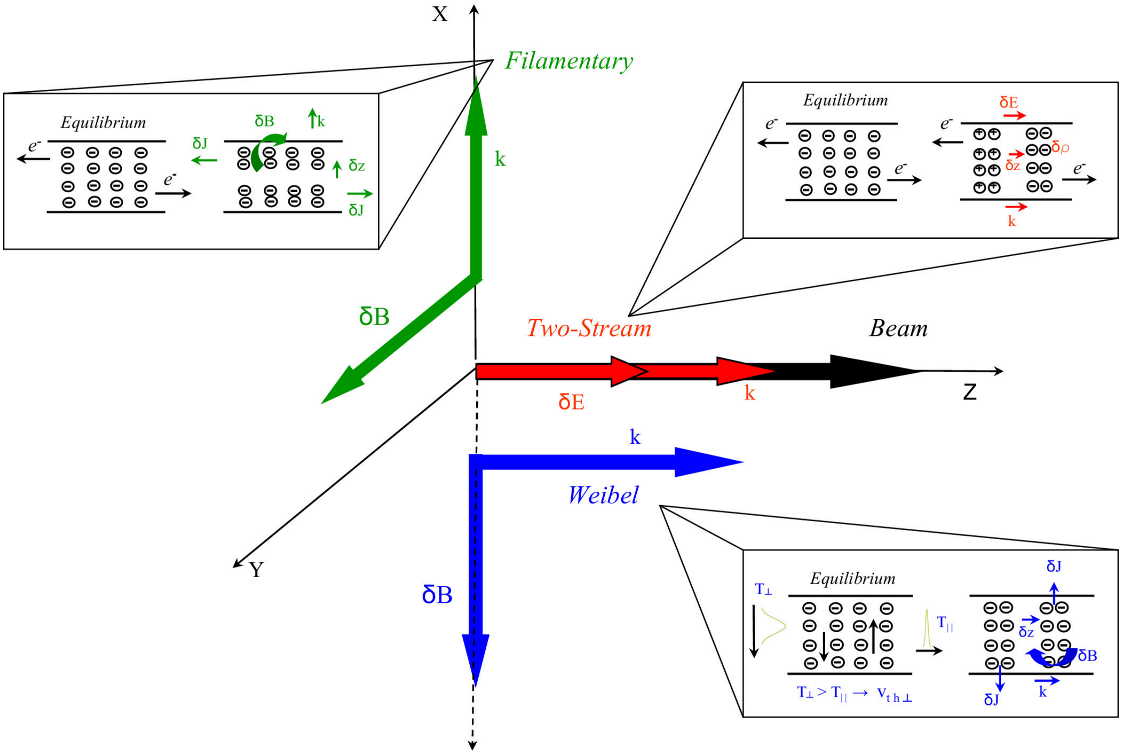

Fig. 2.7 The filamentation, two-stream, oblique and Weibel modes. Figure taken from Cottrill et al. (2008)

perturbations. In other words, if $T_{\|} > T_{\perp}$ , electrons moving in y direction, will have a higher mean velocity leading to stronger currents, resulting in the instability.

In the non-linear regime, the magnetic field becomes high enough such that the anisotropy becomes too weak and the Weibel instability saturates. (i.e the parallel temperature has been reduced in order to increase the perpendicular temperature and also to develop a magnetic field.)

# Chapter 3

# Analytical model

In this chapter, first we start with an overview of the literature related to this work, followed by our analytical model (covered in sections 3.4 and 3.5). This is the main framework which this thesis is relied on in later chapters.

Amongst the astrophysical plasma systems, IGM has a typical density of a few particles per cubic metre and it is much less dense compared to other plasma systems such as stellar plasma. Important properties of the plasma are based on the characteristic time and length scale, which are defined by:

- The **Electron plasma frequency**
$$\omega_{pe} = \left(\frac{n_0 e^2}{\varepsilon_0 m_e}\right)^{\frac{1}{2}} \tag{3.1}$$
- The **Debye length**
$$\lambda_D = \frac{v_{th}}{\omega_{pe}} \tag{3.2}$$
- The **Skin length**
$$\lambda_e = \frac{c}{\omega_{pe}} \tag{3.3}$$

where $n_0$ is particle density and $v_{th}$ is thermal velocity of the plasma system.

The type of plasmas we are dealing with in this work, due to their very low densities such as in IGM, is called collisionless. Generally, in collisionless systems, the time scale of the phenomena under study is short compared to the collision time scale ( and also the length scales are shorter than the mean free path for the coulomb collisions). However, the same plasma with the same parameters could be considered as collisional depending on the scales of time and distance of the concerned phenomena. Then, in systems such stellar plasma, it is a collision dominated system. In the later case, the particles quickly form an isotropic Maxwellian velocity distribution $f(v)$ and the plasma distribution function can be regarded as a continuous fluid or a delta function, so that the magnetohydrodynamics (MHD) or two-fluid models are considered for the analytical description of such systems. However, for the former case of a collisionless plasma, the precise form of the velocity distribution function based on a statistical model is vital for the analytical description which is referred to as kinetic treatment. This kinetic treatment is the main framework of the analytical descriptions of the plasma in this thesis and also in the computer simulations followed by.

The relevant equation to deal with such problems is the Vlasov equation, completed by Maxwell equations. This thesis relies exclusively on the kinetic framework, which is detailed in the following section.

## 3.1 Kinetic representation

For the kinetic description of a plasma, we need to use the Vlasov equation coupled with the Maxwell equations. Assuming the particle distribution to be in an equilibrium and introducing a small perturbation around this distribution, one can linearise the equations with respect to the small quantities and find solutions leading to dispersion relations that govern the spectrum of allowed waves in the plasma.

There are many cases where the exact form of the velocity distribution function is significant for the dispersion relation. Such cases are referred to as kinetic instabilities. For one particle trajectory one should follow six-dimensional space-momentum, however for the whole system of plasma this would be impossible. Instead, the Kinetic theory uses a distribution function of particle species $i$ at time t with the number density:

$$n_i(\mathbf{r},t) = \int f_i(\mathbf{r},\mathbf{p},t) d^3 p. \tag{3.4}$$

For the plasma feedback to the electromagnetic fields, we need the total charge and current densities for all species $i$ from Gauss's law and Ampere's law:

$$\rho(\mathbf{r},t) = \sum_i q_i \int f_i(\mathbf{r},\mathbf{p},t) d^3 p, \tag{3.5}$$

$$\mathbf{j}(\mathbf{r},t) = \sum_i q_i \int \mathbf{v} f_i(\mathbf{r},\mathbf{p},t) d^3 p. \tag{3.6}$$

Inserting equations 3.5 and 3.6 to Maxwell's equations:

$$\nabla \cdot \mathbf{E} = 4\pi\rho, \tag{3.7}$$

$$\nabla \cdot \mathbf{B} = 0, \tag{3.8}$$

$$\nabla \times \mathbf{E} = -\frac{1}{c}\frac{\partial \mathbf{B}}{\partial t}, \tag{3.9}$$

$$\nabla \times \mathbf{B} = \frac{1}{c}\left(4\pi\mathbf{j} + \frac{\partial \mathbf{E}}{\partial t}\right). \tag{3.10}$$

And the feedback of electromagnetic fields on the particles is described by the Lorentz force:

$$\frac{d\mathbf{p}}{dt} = q\left(\mathbf{E} + \frac{1}{c}\mathbf{v} \times \mathbf{B}\right), \tag{3.11}$$

where $\mathbf{v} = (\mathbf{p}/\Gamma m)$ with the relativistic Lorentz factor of $\Gamma = (1 - \frac{v^2}{c^2})^{-\frac{1}{2}}$. Assuming the distribution function is locally conserved according to the Liouville's theorem, its continuity equation with source and sink term being zero, reads as:

$$\frac{\partial f}{\partial t} + \dot{\mathbf{r}} \cdot \frac{\partial f}{\partial \mathbf{r}} + \dot{\mathbf{p}} \cdot \frac{\partial f}{\partial \mathbf{p}} = 0, \tag{3.12}$$

replacing the Lorentz force from equation 3.12 and velocity term results in the Velasov equation:

$$\frac{\partial f}{\partial t} + \mathbf{v}\frac{\partial f}{\partial \mathbf{r}} + q\left(\mathbf{E} + \frac{1}{c}\mathbf{v} \times \mathbf{B}\right)\frac{\partial f}{\partial \mathbf{p}} = 0 \tag{3.13}$$

which could also be derived from Boltzmann's equation with the collision term set to zero in the form of collisionless Boltzmann equation.

In short, one can derive the fields from Maxwell's equations originating from the charge and current densities. Albeit, using Vlasov equation for the fields the distribution function is derived. However, using the Vlasov-Maxwell system, it is not easy to derive the analytical solutions, which brings us to the alternative approach of making approximations to decouple the equations from each other through simplified linearisation.

We start with a linear representation of the Vlasov-Maxwell equations by assuming the exact equilibrium solutions for the distribution function, the electric field, and the magnetic field and then inserting small derivations from these solutions such that:

$$f(\mathbf{r},\mathbf{p},t) = f_0(\mathbf{r},\mathbf{p},t) + \delta f(\mathbf{r},\mathbf{p},t), \tag{3.14}$$

$$\mathbf{E}(\mathbf{r},t) = \mathbf{E}_0(\mathbf{r},t) + \delta\mathbf{E}(\mathbf{r},t), \tag{3.15}$$

$$\mathbf{B}(\mathbf{r},t) = \mathbf{B}_0(\mathbf{r},t) + \delta\mathbf{B}(\mathbf{r},t). \tag{3.16}$$

Inserting the first order approximation of equations 3.14 to 3.16 in the Vlasov-Maxwell equations and keeping in mind that the current and charge densities only depend on the perturbation terms, we obtain:

$$\frac{\partial \delta f}{\partial t}+\mathbf{v}\frac{\partial \delta f}{\partial \mathbf{r}}+q\left(\mathbf{E}_0+\frac{1}{c}\mathbf{v}\times\mathbf{B}_0\right)\frac{\partial \delta f}{\partial \mathbf{p}}=-q\left(\delta\mathbf{E}_0+\frac{1}{c}\mathbf{v}\times\delta\mathbf{B}_0\right)\frac{\partial f_0}{\partial \mathbf{p}}, \tag{3.17}$$

$$\nabla\cdot\delta\mathbf{E}=4\pi\delta\rho, \tag{3.18}$$

$$\nabla\cdot\delta\mathbf{B}=0, \tag{3.19}$$

$$\nabla\times\delta\mathbf{E}=-\frac{1}{c}\frac{\partial\delta\mathbf{B}}{\partial t}, \tag{3.20}$$

$$\nabla\times\delta\mathbf{B}=\frac{1}{c}\left(4\pi\delta\mathbf{j}+\frac{\partial\delta\mathbf{E}}{\partial t}\right). \tag{3.21}$$

Using the method of characteristics by Koskinen (2011), the equation 3.17 can be solved by integrating over unperturbed orbits, introducing new variables for the position and momentum with the boundary condition of $r'(t'=t)=r$ and $p'(t'=t)=p$ such that

$$\frac{d\mathbf{r}'}{dt'}=\mathbf{v}' \qquad \mathit{and} \qquad \frac{d\mathbf{p}'}{dt'}=q\Big(\mathbf{E}_0(\mathbf{r}',t')+\frac{1}{c}\mathbf{v}'\times\mathbf{B}_0(\mathbf{r}',t')\Big), \tag{3.22}$$

and the total derivative of distribution as:

$$\begin{aligned}\frac{d\delta f(\mathbf{r}',\mathbf{p}',t')}{\delta t'}&=\frac{\partial\delta f(\mathbf{r}',\mathbf{p}',t')}{\delta t'}+\frac{d\mathbf{r}'}{dt'}\cdot\frac{\partial\delta f(\mathbf{r}',\mathbf{p}',t')}{\partial\mathbf{r}'}+\frac{d\mathbf{p}'}{dt'}\cdot\frac{\partial\delta f(\mathbf{r}',\mathbf{p}',t')}{\partial\mathbf{p}'}\\&=-q\Big(\delta\mathbf{E}(\mathbf{r}',t')+\frac{1}{c}\mathbf{v}'\times\delta\mathbf{B}(\mathbf{r}',t')\Big)\cdot\frac{\partial f_0(\mathbf{r}',\mathbf{p}')}{\partial\mathbf{p}'},\end{aligned} \tag{3.23}$$

$$\begin{aligned}\delta f(\mathbf{r},\mathbf{p},t)=-q\int_{-\infty}^{t}\Big(\delta\mathbf{E}(\mathbf{r}',t')+\frac{1}{c}\mathbf{v}'\times\delta\mathbf{B}(\mathbf{r}',t')\Big)\cdot\frac{\partial f_0(\mathbf{r}',\mathbf{p}')}{\partial\mathbf{p}'}dt'\\+\delta f\Big(\mathbf{r}'(-\infty),\mathbf{p}'(-\infty),\mathbf{t}'(-\infty)\Big).\end{aligned} \tag{3.24}$$

Reintroducing the index species i into 3.25

$$\delta\mathbf{j}(\mathbf{r},t)=\sum_i q_i\int\mathbf{v}\delta f_i(\mathbf{r},\mathbf{p},t)d^3p=\hat{\sigma}\cdot\delta\mathbf{E}. \tag{3.25}$$

where equation 3.25 defines the conductivity tensor $\sigma(x,t)$ of the plasma, corresponding to the plasma feedback on electro-magnetic perturbation.

To present the Maxwell operator for an infinite, homogeneous and stationary system, one can apply perturbation quantities as spatial dependence such that the solutions are assumed to be Fourier-Laplace integrals

$$\tilde{\mathbf{E}}(\mathbf{r},t) = \int_0^\infty dt \int_{-\infty}^\infty d^3k\mathbf{E}(\mathbf{k},t)e^{i(\omega t-\mathbf{k}.\mathbf{r})}, \tag{3.26}$$

$$\tilde{\mathbf{B}}(\mathbf{r},t) = \int_0^\infty dt \int_{-\infty}^\infty d^3k\mathbf{B}(\mathbf{k},t)e^{i(\omega t-\mathbf{k}.\mathbf{r})}, \tag{3.27}$$

$$\tilde{f}(\mathbf{r},\mathbf{p},t) = \int_0^\infty dt \int_{-\infty}^\infty d^3kf(\mathbf{k},\mathbf{p},t)e^{i(\omega t-\mathbf{k}.\mathbf{r})}. \tag{3.28}$$

Inserting the above equations to Maxwell's equations and the current density and combining them, we can easily derive a single wave equation for electric field

$$(-\omega^2+k^2c^2-4\pi i\omega\hat{\sigma})\cdot\tilde{\mathbf{E}}-c^2(\mathbf{k}\cdot\tilde{\mathbf{E}})\mathbf{k} = ic\mathbf{k}\times\mathbf{B}(\mathbf{k},t=0)-i\omega\mathbf{E}(\mathbf{k},t=0), \tag{3.29}$$

which can be rewritten with the index notation as

$$\Lambda_{nj}E_j(\mathbf{k},\omega) = A_n(\mathbf{k},\omega), \tag{3.30}$$

where the tensors $\Lambda_{nj}$ and $\Psi_{nj}$ define Maxwell operator and dielectric tensor respectively such that:

$$\Lambda_{nj} := \frac{k^2c^2}{\omega^2}\left(\frac{k_nk_j}{k^2}-\delta_{nj}\right)+\Psi_{nj}, \tag{3.31}$$

$$\Psi_{nj} := \delta_{nj}+\frac{4\pi i}{\omega}\sigma_{nj}, \tag{3.32}$$

which contains the conductivity tensor $\sigma_{nj}$ and the Kronecker delta $\delta_{nj} = \begin{cases} 1, & \text{if } n=j \\ 0, & \text{otherwise} \end{cases}$ and $\mathbf{A}$ is given by:

$$A_n(\mathbf{k},\omega) = \frac{i}{\omega}E_n(\mathbf{k},t=0)-\frac{ic}{\omega^2}\varepsilon_{nrs}k_rB_s(\mathbf{k},t=0), \tag{3.33}$$

where $\varepsilon_{nrs}$ is the defined Levi-Civita symbol.

A solution for the electric field perturbations is derived from the inversion of Maxwell operator, if the operator is known and invertible. This leads to the dispersion relation of the late time reaction of the plasma to small perturbations:

$$det(\hat{\Lambda}(\mathbf{k},\omega)) = 0. \tag{3.34}$$

Equation 3.34 provides the so-called dispersion relation which yields the dependence of the wave frequency on the wave vector, $\omega = \omega(\mathbf{k})$, distinguishing the wave modes of plasma configuration.

Now we will consider an unmagnetized plasma to linearise the wave solution of Vlasov equation, assuming:

$$\begin{aligned} & f = f_0(\mathbf{v}) + f_1(\upsilon)e^{i(\mathbf{k}\cdot\mathbf{x}-\omega t)}, \\ & \mathbf{E} = \mathbf{E}_1 e^{i(\mathbf{k}\cdot\mathbf{x}-\omega t)} \quad and \quad \mathbf{B} = \mathbf{B}_1 e^{i(\mathbf{k}\cdot\mathbf{x}-\omega t)}. \end{aligned} \tag{3.35}$$

Here, $f_0$ represents the equilibrium electron distribution, whereas $f_1$ denotes a small perturbation in the form of the plane wave. Equation 3.13 can be rewritten as

$$-i\omega f_1 + \mathbf{v}\cdot i\mathbf{k} f_1 + \frac{q}{m}(\mathbf{E}_1 + \mathbf{v}\times\mathbf{B}_1)\cdot\frac{\partial f_0}{\delta\mathbf{v}} = 0. \tag{3.36}$$

Assuming $f_0$ is isotropic, $\frac{\partial f_0}{\partial \mathbf{v}}$ is in the direction of $\mathbf{v}$ such that the term $\mathbf{v}\times\mathbf{B}_1.\frac{\partial f_0}{\partial \mathbf{v}} = 0$, thus $f_1$ can be derived in the form of:

$$f_1 = \frac{\frac{q}{m}\mathbf{E}_1\cdot\frac{\partial f_0}{\partial \mathbf{v}}}{i(\omega - \mathbf{v}\cdot\mathbf{k})}. \tag{3.37}$$

Now by inserting $f_1$ in Ampere's Law, the current density can be written as:

$$\mathbf{j} = q\int \mathbf{v} f_1 d^3\upsilon = \frac{q^2}{im}\int \frac{\mathbf{v}\frac{\partial f_0}{\partial \mathbf{v}}}{\omega - \mathbf{v}\cdot\mathbf{k}} d^3\upsilon\cdot\mathbf{E}_1 = \sigma\cdot\mathbf{E}_1, \tag{3.38}$$

Where as discussed before, $\sigma$ is the conductivity tensor. Each element of the dielectric tensor contains the integral in the form:

$$1 + \int \frac{F(\mathbf{v})}{\omega - \mathbf{k}\cdot\mathbf{v}} d^3\mathbf{v}. \tag{3.39}$$

However the problem with this integral is obvious due to the zero value in the denominator. Integrating through the pole at $v = \frac{\omega}{k}$ was magnificently done by Landau (1946).

Considering an infinitely small electrostatic potential energy such that the modulation velocity would be negligible, in the wave frame ( i.e moving with the phase velocity of wave), the potential would be at rest and the collisionless particles are moving at constant speed with this frame (figure 3.1). Let us investigate the particle motion in a time period $\tau$ such that it is smaller than the lifetime of the potential. Particles moving with the wave frame speed would experience a potential modulation, but averaged over time $\tau$ their kinetic energy is constant. Such particles are referred as *non-resonant particles*. Howbeit the so called *resonant particles* are at rest relative to the wave frame, such that they would experience the wave potential as a DC field, where averaged over time $\tau$ their kinetic energy would increase

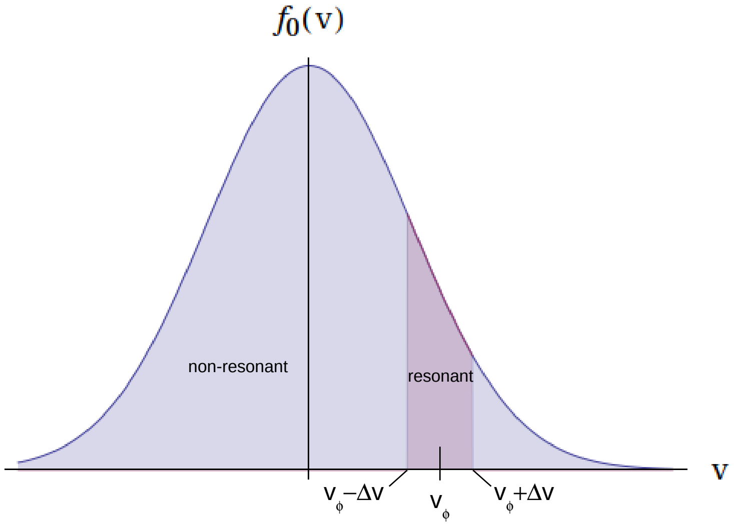

Fig. 3.1 A Sketch of the resonant and non-resonant particles. Figure taken from Bret (2012)

(in the acceleration phase) or decrease (in the deceleration phase). These particles will participate in the energy exchange with the wave, either in form of damping or amplification of the wave potential energy.

## 3.2 Linear Landau damping

An important feature of collisionless plasmas was discovered by Landau (1946) known as Landau damping, derived from Vlasov's equation, describing the absorption of Langmuir waves or of other waves by the plasma. As mentioned in last section, equation 3.39 at $\omega = \mathbf{k}\cdot\mathbf{v}$ has a complex solution that can be written as $\omega = \omega_r + i\gamma$.

Landau presented the damping effect purely mathematically based on the Cauchy problem. The contour must pass below the singularity. If $\gamma \ll \omega_r$, the Landau contour can be approximated by a line along the v-axis with semicircular path around this pole without the exact point of $v = \frac{\omega}{k}$. The details can be found in Montgomery and Tidman (1964), therefore the integral can be derived:

$$\int \frac{dv}{\omega - \mathbf{k}\cdot\mathbf{v}} g(v) = P\int \frac{dv}{\omega - \mathbf{k}\cdot\mathbf{v}} g(v) + i\pi g(v)|_{v=\omega_r/k} \tag{3.40}$$

where $P$ denotes the principal part of the integral, g(v) is an arbitrary function and $k > 0$.

Furthermore, for a sufficiently small damping,$|\gamma| \ll |\omega_r|$ , one can derive an estimate for the imaginary part from equation 3.34 in the form of

$$\gamma = k\pi \frac{\sum_j \frac{\omega_j^2}{n_j} \frac{\partial f_0}{\partial v}|_{v=\omega_r/k}}{\sum_j \frac{\omega_j^2}{n_j} P \int \frac{dv}{v-\omega_r/k} \frac{\partial f_0}{\partial v}}, \tag{3.41}$$

(where $k > 0$), From equation 3.41, it is well seen that the sign of $\gamma$ is determined by the slope of the distribution function at the velocity $v = \omega_r/k$.

The same complicated method can derive a solution for the electric field. Schlickeiser et al. (2002) presented this at late times ( $t \to \infty$) where the complex term of the Laplace transformation vanishes exponentially leading to:

$$\mathbf{E}(\mathbf{k},t) = \sum_m R_m e^{-i\omega_{r,m}(\mathbf{k})t} e^{\gamma_m(\mathbf{k})t}, \tag{3.42}$$

where m refers to wave modes and $R_m$ is the residue of the pole at $\omega_{r,m}$. It is easy to notice that the electric field is constituted of sinusoidal waves at late time either damping ($\gamma < 0$) or amplifying with time ($\gamma > 0$).

It is useful to consider the interaction of a plasma wave with the particles of velocity close to the phase speed of the wave from the energetic point of view. Since the particle velocity is close to the wave velocity, most of the exchange happens with the trapped particles by the wave. In case of a decreasing velocity function in the distribution function, the majority of trapped particles are accelerated rather than decelerated. Thus the wave is damped by losing energy to plasma.

The dispersion relation is widely used to investigate plasma instabilities and the respective growth rates. It is useful to mention the hierarchy of the modes for cold plasma regime in the $(\alpha, \gamma_b)$ phase space, presented by Bret et al. (2010). With $n_b$ and $n_e$ as the number densities for the beam and plasma respectively, the competing modes for dilute astrophysical plasmas $\alpha = n_b/n_e \ll 1$ for the Two-stream, Oblique and filamentation instabilities read as:

$$\frac{\gamma_{TS}}{\omega_p} = \frac{\sqrt{3}}{2^{4/3}} \frac{\alpha^{1/3}}{\gamma_b}, \tag{3.43}$$

$$\frac{\gamma_{Obl}}{\omega_p} = \frac{\sqrt{3}}{2^{4/3}} (\frac{\alpha}{\gamma_b})^{1/3}, \tag{3.44}$$

$$\frac{\gamma_{FI}}{\omega_p} = \frac{v_b}{c} \sqrt{\frac{\alpha}{\gamma_b}}. \tag{3.45}$$

In sections 3.4 and 3.5, the electrostatic instability driven by blazar-induced pair beams will be presented for two cases of monoenergetic pair distributions $\Delta\Gamma \ll \langle\Gamma\rangle$ and the realistic non-monoenergetic pair distributions $\Delta\Gamma \gg \langle\Gamma\rangle$ based on our publications Rafighi et al. (2017) and Vafin et al. (2018). But first an overview of the related plasma studies is presented in section 3.3.

## 3.3 Overview of relevant plasma studies

In this thesis, we want to investigate the relevant plasma instabilties to blazar-induced pair beams interacting with the IGM, using PIC simulations. We cannot simulate the realistic pair-beam parameters because of the small density. For this reason, we need to find some set of parameters, where these parameters satisfy some conditions which garantee that our simulations reasonably reproduce the behaviour of the realistic blazar-induced pair beams. The conditions will be presented in sections 5.1.2 and 5.2.1 where energy density, intitial instability development and non-linear evolution is thoroughly explained.

We consider a pair beam created only by the initial TeV gamma-ray emission neglecting inverse-Compton scatterin (ICS). The typical parameters of the created beams depend on the distance from a blazar, and they are $\langle\Gamma\rangle = 10^5$, $\Gamma = 10^3 - 10^8$, $n_b = 10^{-25} - 10^{-19}$ cm$^{-3}$, $\Delta\theta \approx 1/\langle\Gamma\rangle \approx 10^{-5}$ ($\Delta\theta$ is the angular spread), whereas typical parameters of the IGM are $T = 10^4 - 10^7$ K, $n = 10^{-7}$ cm$^{-3}$ (Broderick et al., 2012; Miniati and Elyiv, 2013; Schlickeiser et al., 2012b; Sironi and Giannios, 2014). Thus, the energy density ratio is $\varepsilon = n_b\langle\Gamma\rangle m_e c^2/(nk_BT) \approx 10^{-10} - 10^{-1}$ ($k_B$ is the Boltzmann constant, $m_e$ is the electron mass) indicating that the pair beam cannot heat the IGM plasma considerably. This point was realized by Kempf et al. (2016) who conducted simulations for $\varepsilon = 0.1$. The parameters of the simulations by Sironi and Giannios (2014) are $\alpha = n_b/n \approx 10^{-2}$, $\Gamma \approx 10^2$, and $k_BT/(m_ec^2) \approx 10^{-8}$, resulting in $\varepsilon \approx 10^8$, a parameter regime that is not relevant for realistic pair beams. Moreover, such a high energy density ratio causes anisotropic plasma heating that can eventually drive the Weibel instability, as it is discussed later. We note that Kempf and Sironi have studied a beam distribution with $\Delta\Gamma \ll \langle\Gamma\rangle$. We also investigate this case in section 3.4, whereas a realistic distribution with $\Delta\Gamma \gg \langle\Gamma\rangle$ will be studied in section 3.5.

### 3.3.1 Reactive vs Kinetic regime

The pair beam can induce two unstable modes: electrostatic and electromagnetic. The growth rate of these instabilities sensitively depends on the momentum spread of the beam. If the momentum spread is small enough, then the instabilities evolve in the so-called **reactive**

**regime**. In this case, the beam can be mathematically treated as a delta function (Schlickeiser et al. (2012b)) in the form of $n_b\delta(p_{\|}-\Gamma_b m_e\beta_b c)$, where the distribution function for the cold beam in a cold background at rest is:

$$f(p_{\perp},p_{\|})=\frac{\delta(p_{\perp})}{2\pi p_{\perp}}\sum_j\sum_i N_j\delta(p_{\|}-\Gamma_b m_i\beta_i u_i). \tag{3.46}$$

and the growth rates of the electrostatic and electromagnetic instabilities are maximal perpendicular to the direction of the beam propagation (Godfrey et al., 1975).

As the momentum spread increases, the electromagnetic instability becomes stabilized (Bret et al., 2005), while the maximum growth rate of the electrostatic mode shifts to the direction parallel to the beam propagation (Breizman, 1990). This is the so-called **kinetic regime**. Miniati and Elyiv (2013) have argued that the momentum spread of the realistic pair beam drastically reduces the growth rate of the electrostatic instability. Later, Schlickeiser et al. (2013) disputed this statement. Sironi and Giannios (2014) have demonstrated that the maximum growth rate occurs in the direction almost parallel to the beam (contrary to the reactive regime, when the maximum growth rate occurs in quasi-perpendicular direction to the beam). But Schlickeiser et al. (2013) have assumed the parallel direction of the wave vector from the very beginning. In this case, the electrostatic growth rate, indeed, only weakly depends on the beam temperature (Bret et al., 2005). Thus, we can conclude that the electrostatic instability for a blazar-induced beam evolves in the kinetic regime at all angles with the maximum growth rate parallel to the beam propagation. It can be shown (section 3.4) that for the beam parameters used by Kempf et al. (2016) and Sironi and Giannios (2014) the electrostatic instability has evolved in the reactive regime.

The following sections 3.4 and 3.5 are based on our publications Rafighi et al. (2017) and Vafin et al. (2018). The analytical part is mainly based on the endeavours of my collaborator, Dr. Vafin.

## 3.4 Monoenergetic pair beams

In this section, we develop a simple analytical model of plasma instabilities driven by a monoenergetic beam, based on our publication (Rafighi et al., 2017). We note that Kempf et al. (2016) and Sironi and Giannios (2014) have studied a beam distribution with $\Delta\Gamma \ll \langle\Gamma\rangle$. We also investigate this case in this section, whereas a realistic distribution with $\Delta\Gamma \gg \langle\Gamma\rangle$ will be studied in in section 3.5.

### 3.4.1 The electrostatic instability

In section 3.3.1 we noted that the electrostatic instability of a cold beam evolves in the kinetic regime and has its maximum growth rate in the direction almost parallel to the beam propagation. At the same time, Schlickeiser et al. (2013) demonstrated that the growth rate of the parallel electrostatic instability depends very weakly on the momentum spread of the beam. Therefore, we can use the well-known growth rate of the two-stream instability for a cold plasma,

$$\gamma_{\mathrm{TS}} = \frac{3^{1/2}}{2^{4/3}} \omega_p \alpha^{1/3} \Gamma^{-1}. \tag{3.47}$$

In consequence, we need to investigate only the electromagnetic Weibel instability, using the waterbag distribution.

#### Waterbag Distribution

It should be noted that the most unstable wave vector of the Weibel mode can be in the transverse direction to the beam (see Califano et al. (1998)) as well as in the oblique direction (see Bret et al. (2010)). Moreover, the work by Bret et al. (2010) shows that for dilute beams the maximum growth rates of Weibel mode in the transverse and oblique directions can differ by a factor 2. Therefore, to make a rough estimation, we will study the Weibel instability only for wave vectors perpendicular to the beam.

In order to solve the dispersion relation, one can use the monokinetic or so-called "cold" distribution function which was introduced in previous section 3.3.1 with the general form

$$f_j(\mathbf{p}) = \delta(p_x)\delta(p_y)\delta(p_z - P_j), \tag{3.48}$$

where $P_j = m_e \gamma_j v_j$ for the beam and plasma electrons, giving a zero-order analytical estimates useful in reactive regime. Nonetheless, the waterbag distributions is the mathematical convenient tool to study kinetic beam-plasma instabilities (figure 3.2).

To derive analytical results with temperature effects, the beam-plasma system is modelled by a waterbag distribution in a relativistic setting. The waterbag distribution is considered analytically friendly to “play” with parallel and transverse thermal spreads, however not useful in the high temperature regime and are unable to produce any Landau damping (see Bret et al. (2005); Yoon and Davidson (1987)).

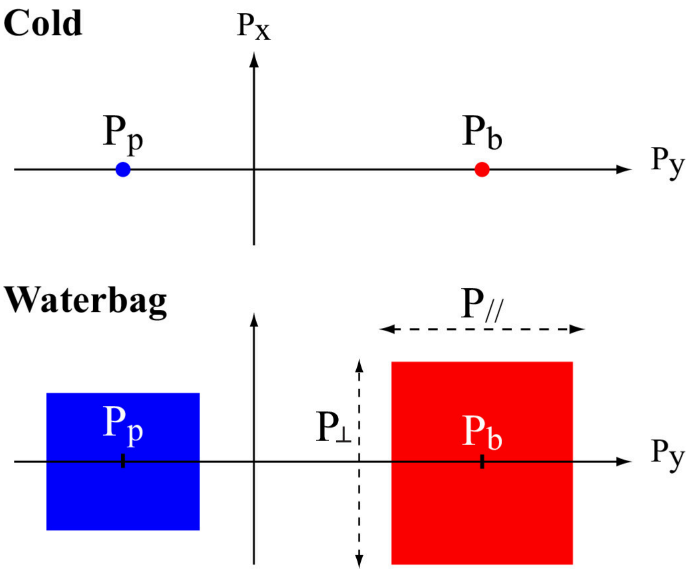

Fig. 3.2 Schematic representations of the cold and waterbag distribution functions taken from Bret et al. (2010)

To sum up, the waterbag distributions of the beam and the plasma that we will use in this section are respectively:

$$f_b(\mathbf{p}) = \frac{n_b}{4p_{\perp,b}^2(p_{\parallel,b}^+ - p_{\parallel,b}^-)} \left[\theta\left(p_z + p_{\perp,b}\right) - \theta\left(p_z - p_{\perp,b}\right)\right]$$
$$\times \left[\theta\left(p_y + p_{\perp,b}\right) - \theta\left(p_y - p_{\perp,b}\right)\right] \left[\theta\left(p_x - p_{\parallel,b}^-\right) - \theta\left(p_x - p_{\parallel,b}^+\right)\right], \quad (3.49)$$

$$f_p(\mathbf{p}) = \frac{n}{8p_{\perp,p}^2 p_{\parallel,p}} \left[\theta\left(p_z + p_{\perp,p}\right) - \theta\left(p_z - p_{\perp,p}\right)\right]$$
$$\times \left[\theta\left(p_y + p_{\perp,p}\right) - \theta\left(p_y - p_{\perp,p}\right)\right] \left[\theta\left(p_x + p_{\parallel,p}\right) - \theta\left(p_x - p_{\parallel,p}\right)\right], \quad (3.50)$$

where $p_{\parallel,b}^{\pm} = p_0 \pm p_{\parallel,b}$; $p_0$ is the beam drift momentum; $p_{\parallel,b}$ and $p_{\perp,b}$, respectively, the parallel and perpendicular momentum spreads of the beam; $p_{\parallel,p}$ and $p_{\perp,p}$, respectively, the parallel and perpendicular momentum spreads of the background plasma; and $\theta(x)$ is the Heaviside step function [$\theta(x) = 1$ for $\theta > 0$ and 0 otherwise]. The beam and background plasma are assumed to be homogeneous with number densities, accordingly, $n_b$ and $n$. It is useful to consider two cases separately: (i) $p_{\perp,b} = p_{\parallel,p} = p_{\perp,p} = 0$ and (ii) $p_{\parallel,b} = 0$.

### 3.4.2 Weibel mode

Assuming the waterbag distribution function as 3.49 and 3.50 we now derive the dispersion relations and growth rate for the Weibel instability for different cases of $p_\perp$(transverse to the beam) and $p_\parallel$ (parallel to the beam) for the beam and plasma.

**Case** $p_{\perp,b} = p_{\parallel,p} = p_{\perp,p} = 0$

We derive the dispersion equation for this case in Appendix A.1. It reads

$$\begin{aligned}&\left[1-\frac{\omega_p^2}{\omega}-\frac{\omega_b^2}{\omega^2}U_1\right]\left\{1-\left(\frac{kc}{\omega}\right)^2-\frac{\omega_p^2}{\omega^2}-\right.\\ &\qquad\left.-\frac{\omega_b^2}{\omega^2}\left[\left(\frac{kc}{\omega}\right)^2 U_1+\left(1-\left(\frac{kc}{\omega}\right)^2\right)U_2\right]\right\}-\\ &\qquad\qquad-\left(\frac{\omega_b^2}{\omega^2}\frac{kc}{\omega}U_3\right)^2=0. \qquad (3.51)\end{aligned}$$

Taking the limiting case $p_{\parallel,b} \ll p_0$, equation (3.51) provides the classical textbook result (Breizman (1990)):

$$\begin{aligned}&\left[1-\frac{\omega_p^2}{\omega}-\frac{\omega_b^2}{\Gamma\omega^2}\right]\left\{1-\left(\frac{kc}{\omega}\right)^2-\frac{\omega_p^2}{\omega^2}-\frac{\omega_b^2}{\Gamma^3\omega^2}-\right.\\ &\qquad\left.-\frac{\omega_b^2}{\Gamma\omega^2}\left(\frac{kV_o}{\omega}\right)^2\right\}-\left(\frac{\omega_b^2}{\Gamma\omega^2}\frac{kc}{\omega}\right)^2=0, \qquad (3.52)\end{aligned}$$

where $V_0 = p_0/(m_e\Gamma)$. Equation (3.52) predicts the instability with the growth rate (Godfrey et al., 1975):

$$\gamma = \omega_p \beta_0 \left(\frac{\alpha}{\Gamma}\right)^{1/2} \frac{kc}{\left(\omega_p^2+(kc)^2\right)^{1/2}}. \qquad (3.53)$$

Now, we will show that the solution (3.53) is only slightly different for a large parallel momentum spread $p_{\parallel,b} \gg p_0$. Assuming $p_{\parallel,b}^{+} \gg mc$ and $p_{\parallel,b}^{-} \ll mc$, we obtain

$$U_1 \approx U_3 \approx \frac{m_e c}{p_{\parallel,b}^{+}} \ln \frac{p_{\parallel,b}^{+}}{m_e c}, \qquad (3.54)$$

$$U_2 \approx \frac{m_e c}{p^+_{\parallel,b}}. \tag{3.55}$$

Neglecting unity in each bracket in equation (3.51) results in the solution

$$\gamma = \omega_p \left[ \alpha \frac{m_e c}{p^+_{\parallel,b}} \ln \frac{p^+_{\parallel,b}}{m_e c} \right]^{1/2} \frac{kc}{\left(\omega_p^2 + (kc)^2\right)^{1/2}}. \tag{3.56}$$

It is easily seen from equation (3.56) that even for $p^+_{\parallel,b} = 10^2 p_0$, the difference between the solutions (3.55) and (3.56) is only a factor of 0.4. Thus, we can neglect the parallel momentum dispersion of the beam and use $p_{\parallel,b} = 0$.

### Case $p_{\parallel,b} = 0$

The dispersion equation for $p_{\parallel,b} = 0$ is derived in Appendix A.2 and has the following form

$$\begin{aligned}
&\left[ 1 - \frac{\omega_{p,p}^2}{\omega^2} - \frac{\omega_{p,e}^2}{\omega^2 - (kv_{\perp,p})^2} - \frac{\omega_{b,\perp}^2}{\omega^2 - (ku)^2} \right] \times \\
&\qquad \times \left[ 1 - \frac{(kc)^2 + \omega_p^2 + \omega_{b,\parallel}^2}{\omega^2} - \frac{(kv_{\parallel,p})^2 \omega_{p,e}^2}{3\omega^2(\omega^2 - (kv_{\perp,p})^2)} - \right. \\
&\qquad\qquad \left. - \frac{(kV_0)^2 \omega_{b,\perp}^2}{\omega^2(\omega^2 - (ku)^2)} \right] - \left[ \frac{kV_0 \omega_{b,\perp}^2}{\omega(\omega^2 - (ku)^2)} \right]^2 = 0,
\end{aligned} \tag{3.57}$$

where $\omega_{b,\perp}^2 = \omega_b^2/\Gamma$, $\omega_{b,\parallel}^2 = \omega_b^2/\Gamma^3$. In principle, one can analyze equation (3.57) analytically, but it is more useful and easier to treat two limiting cases of the cold background plasma and the cold beam.

### Cold background plasma $v_{\parallel,p} = v_{\perp,p} = 0$

Neglecting unity in each bracket in equation (3.57), we obtain that for $p_{\perp,b} \geq p_0(\alpha/\Gamma)^{1/2}$ the solution is purely real (no instability can arise), whereas for $p_{\perp,b} < p_0(\alpha/\Gamma)^{1/2}$ the Weibel mode is unstable for $k < (\omega_p/c)[(\alpha/\Gamma)(p_0/p_{\perp,b})^2 - 1]^{1/2}$ with the growth rate

$$\gamma = \left( \omega_p^2 \beta_0^2 \frac{\alpha}{\Gamma} \frac{(kc)^2}{(kc)^2 + \omega_p^2} - (ku)^2 \right)^{1/2}. \tag{3.58}$$

Let us now assume that the beam obeys a relativistic Maxwellian distribution:

$$f(\mathbf{p}) = \frac{\mu}{4\pi(m_e c)^3 \Gamma^2 K_2(\mu/\Gamma)} e^{-\mu\left[\left(1+\frac{p^2}{(m_e c)^2}\right)^{1/2} - \beta_0 \frac{p_x}{m_e c}\right]}, \tag{3.59}$$

where $\mu = \Gamma\mu_R = \Gamma m_e c^2/(k_B T_b)$, $\beta_0 = V_0/c$. Here, $T_b$ is the temperature of the beam in its rest frame. Then we can evaluate $\Delta p_\perp$ (see Appendix A.3) and write the condition for the Weibel mode stability as

$$\alpha \leq \alpha_W = \frac{2-\pi/2}{\Gamma\mu_R} = \left(2 - \frac{\pi}{2}\right)\frac{k_B T_b}{\Gamma m_e c^2}. \tag{3.60}$$

In the simulations by Sironi and Giannios (2014), magnetic-field fluctuations grew at early times due to the Weibel instability driven by the beam, because $\alpha = 10^{-2}$ and $\alpha_W < 5 \times 10^{-4}$ led to condition (3.60) not being fulfilled. But in the simulations by Kempf et al. (2016), the Weibel mode was suppressed, because $\alpha = 2 \times 10^{-6} < \alpha_W = 10^{-5}$. For a realistic blazar-induced beam, the Weibel instability is also suppressed, since $k_B T_b \approx m_e c^2$ and $\alpha \ll 1/ < \Gamma >$.

**Cold beam** $p_{\perp,b} = 0$

Again neglecting unity in equation (3.57), we can approximate it as

$$E\omega^4 + F\omega^2 + G = 0. \tag{3.61}$$

where

$$E = (kc)^2 + \omega_p^2, \tag{3.62}$$

$$F = \left(kV_0\omega_{b,\perp}\right)^2 + \frac{1}{3}(kv_{\parallel,p}\omega_{p,e})^2 - (kv_{\perp,p})^2((kc)^2 + \omega_p^2), \tag{3.63}$$

$$G = -\left(kV_0\right)^2 (kv_{\perp,p})^2 \omega_{b,\perp}^2. \tag{3.64}$$

The growth rate reads

$$\gamma = \left[\frac{F + (F^2 - 4EG)^{1/2}}{2E}\right]^{1/2} \approx \left[\frac{F + |F|}{2E} - \frac{G}{|F|}\right]^{1/2}. \tag{3.65}$$

If $F > 0$, equation (3.65) describes the classical Weibel instability (Bret et al., 2005) with growth rate

$$\gamma \approx \left(\frac{F}{E}\right)^{1/2} \approx \left(\frac{(kv_{\parallel,p}\omega_{p,e})^2/3 - (kv_{\perp,p})^2((kc)^2+\omega_p^2)}{(kc)^2+\omega_p^2}\right)^{1/2}. \tag{3.66}$$

Due to $v_{\perp,p} \neq 0$, the instability is stabilized at large wave vectors, but at small $k$ the plasma is unstable for $(v_{\parallel,p}/v_{\perp,p})^2 > 3$. These conditions were fulfilled in the simulations by Sironi and Giannios (2014), where there was a growth of the magnetic-field fluctuations at later time around $\omega_{p,e}t \approx 10^4$. In the opposite case, $F < 0$ and assuming that $v_{\perp,p}$ is large enough, equation (3.65) reduces to equation (3.53).

## 3.5 The electrostatic instability for realistic pair beams

In section 3.4, based on our first publication (Rafighi et al., 2017), we presented the analytical model needed to investigate a range of parameters for which the beam evolution should correctly reflect the physics. The earlier results, as well as those of Sironi and Giannios (2014) and Kempf et al. (2016), are based on a monoenergetic beam. In this section, we develop a simple analytical model of plasma instabilities of a realistic pair-beam distribution which is non-monoenergetic. This analytical model is based on our second publication (Vafin et al. (2018)). To investigate the growth rate of the electrostatic instability, the energy distribution of realistic blazar-induced pairs is needed and it is presented in Appendix B.1.

### 3.5.1 Linear growth rate

Since the growth rate of the electrostatic instability is mainly regulated by the momentum distribution of the beam particles, we introduce the normalized momentum distribution function, $f_b(\mathbf{p}) = f_b(\mathbf{p},\mathbf{x})/n_b$. The background plasma is assumed to be cold. Then the dispersion equation for the electrostatic mode from Breizman (1990) reads

$$\Lambda(\mathbf{k},\omega) = 1 - \frac{\omega_p^2}{\omega^2} - \sum_b \frac{4\pi n_b e_b^2}{k^2}\int d^3p \frac{\mathbf{k}\frac{\partial f_b(\mathbf{p})}{\partial \mathbf{p}}}{\mathbf{kv}-\omega} = 0, \tag{3.67}$$

where $n_b$ is the density, and $e_b$ is the charge, of the beam particles, $\omega_p = (4\pi n_p e^2/m_e)^{1/2}$ is the plasma frequency of the IGM of density $n_p$, and $\mathbf{k} = (k_\perp, 0, k_z)$ denotes the wave vector. In our case, the beam is composed of electrons and positrons ($e_b = e$). The ratio $n_b/n_p \ll 1$

is small. Taylor expansion of dispersion relation for small $\omega_i$ and using Cauchy's theorem for the derivatives in complex space leads to the growth rate as

$$\omega_i = -\frac{\Im\Lambda(\omega=\omega_r)}{\frac{\partial\Re\Lambda(\omega=\omega_r)}{\partial\omega_r}}, \tag{3.68}$$

where

$$\Re\Lambda(\omega=\omega_r) \approx 1-\frac{\omega_p^2}{\omega_r^2}, \tag{3.69}$$

and

$$\Im\Lambda(\omega=\omega_r) \approx -\sum_b \frac{4\pi^2 n_b e_b^2}{k^2} \times \int \mathbf{k}\frac{\partial f_b(\mathbf{p})}{\partial \mathbf{p}}\delta\left(\mathbf{k}\mathbf{v}-\omega_r\right)d^3p. \tag{3.70}$$

Eqs. (3.68)-(3.69) yield $\omega_r=\omega_p$ and

$$\omega_i = \omega_p\sum_b \frac{2\pi^2 n_b e_b^2}{k^2}\int \mathbf{k}\frac{\partial f_b(\mathbf{p})}{\partial \mathbf{p}}\delta\left(\mathbf{k}\mathbf{v}-\omega_r\right)d^3p. \tag{3.71}$$

For an ultra-relativistic beam, equation (3.71) from Breizman (1990), yields

$$\omega_i = \pi\frac{n_b}{n}\omega_p\left(\frac{\omega_p}{kc}\right)^3\int_{\theta_1}^{\theta_2} d\theta' \times \frac{-2g(\theta')\sin\theta' + (\cos\theta' - kc\cos\theta/\omega_p)(dg/d\theta')}{[(\cos\theta'-\cos\theta_1)(\cos\theta_2-\cos\theta')]^{1/2}}, \tag{3.72}$$

where

$$g(\theta') = m_e c\int_0^\infty p f_b(p,\theta')dp, \tag{3.73}$$

$\theta$ is the angle between the beam propagation and the wave vector, $\cos\theta_{1,2} = \omega_p[\cos\theta \pm \sin\theta\sqrt{(kc/\omega_p)^2-1}]/(kc)$, and the integration angle $\theta'$ is counted from the beam direction.

### 3.5.2 Electrostatic instability for a beam without perpendicular momentum spread

In this section, we consider the linear electrostatic growth rate for a realistic blazar-induced pair beam, but with no transverse angular spread. It was found that the momentum distribution of produced pairs is strongly collimated along the direction of the initial gamma-rays, and the transverse momentum is around $m_e c/2$, leading to an opening angle of the beam of about $10^{-5}-10^{-4}$ (Miniati and Elyiv, 2013). Given the small transverse component of the momentum it may seem to be reasonable to model the distribution function of a beam propagating along the z-axis as

$$f_b(\mathbf{p}) = f_{b,z}(p_z)\delta(p_x)\delta(p_y), \tag{3.74}$$

where $f_{b,z}(p_z)$ is related to the distribution can be found in the Appendix as $f_{b,z}(p_z) = f_b(\gamma \approx p_z/(m_e c))/(m_e c)$ (equation B.13). Inserting equation (3.74) into equation (3.71), we obtain

$$\omega_i = \omega_p \sum_b \frac{2\pi^2 n_b e_b^2}{k^2} \int_{-\infty}^{\infty} \left[ k_z \frac{\partial f_{b,z}}{\partial p_z} \delta \left( \frac{k_z p_z}{m_e \gamma} - \omega_p \right) - \right.$$

$$\left. - \frac{k_\perp^2 f_{b,z}}{m_e \gamma} \delta' \left( \frac{k_z p_z}{m_e \gamma} - \omega_p \right) \right] dp_z, \quad (3.75)$$

where $\gamma = \sqrt{(p_z/m_e c)^2 + 1}$. equation (3.75) can be rewritten as

$$\omega_i = \pi \frac{n_b}{n_p} \omega_p \gamma_0^3 \left( \frac{\omega_p}{kc} \right)^2 \left[ 2 p_{z,0} f_{b,z}(p_{z,0}) \left( \frac{k_\perp}{k_z} \right)^2 + \right.$$

$$\left. + (m_e c)^2 \left( 1 + \left( \frac{\gamma_0 k_\perp}{k_z} \right)^2 \right) \frac{\partial f_{b,z}(p_{z,0})}{\partial p_{z,0}} \right], \quad (3.76)$$

where $p_{z_0} = m_e c / \sqrt{(k_z c/\omega_p)^2 - 1}$ and $\gamma_0 = \sqrt{(p_{z,0}/m_e c)^2 + 1}$. For the limiting case of the parallel waves, the growth rate reads

$$\omega_{i,||} = \pi \frac{n_b}{n_p} \omega_p \gamma_0^3 \left( \frac{\omega_p}{kc} \right)^2 (m_e c)^2 \frac{\partial f_{b,z}(p_{z,0})}{\partial p_{z,0}}. \quad (3.77)$$

However, the growth rate (3.76) is larger by many orders of magnitude in quasiperpendicular direction $k_\perp \gg k_z$

$$\omega_{i,\perp} \approx \pi \frac{n_b}{n_p} \omega_p \gamma_0^5 \left( \frac{\omega_p}{kc} \right)^2 (m_e c)^2 \frac{\partial f_{b,z}(p_{z,0})}{\partial p_{z,0}} = \gamma_0^2 \omega_{i,||}. \quad (3.78)$$

The growth rate for parallel wave vectors (3.77) is shown in figure 3.3 for two different pair spectra, the approximation was derived from Schlickeiser et al. (2012a) (equation B.14) and our results (equation (B.13)). As can be noted from the figure, the maximum growth rates for parallel wave vectors differ by only a factor of 2.

The growth rate for arbitrary wave vectors is presented in figure 3.4a and figure 3.4b, respectively, for pairs beams with distributions (B.14) and (B.13). It is evident that for a more realistic pair distribution (B.13) the peak of the growth rate is narrower and has a much larger value than for pair distribution (B.14). Since the perpendicular growth rate is proportional to $\gamma_0^2$, the high-energy part of the distribution function (see figure B.2) gives the dominant contribution to the growth rate.

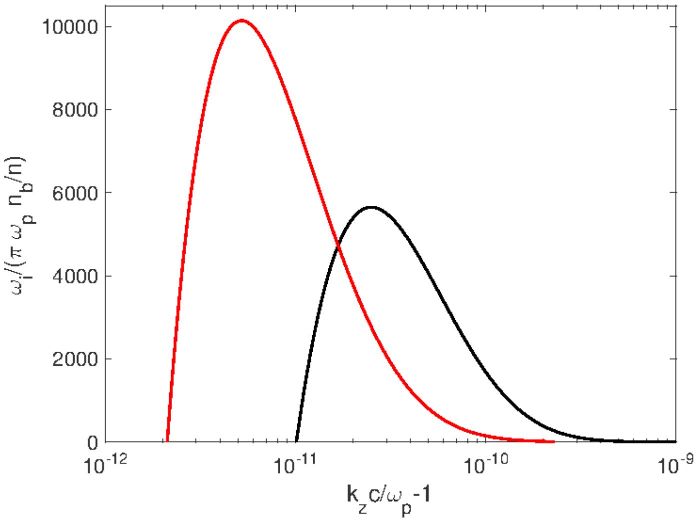

Fig. 3.3 Growth rate of the electrostatic instability for parallel wave vectors for beam with no angular spread and distribution function that was determined by Vafin et al. (2018) (equation B.13, red line) and Schlickeiser et al. (2012a) (equation B.14, black line), respectively.

### 3.5.3 Electrostatic instability for a beam with a finite perpendicular momentum spread

Now, we will consider a finite opening angle of the beam. To do this, we use the distribution function of the form

$$f_b(p,\theta) = f_{b,p}(p) f_{b,\theta}(\theta, p), \tag{3.79}$$

where the transverse distribution can be well approximated by (see the work by Miniati and Elyiv (2013)):

$$f_{b,\theta}(\theta, p) \approx \frac{1}{\pi \Delta\theta^2} \exp\left(-\frac{\theta^2}{\Delta\theta^2}\right) \tag{3.80}$$

and the angular spread for pairs with momentum $p$ can be estimated as $\Delta\theta \approx m_e c/p$ (see the work by Broderick et al. (2012)). The distribution $f_{b,p}(p)$ is derived by transformation from the $z$-integral over equations. (B.4) and (B.9),

$$f_{b,p}(p) = f_b\left(\gamma \approx \frac{p}{m_e c}\right) \frac{d\gamma}{p^2 dp} = \frac{f_b\left(\gamma \approx \frac{p}{m_e c}\right)}{m_e c p^2} . \tag{3.81}$$

The growth rate of electrostatic waves is evaluated by numerically solving equation (3.71). Figure 3.5a a illustrates the growth rate for a beam with the distribution function given by equation (B.14) (Schlickeiser's approximation), whereas figure 3.5b is based on the distribution function found by us and approximated by equation (B.13). The distribution of

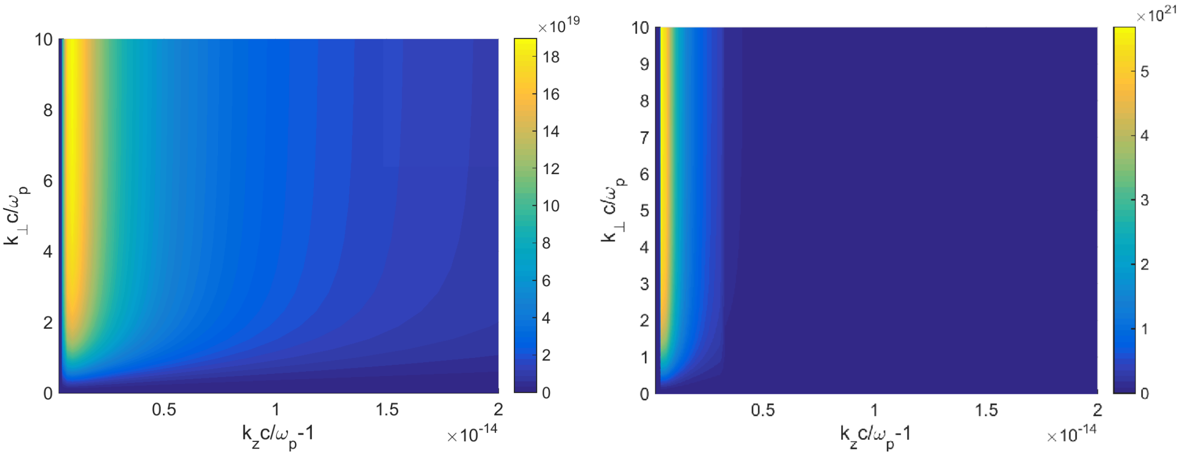

(a) (b)

Fig. 3.4 (a) Normalized growth rate, $\omega_i/(\pi\omega_p(n_b/n_p))$, for a beam with no angular spread and the distribution function from equation (B.14) (Schlickeiser et al. (2012a), $M_c = 2\times 10^6$, $\tau_0 = 10^3$, $\alpha = 1.8$). (b) Same as in (a), but for a beam with no angular spread and a distribution function derived by us (equation B.13).

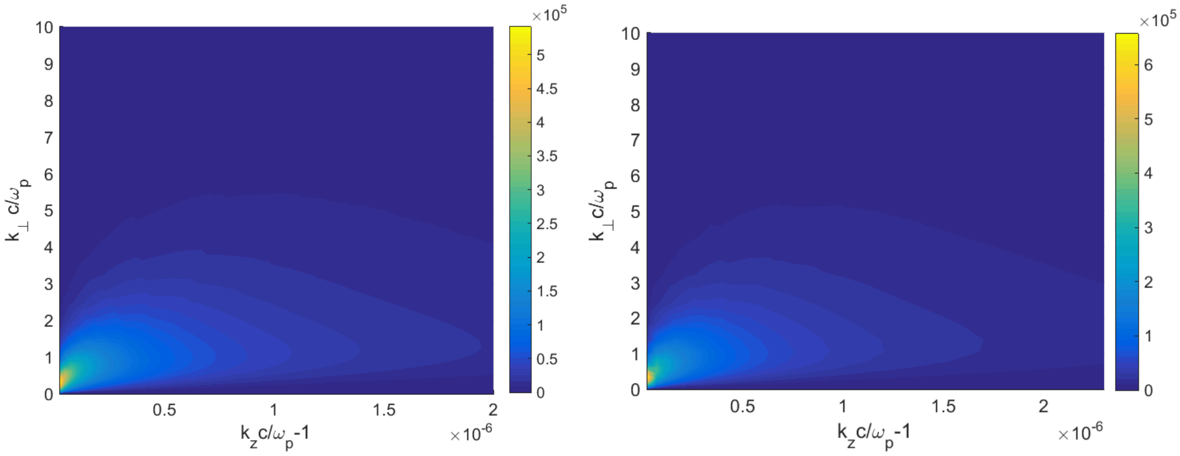

(a) (b)

Fig. 3.5 (a) Normalized growth rate, $\omega_i/(\pi\omega_p(n_b/n_p))$, for a beam with a finite angular spread and the distribution function of equation (B.14). (b) Same as for (a), but for the distribution function of equation (B.13) determined by us.

the growth rate in the wave-vector space is very similar for the two pair distributions, and we can conclude that low-energy pairs that are not included in Schlickeiser's approximation do not really matter.

We find that (i) the growth rate for the beam with a finite angular spread is much smaller compared to the beam with no angular spread and (ii) the maximum growth rate becomes very narrow and lies in the quasiparallel direction ($\theta \approx 16^\circ.7$) to the beam. To be also noted is that the growth rate at oblique wave vectors with $\theta \approx 40^\circ$ is only by a factor 3-5 smaller than the peak value.

The maximum growth rate is

$$\omega_i^{max} \approx 3.2 \times 10^{-6} n_{b,20} n_{e,7}^{-0.5} \text{ s}^{-1} , \tag{3.82}$$

where we adopted $n_b = n_{b,20} 10^{-20}$ cm$^{-3}$ and $n_e = n_{e,7} 10^{-7}$ cm$^{-3}$. This growth rate must be compared to the IC loss time, $\tau_{IC} \approx 10^{20} \gamma^{-1}$ s. Thus, even pairs with Lorentz factor $\gamma \approx 10^9$ will drive the instability for thousands of exponential growth cycles before they loose energy to IC scattering. The important questions are at what level the mode saturates and at which rate the beam energy is depleted while the wave mode is at saturation. While we address the former with PIC simulations, the latter requires an analytical estimate.

# Chapter 4

# Particle-in-Cell Plasma Simulations

The analytical treatments of plasma kinetics rely on the linearisation of the system of Vlasov-Maxwell equations which makes the study of highly nonlinear phenomena almost infeasible. Despite all the approximations used in such treatment, it is still complicated to find a solution. An alternative approach is using computer simulations on supercomputers which still have their own limitations. In this chapter a short overview of the simulation model is presented, followed by an introduction to the simulation code used in this work. The modification we have done to the code in presented in section 4.3.3 and the technical issues that we have investigated through many run tests are discussed in section 4.3.4.

## 4.1 Plasma Simulations Models

Depending on the scale of the plasma system under study, one should choose the appropriate simulation method. For macroscopic systems and collisional plasmas, a hydrodynamic and magnetohydrodynamical (MHD) model are the most preferred approaches. These methods approximate the plasma system as one or more fluids, where the fluid elements have bulk attributes such as density, temperature, pressure, etc., provided the fluid elements represent a large enough volume for the approximation. The temporal evolution of the system consisting of plasma and electromagnetic fields (see, Davidson (2001)) are described by Maxwell's equations of electrodynamics. However, this method is usually based on assumptions (for instance, the Maxwellian distribution of particles), which make the simulation computationally cheaper but not so accurate.

In contrast to MHD models, hybrid simulations focus on more details regarding the distribution function from physical processes. In such method, the evolution of the distribution function of one particle species is of interest. For instance, this method treats electrons with a fluid representation and and uses a particle representation for ions such that one can focus on ion physics. In comparison with MHD, this method replaces the Navier-Stokes equations with the equation of motion for individual particles (which includes the Lorentz force). This also provides more accuracy comparing to MHD and yet still cheaper than a full PIC code.

In the so called Particle-in-Cell (PIC) simulations ( see, Dawson (1983)), with micro-physical scales or a collisionless plasma, a fully kinetic model is needed to study the evolution of the distribution function of all particle species involved. The fundamental plasma parameters like the Debye-length and the plasma frequency are the most common time and length scales of such simulations.

PIC simulations have the advantage of being self-consistent and having a high precision in the representation of real plasma processes. Despite the huge progress in modern computational powers and memory available on high-performance computing clusters (HPC) using advanced parallelisation techniques, this method is still expensive and considered not feasible for the use of realistic parameters with severe limits on the size of problem.

The PIC method can quickly become unstable and noisy; imposing lots of artificial effects on the simulations that one should take with great care and try to suppress these imperfections. However, PIC codes are considered the best simulation tool in a wide range of problems to study the plasma instabilities and general wave-particle interactions; such as laser-plasma interactions, interactions of the solar wind with Earth's magnetosphere. In this thesis, plasma effects on relativistic pair beams from TeV blazars are investigated with a PIC code.

This chapter describes particle-in-cell codes in general, and the PIC code EPOCH used in this study. Also the artificial complications due to simulations restrictions and proposed measures to suppress the imposed limitations are covered.

## 4.2 The Principles of Particle-in-Cell Simulations

Particle-in-Cell simulations are considered the most common tool for a collisionless plasma kinetics. Since the 1970s the algorithm of such codes, have been under contentious development. The early versions of these codes were limited to one-dimensional purely electrostatic codes and the core of PIC algorithms are described in textbooks such as Birdsall and Langdon (2004) and Hockney and Eastwood (1988). Modern PIC codes with the use of modern computational sources can move to higher dimensions of the code (1d, 2d, 3d), at the same time they have capabilities such as using higher order shape functions, using filters to preserve the solution of Poisson's equation, including collisions, ionisation and QED effects, etc.

### 4.2.1 Core collisionless algorithm

The core of a PIC code consists of the particle pusher and the field solver which is presented in next sections. As illustrated in figure 4.1, The overall scheme starts from macroparticles filling computational cells in discrete space “cells” and time “timestep” where the EM field is interpolated from cells to particles’ positions, calculate the force on the particles, update the velocity and distribution of the particles’ current to the cell vertices in a self-consistent manner.

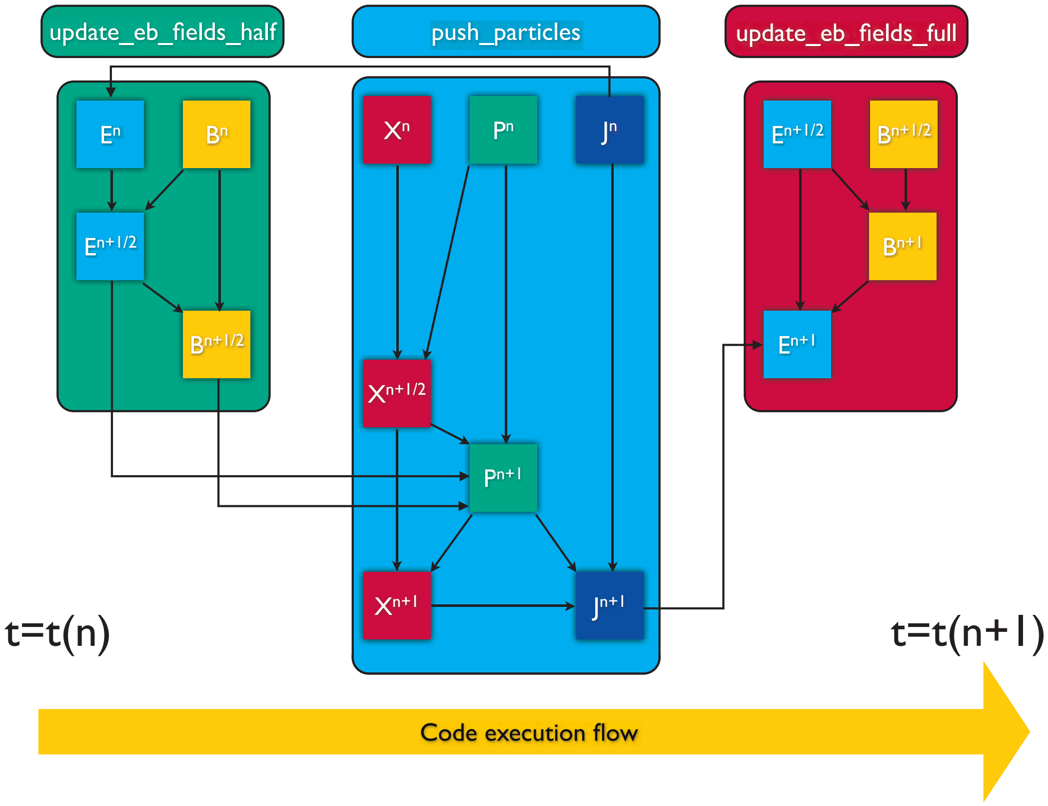

Fig. 4.1 Block diagram of the core routines in a PIC code.[1]

In PIC simulations, for the sampling of the phase space distribution function of particle species $f(\boldsymbol{x},\boldsymbol{p},t)$, the so-called macro particles are used. These macro particles are the probability distribution for an ensemble of Lagrangian markers, which trace the distribution function at certain points in the phase space via Vlasov equation (see Villasenor and Buneman (1992)):

$$\frac{\mathrm{d}f}{\mathrm{d}t} = \frac{\partial f}{\partial t} + \boldsymbol{v}\cdot\frac{\partial f}{\partial \boldsymbol{x}} + \left[\boldsymbol{E}(\boldsymbol{x},t) + \frac{\boldsymbol{v}}{c}\times\boldsymbol{B}(\boldsymbol{x},t)\right]\cdot\frac{\partial f}{\partial \boldsymbol{p}} = 0. \tag{4.1}$$

---

[1] www.cfsapmw.warwick.ac.uk:1731/index.php/EPOCH

From Vlasov equation one can clearly see that if every macro particle is a solution, the total distribution function $f(\boldsymbol{x},\boldsymbol{p},t)$ is then replaced by a sum over all macro particles $\sum_i f_i(\boldsymbol{x},\boldsymbol{p},t)$. Inserting the distribution function of the macro particles into the Vlasov equation (4.1) and taking the first moments with respect to $\boldsymbol{x}$ and $\boldsymbol{p}$ provides macro particle's equations of motion(see Birdsall and Langdon (2004) and Hockney and Eastwood (1988)):

$$\dot{\boldsymbol{x}} = \boldsymbol{v} = \frac{\boldsymbol{p}}{m} \qquad \text{and} \qquad \dot{\boldsymbol{p}} = q\left[\boldsymbol{E}(\boldsymbol{x},t) + \frac{\boldsymbol{v}}{c} \times \boldsymbol{B}(\boldsymbol{x},t)\right], \tag{4.2}$$

where $m$ is the mass of the particle and $q$ is its charge.

Furthermore, the Vlasov equation (4.1) is coupled with Maxwell's equations to form the Vlasov-Maxwell system:

$$\nabla \times \boldsymbol{B} = \mu_0 \varepsilon_0 \frac{\partial \boldsymbol{E}}{\partial t} + \mu_0 \boldsymbol{J}, \tag{4.3}$$

$$\nabla \times \boldsymbol{E} = -\frac{\partial \boldsymbol{B}}{\partial t}, \tag{4.4}$$

$$\nabla \cdot \boldsymbol{E} = \frac{\rho}{\varepsilon_0}, \tag{4.5}$$

$$\nabla \cdot \boldsymbol{B} = 0. \tag{4.6}$$

Finally, we add the sources of the electric and magnetic field to this system by defining

$$\rho = \sum_i q_i \int f_i(\boldsymbol{x},\boldsymbol{p},t)\mathrm{d}\boldsymbol{p}, \tag{4.7}$$

$$\boldsymbol{J} = \sum_i q_i \int \frac{\boldsymbol{p}}{m} f_i(\boldsymbol{x},\boldsymbol{p},t)\mathrm{d}\boldsymbol{p}. \tag{4.8}$$

At each time step, the equations governing these system of equations are solved and it is repeated for the next time step and so on until the time-scale at which we are interested for our physical system to continue.

### Shape-functions

In order to represent these macro particles an interpolation scheme is required such that the per-particle current densities and the charge densities can be accumulated on the simulation grid. The macro particles can be represented by a weight factor $w_i$ and a shape function $S$, where $w_i$ provides the number of real particles inside one macro particle and $S$ describes the shape of the macro particles in phase space:

$$f_i(\boldsymbol{x},\boldsymbol{p},t) = w_i S(\boldsymbol{x} - \boldsymbol{x}_i(t))\delta(\boldsymbol{v} - \boldsymbol{v}_i(t)). \tag{4.9}$$

The so called “nearest grid point” (NGP), is the easiest method, treating all particles as delta-functions in space which is the fastest method but at the same time, the noisiest one. The smoother version “cloud in cell” (CIC) can be achieved by integrating over the delta-function, providing a higher order rectangular particle shape. This can go furtherer to higher orders such as ”triangular shaped cloud” (TSC) and 3rd-order ”BSPLINE” (see figure 4.2).

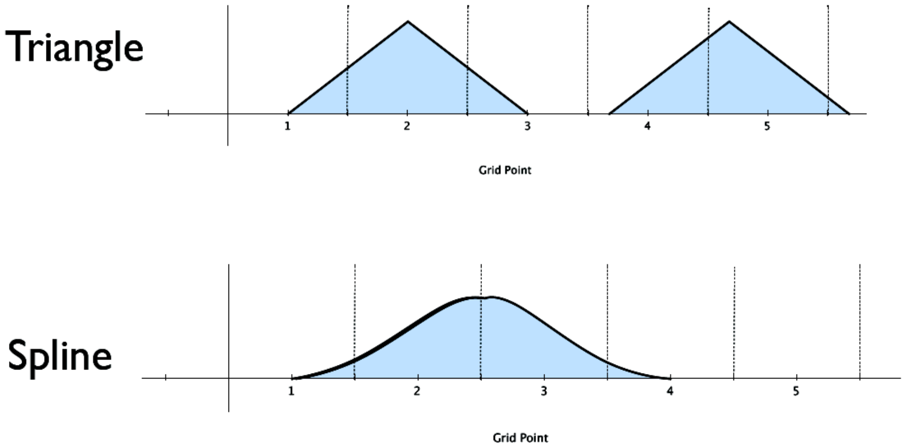

Fig. 4.2 Shape functions.[2]

Implementing a higher order shape function leads to smoother density functions and consequently, a better energy conservation and lower computational noise, because each particle contributes to more and more number of cells. Nevertheless, this also means making the simulation computationally more expensive due to increasing number of cells ( one cell in CIC to four cells in 3rd-order BSPLINE) at every update interval. Another source of artificial noise in a PIC simulation is the number of macro particles which can be suppressed by adding more particles in one simulation cell, which smooths out the current, charge densities and the EM fields in Maxwell’s equations.

### Spatial Grid

In order to store information on the particles and the electromagnetic fields, a computational grid is needed. On a 3D PIC code, it is a three-dimensional lattice of individual cells. The most common method is the so called finite-difference time-domain (FDTD) method proposed by Yee (1966). Figure 4.3 illustrates the grid used in this method. We note that

---

[2] www.cfsapmw.warwick.ac.uk:1731/index.php/EPOCH

the cubic cells are used with a constant cell spacing such that the position of cell i, j, k can be written as $x(i,j,k) = \Delta x(i\hat{x} + j\hat{y} + k\hat{z})$ where $\Delta x = \Delta y = \Delta z$. Furthermore, the field components of **E** are interpolated at points shifted by half a cell, parallel to the direction of the component, while the components of **B** are at the center of the cell, perpendicular to the direction of each component.

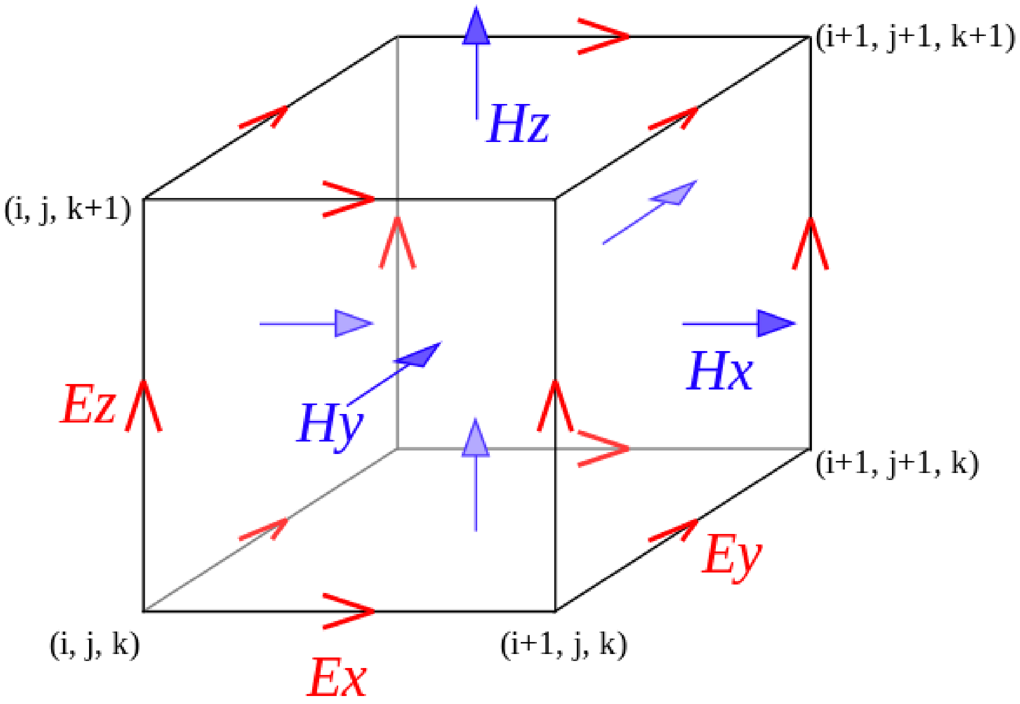

Fig. 4.3 Standard Cartesian Yee cell in 3D, for the finite-difference time-domain (FDTD) method.[3]

### Field Solver

This grid staggering of electric and magnetic fields means that centred, second order accurate derivatives are easily derived, i.e the curl of one field right at the position of the other one. For example $B_z$ at $(i+1/2, j+1/2, k)$ can be updated via,

$$\left(\frac{\partial E_z}{\partial z}\right)_{i+1/2,j+1/2,k} = \frac{E_{y i+1,j+1/2,k} - E_{y i,j+1/2,k}}{\Delta x} - \frac{E_{x i+1/2,j+1,k} - E_{x i+1/2,j,k}}{\Delta y}, \tag{4.10}$$

Using Maxwel’s equations, the FDTD scheme used to advance the fields looks:

---

[3] https://meep.readthedocs.io/en/latest/Yee_Lattice/

- $\vec{E}^{n+\frac{1}{2}} = \vec{E}^{n} + \frac{\Delta t}{2}\left(c^2\nabla \times \vec{B}^n - \vec{j}^n\right)$
- $\vec{B}^{n+\frac{1}{2}} = \vec{B}^{n} - \frac{\Delta t}{2}\left(\nabla \times \vec{E}^{n+\frac{1}{2}}\right)$
- Call particle pusher which calculates $j^{n+1}$ currents
- $\vec{B}^{n+1} = \vec{B}^{n+\frac{1}{2}} - \frac{\Delta t}{2}\left(\nabla \times \vec{E}^{n+\frac{1}{2}}\right)$
- $\vec{E}^{n+1} = \vec{E}^{n+\frac{1}{2}} + \frac{\Delta t}{2}\left(c^2\nabla \times \vec{B}^{n+1} - \vec{j}^{n+1}\right)$

Note that all spatial derivatives are of second order , while higher order spatial derivatives schemes are used in more modern PIC codes. The time-step $\Delta t$ is the CFL limited time-step with restrictions to be discussed shortly.

### Temporal Grid

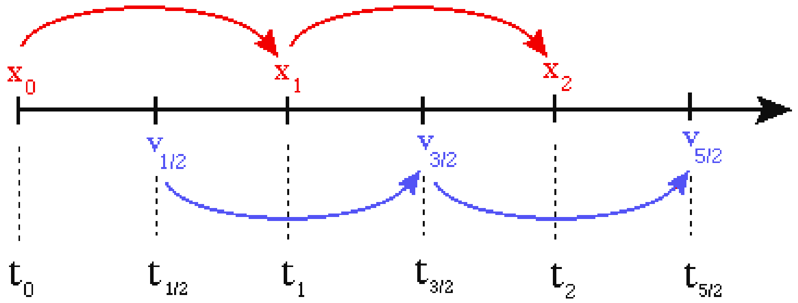

Fig. 4.4 Schematic illustration of the leapfrog intergration method.[4]

The phase space coordinates of the particles are staggered on a temporal grid. The positions of the macro particles $\boldsymbol{x}$ are placed at integer time steps, whereas their velocities $\boldsymbol{v}$ are placed halfway between the integer time steps. This is the so-called leapfrog method (see Birdsall and Langdon (2004)), as illustrated in figure 4.4.

However, the curl operators can differ the dispersion relation of electromagnetic waves $\omega(k)$ from the normal parabolic shape at high k-values. This introduces the so called artificial effect of “grid Cherenkov radiation ” in simulations with highly relativistic beams, propagating close to the speed of light. To avoid this unphysical behaviour, the time-step is restricted such that particles with the fastest speed in the simulation do not cross more than a single grid spacing per step. This leads to an important time-step criteria,

---

[4] https://www.physics.drexel.edu/students/courses/Comp_Phys/Integrators/leapfrog/

$$\frac{c\Delta t}{(\Delta x^2+\Delta y^2+\Delta z^2)^{1/2}} \leq 1, \tag{4.11}$$

where $\Delta x, \Delta y, \Delta z$ are the grid spacings in each direction (see how equation 4.20 is derived).

### Particle pusher

The particle pusher solves the relativistic equation of motion via the Lorentz force. Therefore, the equations of motion (4.2) are replaced by the finite difference equations

$$\frac{\boldsymbol{x}^{t+1}-\boldsymbol{x}^{t}}{\Delta t} = \boldsymbol{v}^{t+1/2} \qquad \text{and} \qquad m\frac{\boldsymbol{v}^{t+1/2}-\boldsymbol{v}^{t-1/2}}{\Delta t} = q\left(\boldsymbol{E}^{t}(\boldsymbol{x}^{t},t)+\boldsymbol{v}^{t}\times\boldsymbol{B}^{t}(\boldsymbol{x}^{t},t)\right), \tag{4.12}$$

where $\Delta t$ is the temporal grid spacing.

The lorentz force on Equation 4.12 is split into separate parts using the common method in PIC simulation known as the Boris rotation algorithm (Boris, 1970). These parts are responsible for the acceleration of the particle and their rotation due to the E and B field, respectively. Also the moving charges, carrying a current should be accounted for. These currents are derived from the particles via the general form of Villasenor and Buneman (1992) current deposition scheme, known as Esirkepov mechansim (Esirkepov, 2001). The Esirkepov algorithm determines not the current itself but its first derivative. This scheme has the property that the electric field is updated from the currents calculated in this way, rather than from moments of the distribution, always satisfies $\nabla \cdot \mathbf{E} = \frac{\rho}{\varepsilon_0}$

## 4.3 Particle-in-Cell Simulations with EPOCH

For our PIC simulation purposes in this work, we use EPOCH 2D written in standard Fortran90 and Message Passing Interface (MPI1.2) to make the code to work in parallel. It is a multi-dimensional, fully electromagnetic, relativistic particle-in-cell code developed by the Collaborative Computational Plasma Physics (CCPP) consortium and funded by the Engineering and Physical Sciences Research Council (EPSRC). EPOCH is a refined version of the basic explicit PIC algorithm with higher-order weights and interpolation schemes. It is based on the older PSC code written by Hartmut Ruhl and retains almost the same core algorithm for the field updates and particle push routines. The code is publicly available at their website [5] and there is an interesting paper about the code by Arber et al. (2015).

---

[5] Epoch code accessible via the url www.ccpp.ac.uk/home/index.shtml.

### 4.3.1 Features of EPOCH

- The EPOCH code uses SI units, although some quantities are given in other units for convenience (for example charges are specified in multiples of the electron charge).
- MPI parallelised, explicit, second-order, relativistic PIC code.
- Dynamic load balancing option for making optimal use of all processors when run in parallel.
- MPI-IO based output, allowing restart on an arbitrary number of processors.
- Data analysis and visualisation options include ITT IDL, LLNL VisIt, Mathworks MatLab and Matplotlib in Python.
- Control of setup and runs of EPOCH through a customisable input deck.

### 4.3.2 EPOCH Characteristics

Despite the huge advancement in modern computer clusters and high-performance computing (HPC) clusters, we are not able to reproduce thoroughly in a simulation. The great challenge is to find a good compromise between the veracity of the model and the computational resources needed to simulate it. Some of the compromises are mentioned below.

#### Dimensionality

EPOCH code is available with different dimensions from 1D to 3D. One should note the physical problem that needs to be investigated through PIC simulations. In this work EPOCH 2D has been used, where the code operates in 2.5 dimensions. This 2D code allows keeping three components for the fields and the particle velocities, but the particles do not have a gradient in the 3rd dimension. Figure 4.5 illustrates the 2.5-dimensional grid used for this work. The 2D version of EPOCH used in this work, reduces the computational expense for the simulation in comparison with the 3D version. Indeed, great care must be taken into account, not to miss important physics. In the current study we are mainly interested in the linear growth of the instabilities, where the non-linear effects can be neglected. Instead of 3D simulations, most of the computational expense is spent in 2D runs with large number of computational particles per cell, that we founds necessary for keeping charge-density fluctuations weak. It is well known that granularity in the charge distribution leads to electric-field noise that causes artificial heating. Suppressing this numerical side effects are

---

[6] EPOCH, *2D Yee grid retrieved from cfsapmw.warwick.ac.uk:1731/index.php/EPOCH*.

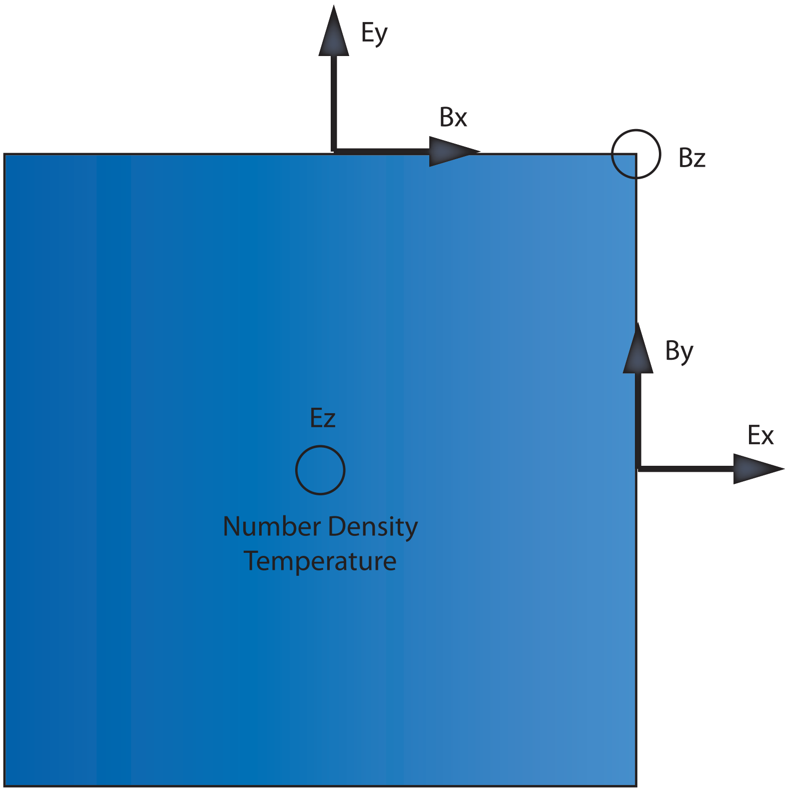

Fig. 4.5 Standard Cartesian Yee cell in 2D, for the finite-difference time-domain (FDTD) method about which electric and magnetic field vector components are distributed.[6]

explained later in section 4.3.4. In fact, the effects of interest in this work do not require a fully three-dimensional setup to occur.

### Particle shape functions

As mentioned in section 4.2.1, macro particles represent many real particles with different shape functions to represent particles. EPOCH can use the following shape functions:

- By default, the code uses a first order b-spline (triangle) shape function to represent particles giving third order particle weighting.
- Top-hat shape function (0th order b-spline yielding a second order weighting)
- 3rd order b-spline shape function (5th order weighting)

### Weight function

The contribution of particles moving through each grid point is its *weight function* or in other words the fraction of macro-particle in cell. The particle weight is calculated as integral of the shape functions in the form $Weight = S(X_j - r_i)$, where the cell j is represented with $X_j$ and particle position with $r_i$.

### Field Order

This is where EPOCH can set the order of the finite difference scheme used for solving Maxwell's equations. The options are 2, 4 or 6 order field solver. If not specified, the default is to use a second order scheme.

### Boundary Condition

The boundaries block sets the boundary conditions of each boundary of the domain. This could have the following forms:

- **periodic** - A simple periodic boundary condition. Fields and/or particles reaching one edge of the domain are wrapped round to the opposite boundary.
- **reflect** -Particles are reflected at the boundary. In case of reflecting fields condition, all field components are clamped to zero.
- **conduct** -Fields would experience conducting boundary conditions. Having applied this condition to particles they would be reflected.
- **open** - Fields would propagate through the boundary and particles are transmitted through the boundary and removed from the system.
- **simple laser** - one or more electromagnetic wave sources can be attached. EM waves impinging on a simple laser boundary are transmitted with as little reflection as possible. Particles are fully transmitted. The field boundary condition works by allowing outflowing characteristics to propagate through the boundary while using the attached lasers to specify the inflowing characteristics. The particles are simply removed from the simulation when they reach the boundary.
- **simple outflow** - A simplified version of the simple laser but more computationally efficient. It has the same properties of transmitting incident waves and particles, but cannot have EM wave sources attached to it.

### Smoothing function

In order to reduce noise and self-heating in a simulation, the smoothing function can be enabled. This applies to the current generated during the particle push. The method is based on the smoothing function used is the same as that outlined in Buneman (1993), but it is a simplified version in the form of a three points filter, called a binomial filter is taken from Vay et al. (2011). This is the most common filter used in PIC simulation codes in which the filtered quantity $\phi_j^f$ can be computed via:

$$\phi_j^f = \alpha\phi_j + (1-\alpha)\frac{\phi_{j-1}+\phi_{j+1}}{2}, \tag{4.13}$$

where the binomial factor is set to $\alpha = 0.5$

### dt-Multiplier

As mentioned in section 4.2.1, the time-step has the criteria to be small, to make sure the simulation remains stable. EPOCH multiples this time-step with factor of dt multiplier. This factor is set to 0.95 by default but can be changed by the user to other numbers smaller than 1. This factor is multiplied to time-step before its applied to the code, i.e. a multiplying factor applied to the CFL condition on the time-step.

Table 4.1 Sobol algorithm with the flipping method.

```
repeat
    generate $X_1, X_2, X_3, X_4$, uniform on (0, 1]
    $u \leftarrow -T \ln X_1 X_2 X_3$
    $\eta \leftarrow -T \ln X_1 X_2 X_3 X_4$
until $\eta^2 - u^2 > 1$.
generate $X_5, X_6, X_7$, uniform on [0, 1]
$u_x \leftarrow u\,(2X_5 - 1)$
$u_y \leftarrow 2u\sqrt{X_5(1-X_5)}\cos(2\pi X_6)$
$u_z \leftarrow 2u\sqrt{X_5(1-X_5)}\sin(2\pi X_6)$
if $(-\beta v_x > X_7)$, $u_x \leftarrow -u_x$
$u_x \leftarrow \Gamma(u_x + \beta\sqrt{1+u^2})$
return $u_x, u_y, u_z$
```

### 4.3.3 Our modifcation to EPOCH

In the analytical model, a particle distribution function was used for the kinetic description of plasma, which was discussed in section 3.4.1. For the PIC simulations also the particle distribution is needed.

EPOCH generates a non-relativistic thermal distribution using the method of Box and Muller (1958) in the form of Maxwellian distribution function by setting the density and temperature for each species which is then used by the autoloader to actually position the particles. However, in our simulations we have highly relativistic beams. Thus, we implemented the algorithm of Zenitani (2015) to set up the relativistic Maxwellian distribution for the beam. The algorithm is presented in a pseudo code in Table 4.1. The Sobol part of the method loads the stationary Maxwellian and the flipping method (equation $-\beta v_x > X_7$) takes care of the spatial part of the Lorentz transformation.

The Sobol method is slower than the inverse transform method, because it uses 6 random variables. But since the algorithm is only used for the initialization of the simulation, it is not a considered as a problem. However, the Sobol method is extremely inefficient in the nonrelativistic limit of $T \ll 1$ KeV. Therefore, we keep using the original Box-Muller method for the distribution function of the IGM background plasma which are immobile.

### 4.3.4 Technical Investigations

Before presenting the simulations in next chapter, a couple of tests which we have performed, are discussed here.

### Cherenkov radiations

As discussed in section 4.2.1, the curl operators in FDTD scheme, can affect the dispersion relation of electromagnetic waves. This leads to artificial effect of "grid Cherenkkov radiation" presented by Godfrey (1974). This effect is due to the scheme imposing a change in the dispersion relation $\omega(k)$ . The phase speed of an EM wave in vacuum is less than speed of light at high k-values, where beams propagating close to the speed of light can interact with these features. Unfortunately, no tested scheme has been able to prevent the instability.

Methods have been developed to suppress this effect. One method is to apply the digital filtering known as Friedmann-filter to waves in high wave number regions. This method has been used in relativistic plasma simulations such as the works by Greenwood et al. (2004); Vay et al. (2011), but the filters may induce numerical damping of physical waves. Another method is the family of spectral methods, where the Maxwell equations are solved in Fourier space. In these methods, the cutoff filter is directly applied in the large wave number region. However, they are in terms of computational cost, under further investigation such as the effort by Vay et al. (2013).

However by careful choice of the CFL number, one could suppress the growth of the numerical Cherenkov instability (see Vay et al. (2011)). Our simulations using EPOCH utilizes explicit FDTD field solvers and the density decomposition method for the current deposit (Esirkepov, 2001), for which a dispersion relation of the numerical Cherenkov instability can be derived.[7]

The fields and the current density are defined on a staggered grid system via :

$$\begin{aligned} \vec{B}^{n+1} &= \vec{B}^{n} + \Delta t\left(\nabla \times \vec{E}^{n+\frac{1}{2}}\right) \\ \vec{E}^{n+\frac{1}{2}} &= \vec{E}^{n-\frac{1}{2}} + \Delta t\left(c^2 \nabla \times \vec{B}^{n} - \frac{\vec{j}^{n}}{\varepsilon_0}\right) \end{aligned} \tag{4.14}$$

**2nd order scheme** In the absence of particles ($\vec{j} = 0$), the 1D second order scheme reduces to

$$\begin{aligned} (B_y)_j^{n+1} &= (B_y)_j^{n} + \frac{\Delta t}{\Delta x}\left((E_z)_{j+1}^{n+\frac{1}{2}} - (E_z)_j^{n+\frac{1}{2}}\right) \\ (E_z)_j^{n+\frac{1}{2}} &= (E_z)_j^{n-\frac{1}{2}} + \frac{c^2\Delta t}{\Delta x}\left((B_y)_j^{n} - (B_y)_{j-1}^{n}\right) \end{aligned} \tag{4.15}$$

Assuming a travelling wave solution of the form $A = A_0 exp(i\omega n\Delta t - ikj\Delta x)$ with the time index n and grid index j, and substituting this in equation 4.15 yields the dispersion relation

---

[7] EPOCH collaboration

for the 1D second order scheme:

$$\sin^2\left(\frac{\omega\Delta t}{2}\right)=\left(\frac{c\Delta t}{\Delta x}\right)^2\sin^2\left(\frac{k\Delta x}{2}\right) \tag{4.16}$$

**4th order scheme** In the absence of particles ($\vec{j}=0$), the 1D fourth order scheme reduces to

$$\begin{aligned}
(B_y)_j^{n+1} &= (B_y)_j^n+\frac{\Delta t}{24\Delta x}\left((E_z)_{j-1}^{n+\frac{1}{2}}-27(E_z)_j^{n+\frac{1}{2}}+27(E_z)_{j+1}^{n+\frac{1}{2}}-27(E_z)_{j+2}^{n+\frac{1}{2}}\right)\\
(E_z)_j^{n+\frac{1}{2}} &= (E_z)_j^{n-\frac{1}{2}}+\frac{c^2\Delta t}{24\Delta x}\left((B_y)_{j-2}^n-27(B_y)_{j-1}^n+27(B_y)_j^n-27(B_y)_{j+1}^n\right)
\end{aligned} \tag{4.17}$$

Again assuming a travelling wave solution of the form $A=A_0 exp(i\omega n\Delta t-ikj\Delta x)$ and substituting it in equation 4.17 yields the dispersion relation for the 1D fourth order scheme:

$$\sin^2\left(\frac{\omega\Delta t}{2}\right)=\left(\frac{7}{6}\frac{c\Delta t}{\Delta x}\right)^2\left[\frac{27}{28}\sin\left(\frac{k\Delta x}{2}\right)-\frac{1}{28}\sin\left(\frac{3k\Delta x}{2}\right)\right]^2 \tag{4.18}$$

**6th order scheme** In the absence of particles ($\vec{j}=0$), the 1D sixth order scheme reduces to

$$\begin{aligned}
(B_y)_j^{n+1} = (B_y)_j^n+\frac{\Delta t}{\Delta x}\Big(&-\frac{3}{640}(E_z)_{j-2}^{n+\frac{1}{2}}+\frac{25}{384}(E_z)_{j-1}^{n+\frac{1}{2}}-\frac{75}{64}(E_z)_j^{n+\frac{1}{2}}+\\
&\frac{75}{64}(E_z)_{j+1}^{n+\frac{1}{2}}-\frac{25}{384}(E_z)_{j+2}^{n+\frac{1}{2}}+\frac{3}{640}(E_z)_{j+3}^{n+\frac{1}{2}}\Big),\\
(E_z)_j^{n+\frac{1}{2}} = (E_z)_j^{n-\frac{1}{2}}+\frac{c^2\Delta t}{\Delta x}\Big(&-\frac{3}{640}(B_y)_{j-3}^n+\frac{25}{384}(B_y)_{j-2}^n-\frac{75}{64}(B_y)_{j-1}^n+\\
&\frac{75}{64}(B_y)_j^n-\frac{25}{384}(B_y)_{j+1}^n+\frac{3}{640}(B_y)_{j+2}^n\Big)
\end{aligned} \tag{4.19}$$

Again assuming a travelling wave solution of the form $A=A_0 exp(i\omega n\Delta t-ikj\Delta x)$ and substituting it in equation 4.19 yields the dispersion relation for the 1D sixth order scheme:

$$\sin^2\left(\frac{\omega\Delta t}{2}\right)=\left(\frac{149}{120}\frac{c\Delta t}{\Delta x}\right)^2\left[\frac{2250}{2384}\sin\left(\frac{k\Delta x}{2}\right)-\frac{125}{2384}\sin\left(\frac{3k\Delta x}{2}\right)+\frac{9}{2384}\sin\left(\frac{5k\Delta x}{2}\right)\right]^2 \tag{4.20}$$

In figures 4.6a to 4.6c, the solutions to equations 4.16, 4.18 and 4.20 are plotted with a range of different values for the courant number $\frac{c\Delta t}{\Delta x}$. The second order scheme for values less than 1 is dispersionless. In case of the fourth order, the scheme becomes unstable when the courant number exceeds 6/7. This analytical method suggests that a CFL condition of 0.8

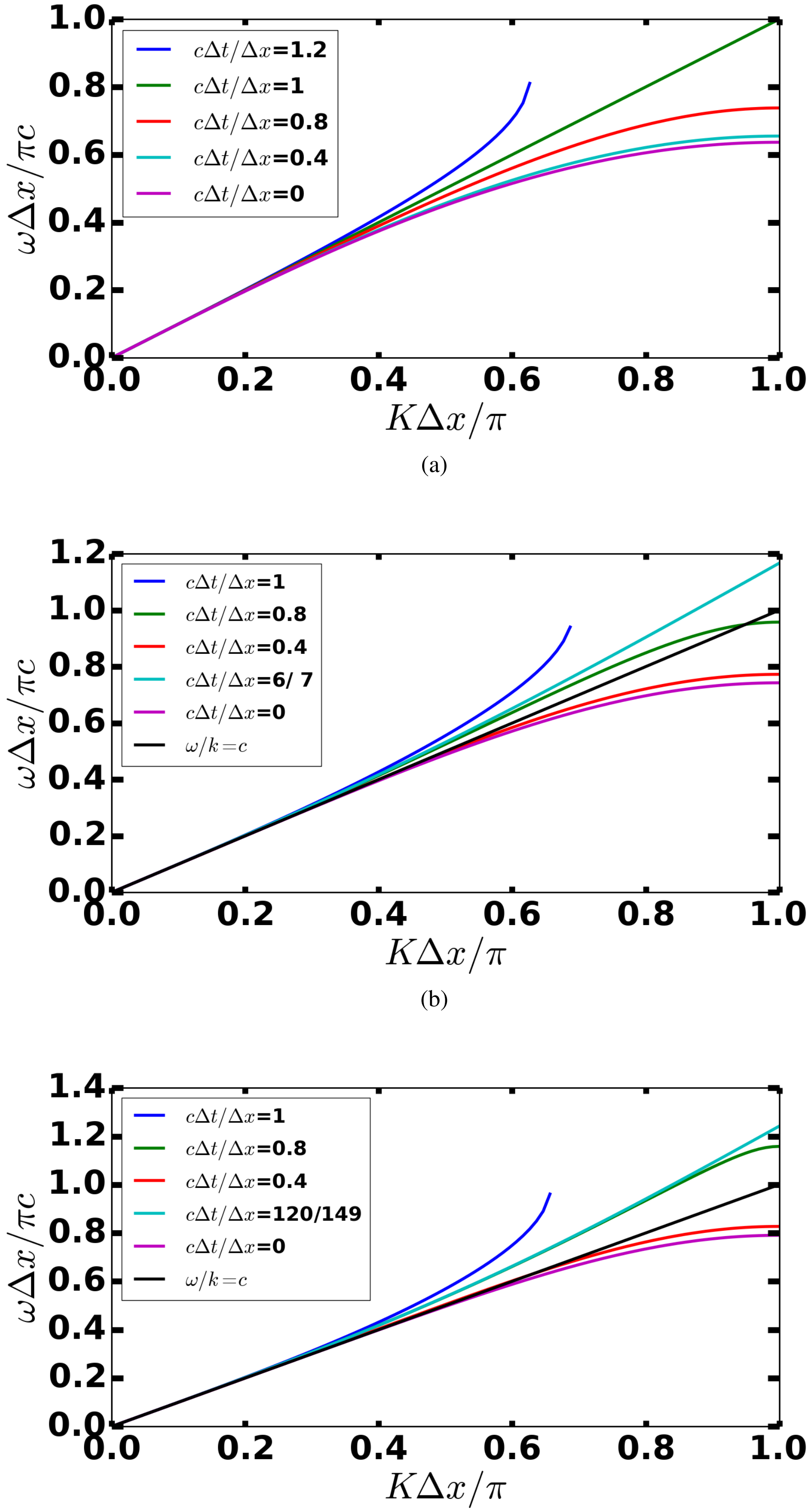

(a)

(b)

(c)

Fig. 4.6 Analytic dispersion curves for (a) 2nd order schemes. (b) 4th order schemes (c) 6th order schemes.

should be fine with all the schemes which we did confirm with our test simulations. Now let us consider the simulations with different schemes and CFL numbers.

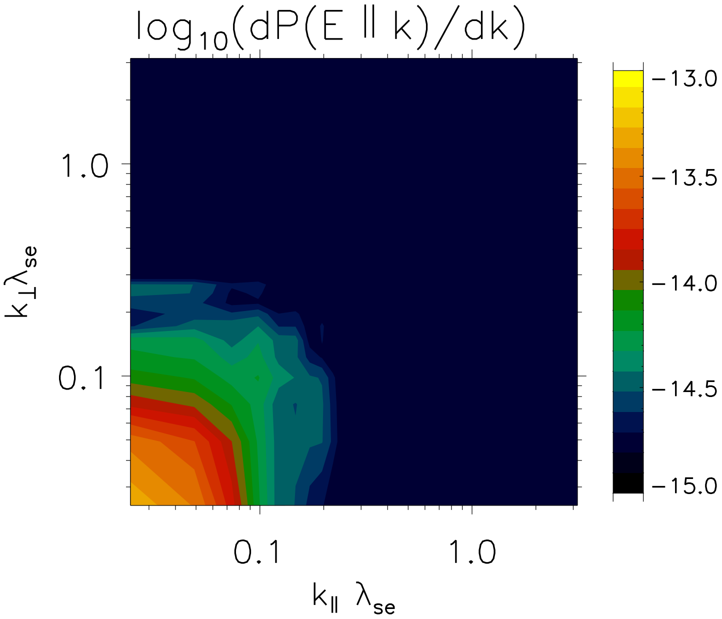

Fig. 4.7 2D Fourier spectra of the electric field energy in a simulation with a relativistic beam with CFL 0.8, current smoothing and field solver 6. The artificial cherenkov radiation pattern is damped without any filtering and thermal noise peaks at low k numbers

Using our EPOCH simulations, the 2D Fourier spectrum of the electric field energy in a simulation is presented in figure 4.7, for a relativistic beam with CFL 0.8, current smoothing and field solver 6. The artificial Cherenkov radiation pattern is damped at large k and thermal noise peaks at low k numbers. The illustrations show that the non-physical phenomenon of Cherenkov radiation is damped without any filtering comparing to simulations with higher CFL number such as 0.95 or simulations without smoothing or the case where the field solver is 2 or 4. Since EPOCH does not support any sort of filtering for such phenomena and after comparison of our test simulations, we will use similar parameters with low CFL numbers, but field solver 6 and enabling the current filter.

### Self-heating and stability

An important consideration in PIC simulations is the so called self-heating. This non-physical effect is caused by not resolving the proper plasma length. To avoid this artificial effect, we have done several tests with EPOCH to see how our code works before the final simulations are performed. These tests were similar to the tests by Arber et al. (2015) (also see Fiuza et al. (2011) for the OSIRIS PIC code).

Table 4.2 Test parameters, $\lambda_D$ is the Debye length and $ppcs$ is number of particles per cell per species

| Runs | $\Delta x/\lambda_D$ | Shape function | $T_p$ | $ppcs$ | $\Gamma_b$ |
|---|---|---|---|---|---|
| Series A | 1,2,0.5 | Tophat-Triangle-Bspline | 2 keV | 25 | 1,5,300 |
| Series B | 1,2,0.5 | Tophat-Triangle-Bspline | 2 keV | 50 | 1,5,300 |
| Series C | 1,2,0.5 | Tophat-Triangle-Bspline | 2 keV | 100 | 1,5,300 |
| Series D | 1,2,0.5 | Tophat-Triangle-Bspline | 2 keV | 200 | 1,5,300 |

For theses tests, the number of grid points in the simulation is fixed for all runs, while varied length of the domains are tested to change the ratio between Debye length, $\lambda_D$ and cell width $\Delta x$ . The number of particles per cell is also varied.

We performed various tests similar to the testes presented by Arber et al. (2015) for energy conversation of EPOCH code. We also performed tests for various shape functions which tophat is the worth amongst them. The triangle one has similar results in comparison with spline. In the case with current smoothing enabled, it shows less self heating in comparison with the case of top hat and triangle but not much difference for spline. Runs with triangle shape function and the smoothing enabled, provides enough self heating suppression, while the spline is still better but more expensive.

We have performed several test-runs to verify how much self heating we have under various parameters. All the simulations were done with $128 \times 128$ grid cells while varying the number of particles per cell and the size of the cells with $\Delta_1 x = \lambda_{se}/8$, also runs with $\Delta_2 x = \Delta_1 x/2$, and runs with $\Delta_3 x = 2\Delta_1 x$. Furthermore, the density was constant for all the tests with the periodic boundary condition. Our final simulations were on a $1024 \times 1024$ grid in a box with a length of $L_x \simeq 128\lambda_{se}$ with the grid size of $\lambda_{se}/8$ and simulations with $2048 \times 512$ grid in a box with a length of $L_{x,y} \simeq 512\lambda_{se} \times 128\lambda_{se}$ with the grid size of $\lambda_{se}/4$. In all these runs, we have chosen the time-step with 0.85 for the CFL condition. The list of different runs is presented in Table 4.2 which confirms the results presented by Arber et al. (2015) in order to avoid self-heating in our simulations.

Numerical noise can introduce a degree of inaccuracy in PIC simulation. Very few particles per cell can introduce significant numerical noise in EM fields. We performed several tests similar to Table 4.2 but with $1024 \times 1024$ and $2048 \times 512$ grids in a box. Typically PIC simulations are performed with 10 particles per cell. Simulations with number of particles per cell higher than 25 smooths the current and charge density leading to reduced high frequency field oscillations due to the source term in Maxwell's equations. Our tests show much lower noise with number particles per cell higher than 100. For the final simulations we took 400 particles per cell per species (i.e. 1600 ppc).

Table 4.3 Test parameters, $\lambda_D$ is the Debye length and *ppcs* is number of particles per cell per species

| Runs | $\Delta x/\lambda_D$ | $ppcs$ | $\Gamma_b$ |
|---|---|---|---|
| Series A | 1,2,0.5 | 25 | 5 |
| Series B | 1,2,0.5 | 50 | 5 |
| Series C | 1,2,0.5 | 100 | 5 |
| Series D | 1,2,0.5 | 200 | 5 |
| Series E | 1,2,0.5 | 400 | 5 |

### Side-band instability

Another artificial effect in PIC simulations is the so-called numerical "Side-band instability". This instability shows up in PIC simulations, where the beam is relativistic and where the simulation box allows for oblique waves. For a detailed description, one can refer to the works of Dieckmann et al. (2006), Kruer and Dawson (1970), Godfrey and Vay (2014).

Generally, such artificial effects occur if electrostatic wave have high enough amplitude, such that it can trap enough number of electrons due to the interpolation scheme between the particles and the grid (Kruer et al., 1969). The trapped particles are considered as the source of this artificial instability, with the maximum growth rates at two wavenumbers around the wavenumber of the large scale electrostatic wave (k0). The term "sideband" refers to plasma waves whose frequency and wavenumber are slightly shifted from the main wave, whereas in 1D, the beam mode $\omega_b = v_b k$ would have sidebands of $\omega = v_b k + \omega_s$ and $\omega = v_b k - \omega_s$. whereas, If one computational particle (CP) moves at a constant speed $v_b$ in a grid cell of $\Delta_x$ then the frequency is $\omega_s = 2\pi v_b/\Delta_x$. The energy of the initial large scale wave is transferred to the "sideband" waves. Our test runs with the parameters provided in Table 4.3 using the triangle shape function, confirm that the effects of this instability can be reduced by selecting a finer grid and more CPs per cell but they can not be suppressed completely.

To sum up, having performed wide range of test runs, we confirmed that the non-physical instabilities and numerical problems have been taken care of in our PIC simulations. Our test runs confirmed that failing to resolve the space would lead to self-heating and aliasing, which could be suppressed by choosing the grid cell size close to Debye length ($\Delta x \approx 0.7\lambda_D$ in our final simulations).

We confirmed that artificial effects of PIC simulations on relativistic beams known as " Cherenkov radiation" and "side-band instability" are reduced by finer grid, more particles per cell and choosing higher order field solvers and shape functions. All the above tests we preformed, have been the foundation of our choosing the parameters for our final simulations presented in Chapter 5.

# Chapter 5

# Simulations

As discussed in the introduction and the analytical part of this thesis, realistic parameters of the pair beams can not be simulated by modern computers. Instead, we use a simple analytical model to find a range of the beam parameters that (i) provides a physical picture similar to that of realistic pair beams and (ii) at the same time can be handled by available computational resources. In this chapter, the performed corresponding two-dimensional (2D) particle-in-cell (PIC) simulations are presented. In section 5.1, the simulations related to monoenergetic beams are presented based on our first publication (Rafighi et al., 2017). Section 5.2 concerns the non-monoenergetic beam simulations based on our second publication (Vafin et al., 2018).

## 5.1 Monoenergitc beam simulations

There is a great challenge of performing plasma simulations despite our modern computational resources. One can not simulate realistic blazar-induced beams. The alternative approach is using parameters that permit numerical modelling with similar physical properties in the simulations. Two important criteria of the realistic pair beams have been noticed before: (i) the beam/IGM energy density ratio is much smaller than unity (Kempf et al., 2016), and (ii) the electrostatic mode evolves in the kinetic regime (Miniati and Elyiv, 2013). However, our simple analytical model evinced that the Weibel mode is actually stable for realistic parameters. This adds a third criterion for the pair beams.

Preceding computational efforts (Kempf et al., 2016; Sironi and Giannios, 2014) considered only some of these requirements on the beam-plasma system. In this work, we have taken into account all the three criteria (run 1). Then, we have compared this case with three other simulations (runs 2-4), for which some criteria were violated.

In this section, we start by presenting the conditions for the the kinetic regime presented in subsection 5.1.1 based on our analytical representation discussed earlier in Section 3.4, followed by the set up of the simulation presented in subsection 5.1.2. Then we proceed with the simulations in subsection 5.1.3. Finally the results are presented in subsection 5.1.4.

### 5.1.1 Condition for the kinetic regime

The work by Breizman (1990) shows that the parallel electrostatic instability evolves in the kinetic regime, if

$$\left|\frac{v_{\|,b}}{c}\right| \gg \alpha^{1/3}\Gamma^{-1}, \tag{5.1}$$

which can be re-written as

$$\alpha \ll \alpha_{kin} = \left(\Gamma\left|\frac{v_{\|,b}}{c}\right|\right)^3. \tag{5.2}$$

An analytical expression for $\alpha_{kin}$ is derived in Appendix A.1 and its functional behaviour is illustrated in figure 5.1.

For the simulation parameters used by Kempf et al. (2016), $\mu_R = 5 \times 10^3$ ($T_b = 10^6$ K), $\Gamma = 10$, and $\alpha = 2.5 \times 10^{-6}$, we obtain $\alpha_{kin} \approx 2.8 \times 10^{-9}$ and equation (5.2) is not fulfilled. For the work of Sironi and Giannios (2014), $\Gamma = 300$, $\alpha = 10^{-2}$, $\mu > 3$, it results in $\alpha_{kin} \approx 7.1 \times 10^{-9}$, and equation (5.2) is not satisfied again. Hence, both Kempf et al. (2016) and Sironi and Giannios (2014) did not simulate the electrostatic instability in the appropriate kinematic regime of pair cascades from AGN.

### 5.1.2 Choice of parameters for PIC simulations

So far, we specified three criteria for a physically relevant setup for the beam-plasma system.

1. The energy density ratio must satisfy $\varepsilon = \alpha\Gamma m_e c^2/(k_B T_p) \ll 1$ yielding

$$\alpha \ll \alpha_\varepsilon(\Gamma) = \frac{k_B T_p}{\Gamma m_e c^2} \approx \frac{10^{-6} - 10^{-3}}{\Gamma}. \tag{5.3}$$

   The behaviour of $\alpha_\varepsilon(\Gamma)$ is shown in figures 5.2, 5.3, and 5.4 as a red line.

2. The electrostatic instability should develop in the kinetic regime at all angles which is determined by equation (5.2), for which we indicate $\alpha_{kin}$ by the green line in the figures.

3. The Weibel mode must be stable which requires satisfying equation (3.60). Equation (3.60) is automatically fulfilled due to $\alpha_{kin} \ll \alpha_W$ for $\Gamma > 1$ and $\mu_R > 1$. Figure 5.1 compares the functions $\alpha_{kin}(\Gamma)$ and $\alpha_\varepsilon(\Gamma)$. To satisfy equations (5.2) and (5.3) for given values of $\Gamma$ and $\mu$, the value of $\alpha$ must be below both curves $\alpha_{kin}(\Gamma)$ and $\alpha_\varepsilon(\Gamma)$.

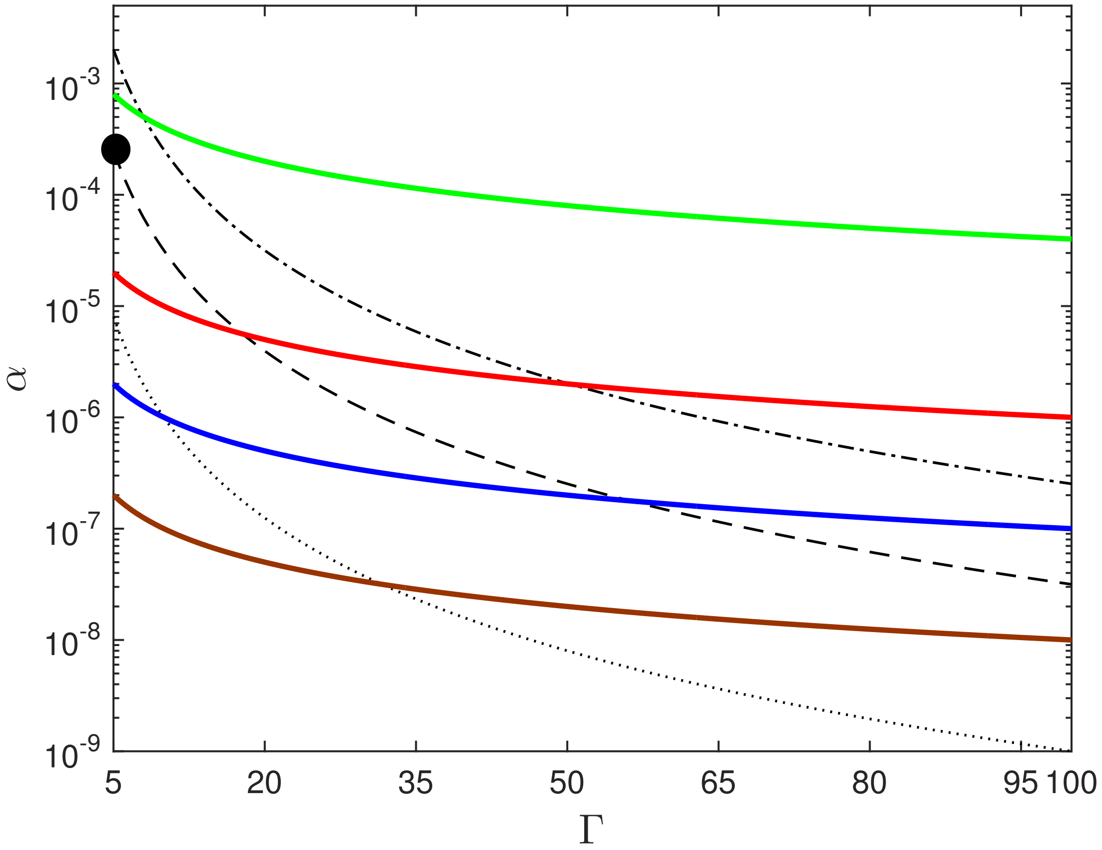

Fig. 5.1 Function $\alpha_{kin}(\Gamma)$: dashed dotted black line $\mu_R = 2.5$; dashed black line $\mu_R = 10$; dotted black line $\mu_R = 100$. Function $\alpha_\varepsilon(\Gamma)$: green line $k_B T_p/(m_e c^2) = 4 \times 10^{-3}$; red line $k_B T_p/(m_e c^2) = 10^{-4}$; blue line $k_B T_p/(m_e c^2) = 10^{-5}$; brown line $k_B T_p/(m_e c^2) = 10^{-6}$. The black point illustrates the parameters chosen for simulation run 1 that satisfies all criteria.

We defined a simulation setup, henceforth referred to as run 1, that would satisfy all criteria. The main parameter values are $\Gamma = 5$ and $\alpha = 2 \times 10^{-4}$, and it is indicated in figure 5.1 by a black dot. In addition, we have specified three other setups (runs 2-4) that are listed in Table 5.1. The goal of these tests is to determine the impact of a violation of one of the criteria on the beam-plasma evolution. For run 2, the energy density ratio $\varepsilon = 2.5$ is higher than unity, and one might expect a strong heating of the background plasma and subsequently the development of other instabilities. Run 3 considers the evolution of the electrostatic instability in the reactive regime ($\alpha > \alpha_{kin}$), and beam energy losses are expected to be larger. Finally, all the conditions are violated for run 4. The values of $(\alpha;\Gamma)$ for runs 2-4 are demonstrated by the black dots in figures 5.2-5.4, respectively.

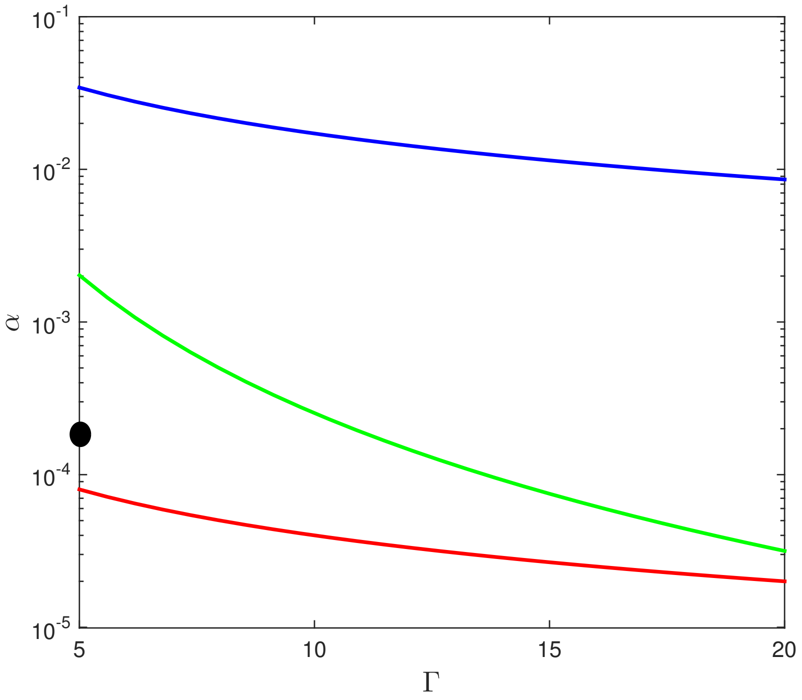

Fig. 5.2 Dependence of all three constraints on the beam Lorentz factor. The green line represents $\alpha_{kin}$, the red line $\alpha_{\varepsilon}$, and the blue line $\alpha_W$. $\mu_R = 2.5$, $k_B T_p/(m_e c^2) = 4 \times 10^{-4}$. The black dot indicates parameter values of run 2.

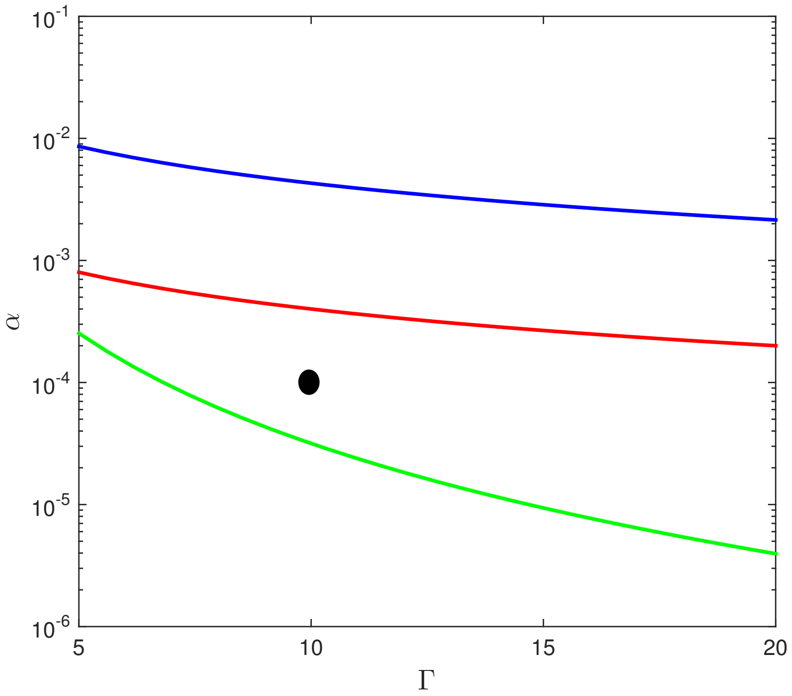

Fig. 5.3 Same as figure 5.2, but for $\mu_R = 10$, $k_B T_p/(m_e c^2) = 4 \times 10^{-3}$. The black dot indicates parameter values of run 3.

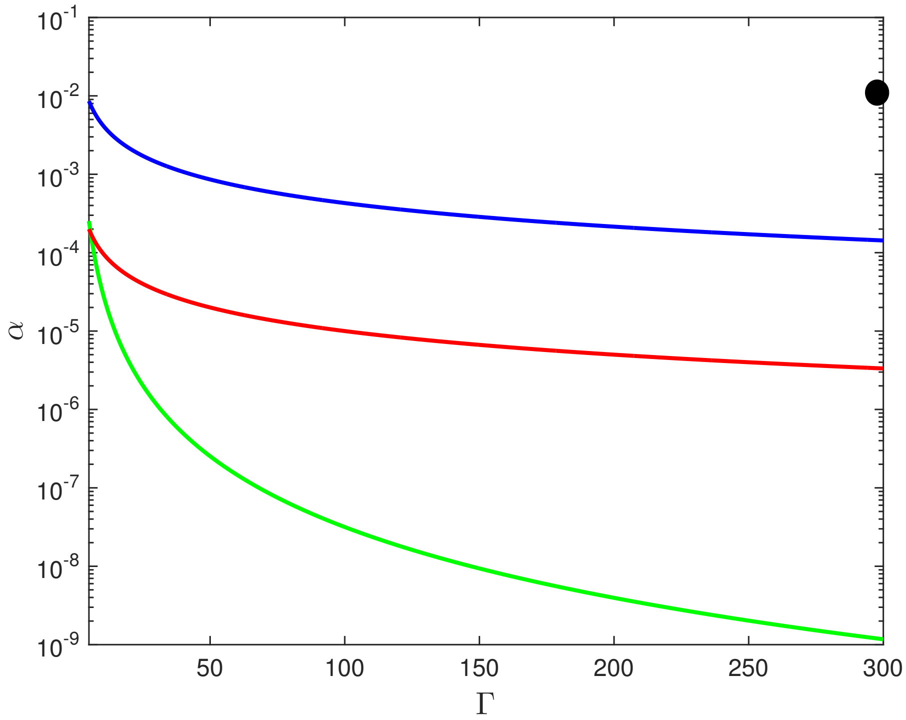

Fig. 5.4 Same as figure 5.2, but for $\mu_R = 10$, $k_B T_p/(m_e c^2) = 10^{-3}$. The black dot indicates parameter values of run 4.

### 5.1.3 The simulation setup

The simulation resolves the x–y plane with periodic boundary conditions, where 2D simulations can address the problem neglecting the out of plane effects, since the instability without external magnetic field only depends on the perpendicular and parallel wave vectors. Furthermore, the periodic boundary condition represents the steady homogeneous beam travelling through the IGM plasma over long distances. The simulation volume is filled with a beam of electrons and positrons and the background plasma of protons and electrons with real mass ratio. We performed a series of tests to verify the stability of the simulation against numerical artefacts. Of particular interest is avoiding artificial plasma heating arising from electric-field noise caused by the charge-density granularity in a particle simulation. We found that using 400 particles per cell and species is required to keep the plasma temperature as desired and the electric-field noise at a level significantly below the intensity of the electrostatic mode. The desired density ratio of beam particles to background plasma, $\alpha = n_b/n$, is established with numerical weights.

As discussed in section 4.3.4, we performed tests runs for our final simulations. For spatial scales, we resolve the electron skin length $\lambda_e = \frac{c}{\omega_{pe}}$ in our simulation, where in case of the electrostatic instability, $k v_b \approx \omega_{pe}$ and $v_b \approx c$. The simulation box contains

Table 5.1 Simulation parameters

| Run | $\alpha$ | $T_b$ | $T_p$ | $\Gamma_b$ |
|---|---|---|---|---|
| 1 | 2.E-04 | 200 keV | 2 keV | 5 |
| 2 | 2.E-04 | 200 keV | 200 eV | 5 |
| 3 | 1.E-04 | 50 keV | 2 keV | 10 |
| 4 | 1.E-02 | 50 keV | 500 eV | 300 |

$1024 \times 1024$ cells, each one eighth of the skin length in size, $\lambda_e = 8\Delta_x$. The timestep is chosen to satisfy the Courant-Friedrichs-Lewy (CFL) condition and to resolve the plasma frequency, $\omega_{pe} = (n_0 e^2/\varepsilon_0 m_e)^{1/2}$. Indeed, IGM proton particles are calculated through the simulations, their effects could be ignored due to their high mass ratio $m_p/m_e = 1836$. This high mass ratio requires to pursue the simulation on much larger time scales ($\omega_{pro} \approx 42\omega_{pe}$) to get a feedback from their interactions.

Table 5.1 lists the parameters of 4 different simulations: temperature of the IGM plasma, $T_p$, and of the beam in its rest frame, $T_b$, density ratio, $\alpha = n_b/n$, Lorentz factor, $\Gamma_b$. The IGM particles are initially at rest, while the beam is moving in x-direction with Lorentz factor $\Gamma_b$. For the IGM, EPOCH code generates a non-relativistic thermal distribution using the method of Box and Muller (1958). However, we implemented the algorithm of Zenitani (2015) to set up the relativistic Maxwellian distribution for the beam. For the graphical presentation we use the following normalization: distance and time are normalized to $\frac{c}{\omega_{p,e}}$ and $\omega_{p,e}^{-1}$, and electric and magnetic fields are given in units of $\omega_{p,e} c m_e/e$ and $\omega_{p,e} m_e/e$, respectively.

In order to reduce the well-known PIC-code phenomena of self heating and statistical noise, all simulations are performed with a high number of CPs (400 particles per species), a 6th-order field particle pusher and a triangular-shaped cloud (TSC) shape function, with the peak of the triangle located at the position of the pseudoparticle.

To sum up, we introduced three criteria for our simulations:

1. The beam/plasma energy density ratio must be less than unity;
2. The Weibel mode has to be stable;
3. The electrostatic instability should develop in the kinetic regime.

Simulation run 1 satisfies all criteria above. Then, we have compared this case with three other simulations (runs 2-4), for which some criteria were violated. In run 2, we considered the beam/plasma energy-density ratio higher than unity. In run 3, the electrostatic instability we considered the reactive regime instead of the kinetic regime. In run 4, all three conditions are violated.

### 5.1.4 Discussion of simulation results

**Run 1**

As mentioned above, for run 1, all relevant criteria for the beam are fulfilled. First of all, the beam/plasma energy density ratio $\varepsilon = 0.5$ for run 1 is smaller than unity. Moreover, the beam is stable with respect to the Weibel instability, while the electrostatic mode grows as expected in the kinetic regime, that is, at the parallel wave vector $k_{||} \approx \omega_p/c$ to the beam.

Figures 5.5a to 5.5c presents the 2D plot of the electric field $E_x$ for three different plasma times of $\omega_{pe}t = 488, 4222, 16238$ in units of $\omega_{p,e}cm_e/e$, where the forming of structures are clearly visible. For comparison, figure 5.5d is the contour of the transverse magnetic field $B_z$ at $\omega_{pe}t = 16238$ in units of $\omega_{p,e}m_e/e$ for run1. Furthermore, figure 5.6a presents the Fourier spectrum of the electric field, and it is evident that an electrostatic mode with $\mathbf{E} \parallel \mathbf{k}$ dominates with peak intensity for wave vectors roughly aligned with the beam direction. The linear growth rate of the electric field is about $\gamma \simeq 4 \times 10^{-4}\omega_{pe}$. The theoretically calculated maximum growth rate for parallel wave vectors is $5 \times 10^{-4}\omega_{pe}$ which approximately agrees with that derived numerically.

Figures 5.7a and 5.7b demonstrate that after $16,237\,\omega_{pe}^{-1}$, corresponding to about eight growth times, the instability has saturated with negligible energy loss and heating of the beam. The latter is of interest because a widening of the lateral beam distribution would impose a temporal smearing of the ICS signal that would reduce the expected flux seen with Fermi-LAT. Our run 1 suggests that this effect is not efficient for realistic pair beams induced by gamma rays from AGN.

Figure 5.6b illustrates the time evolution of the electric and magnetic field energy density. The electric field energy increases and saturates after $\sim 7$ growth times, while the magnetic field grows slightly at late stages which is possibly due to numerical artificial effects. It is clear that the beam transferred only a tiny fraction ($\sim 10^{-4}$ %) of its initial kinetic energy into the electromagnetic fields. Accordingly, the change of the beam distribution is also very small (see figures 5.7a-5.7b). This development of the beam-plasma interaction is caused by the initial momentum spread of the beam. It was also found by Sironi and Giannios (2014) that the beam momentum distribution does not relax to the plateau form when $\Delta p_{\perp,b}/m_e c \sim 1$. The physical reason is that the electrostatic growth rate simply becomes much smaller than in the reactive regime. At the same time, the damping rates of the modulation instability and non-linear Landau damping depend on the resonant wave energy, and therefore they will stabilize the instability at smaller electric field energies.

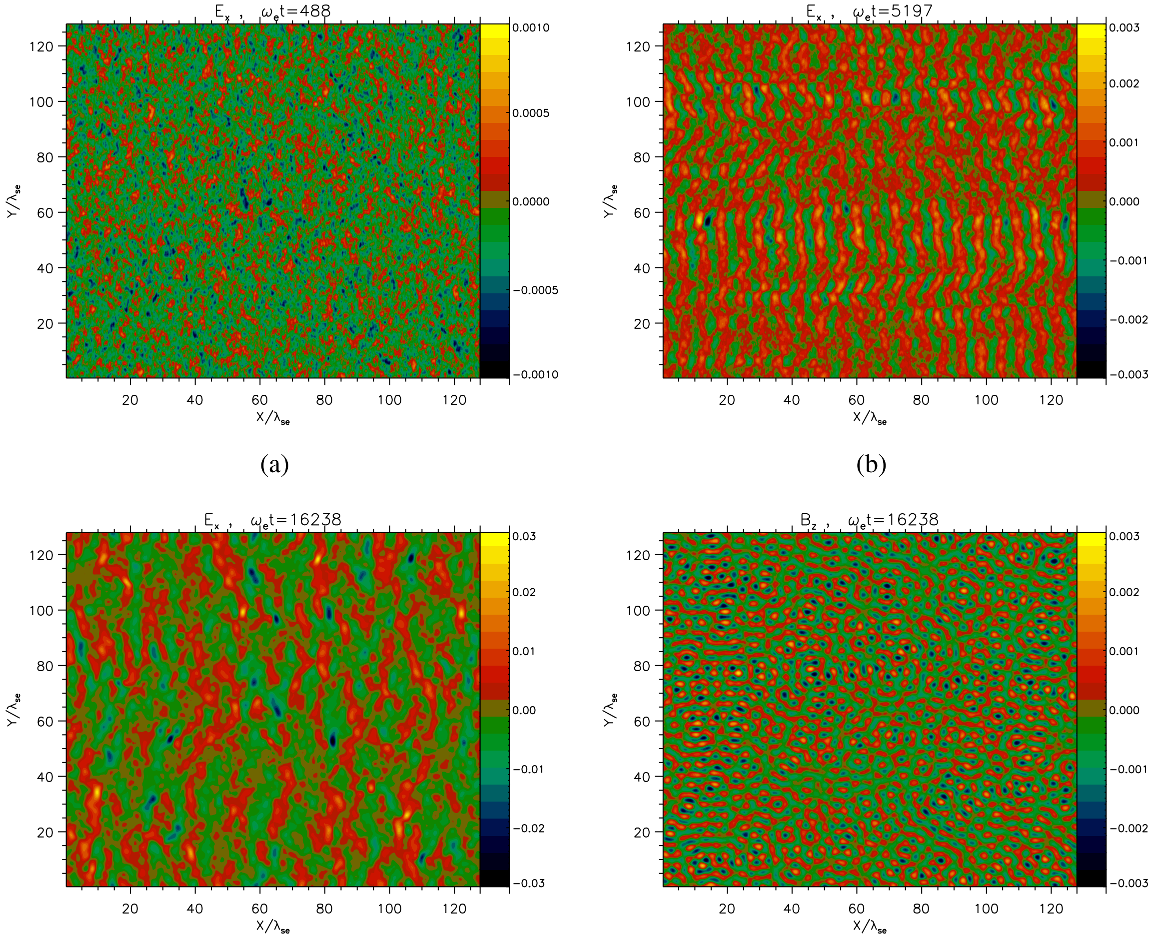

(a) (b)

(c) (d)

Fig. 5.5 Panels(a)-(c) 2D plot of the electric field $E_x$ for three different plasma times of $\omega_{pe}t = 488, 4222, 16238$ in units of $\omega_{p,e}cm_e/e$, (d): 2D plot of the transverse magnetic field $B_z$ at $\omega_{pe}t = 16238$ in units of $\omega_{p,e}m_e/e$ for run 1.

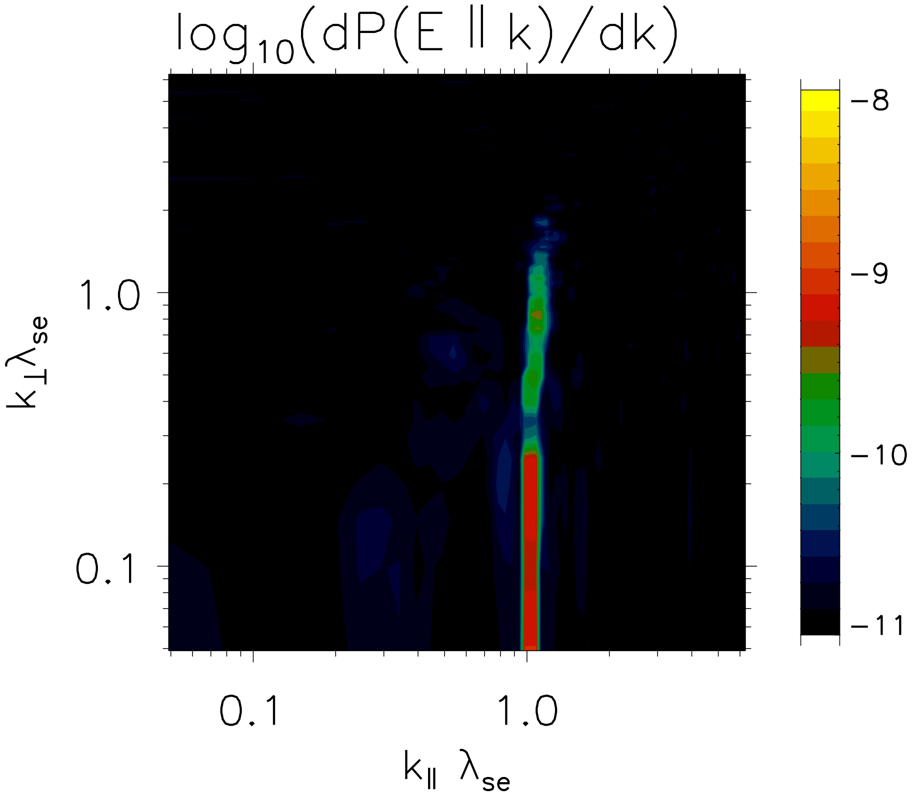

(a)

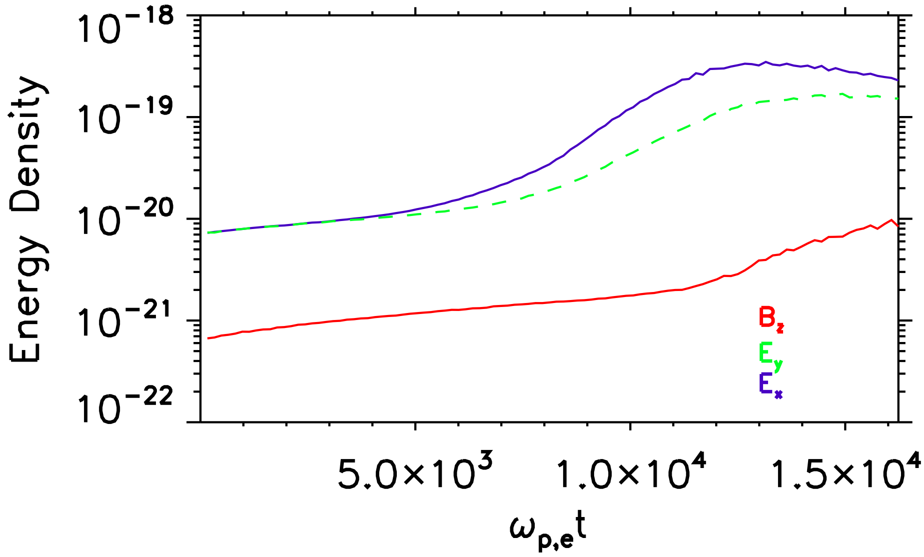

(b)

Fig. 5.6 Figure (a):Two-dimensional Fourier spectrum of $\mathbf{E} \parallel \mathbf{k}$ at $\omega_{pe}t = 4222$ in units of $\omega_{p,e}cm_e/e$, Figure (b): Time evolution of the energy densities of electric and magnetic field, respectively, in SI units for run 1.

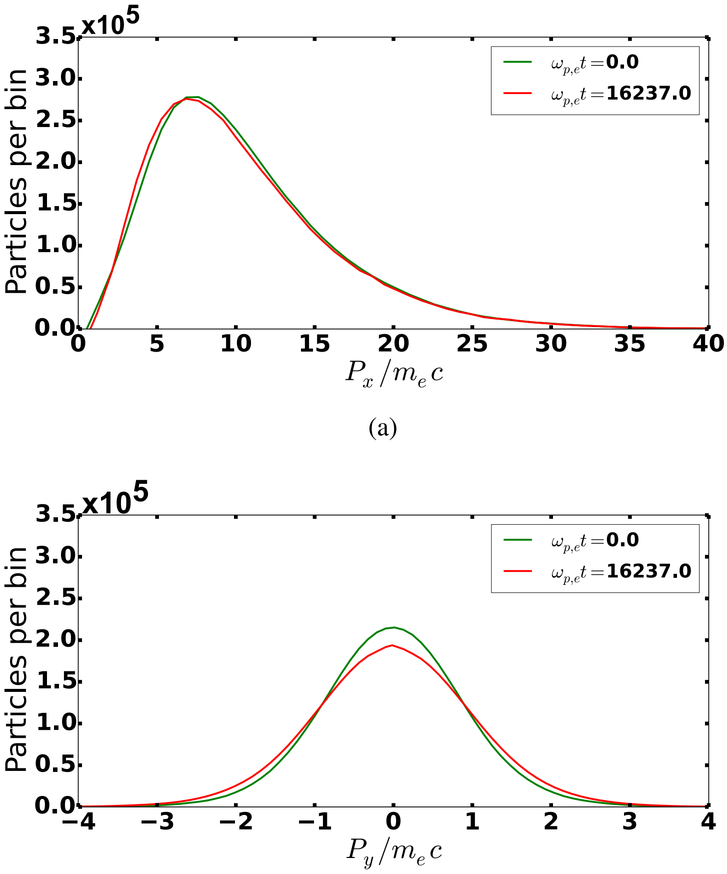

(a)

(b)

Fig. 5.7 Beam momentum distribution for run 1 at two points in time: (a) for $p_x$, (b) for $p_y$.

### Run 2

In contrast to run 1, run 2 considers the beam/plasma energy-density ratio, $\varepsilon = 5$, greater than 1. The only parameter changed compared to run 1 is the plasma temperature that became smaller by an order of magnitude. Due to the fact that the beam parameters remained the same, the Weibel mode is still stable. The electrostatic instability also evolves in kinetic regime with a growth rate of around $\simeq 5 \times 10^{-4} \omega_{pe}$, and the time evolution of the Fourier spectrum (shown in figure 5.8a at $\omega_{pe} t = 5036$) is consistent with the value.

Figure 5.8b shows that the electric field energy density saturates at nearly the same level as in run 1. We note that due to a smaller plasma temperature the initial electric noise level in run 2 is smaller by about an order of magnitude compared to run 1. Although the peak intensity of the electrostatic modes is now observed at a $10^\circ$ angle to the beam direction, the distribution function again did not evolve appreciably, in particular not to a plateau distribution, and the beam experienced only a tiny energy loss or widening.

### Run 3

With run 3, we explore the reactive regime of the electrostatic mode in contrast to runs 1 and 2, where the instability was kinetic. To do this, we have reduced the temperature of the beam and increased its gamma factor. Figures 5.9a to 5.9d presents the 2D plots of the electric field $E_x$ and magnetic field $B_z$ for three different plasma times of $\omega_{pe} t = 564, 4025, 10714$ in units of $\omega_{p,e} c m_e / e$ and $\omega_{p,e} m_e / e$ respectively. Now, the electrostatic instability grows in an oblique direction (at about $30^\circ$) to the beam as is evident from the Fourier spectrum shown in figure 5.10a. The growth rate for oblique propagation and the parameters of run 3 (assuming a cold beam (Breizman, 1990)) is

$$\gamma_{\mathrm{TS}} = \frac{3^{1/2}}{2^{4/3}} \omega_{pe} \left( \frac{\alpha}{\Gamma} \right)^{1/3} \left( \frac{k_{\|}^2}{k^2 \gamma^2} + \frac{k_{\perp}^2}{k^2} \right)^{1/3} \simeq 9 \times 10^{-3} \omega_{pe}, \tag{5.4}$$

where the last equality applies for the parameters of run 3. The numerically determined growth rate is smaller than that by a factor 2-3. This difference may be explained by the fact that run 3 operates not very far from the condition $\alpha = \alpha_{kin}(\Gamma)$ (see figure 5.3).

The instability growth rate of run 3 is larger by an order of magnitude compared to runs 1 and 2. Therefore, we can expect a more substantial modification of the beam. Although the electric-field energy density remains small as shown in figure 5.10b, we observe in figure 5.11 a significant transverse widening of the beam that is not seen in runs 1 and 2. Figure 5.12 indicates that the width of the perpendicular momentum distribution of the beam increased by a factor of 3.

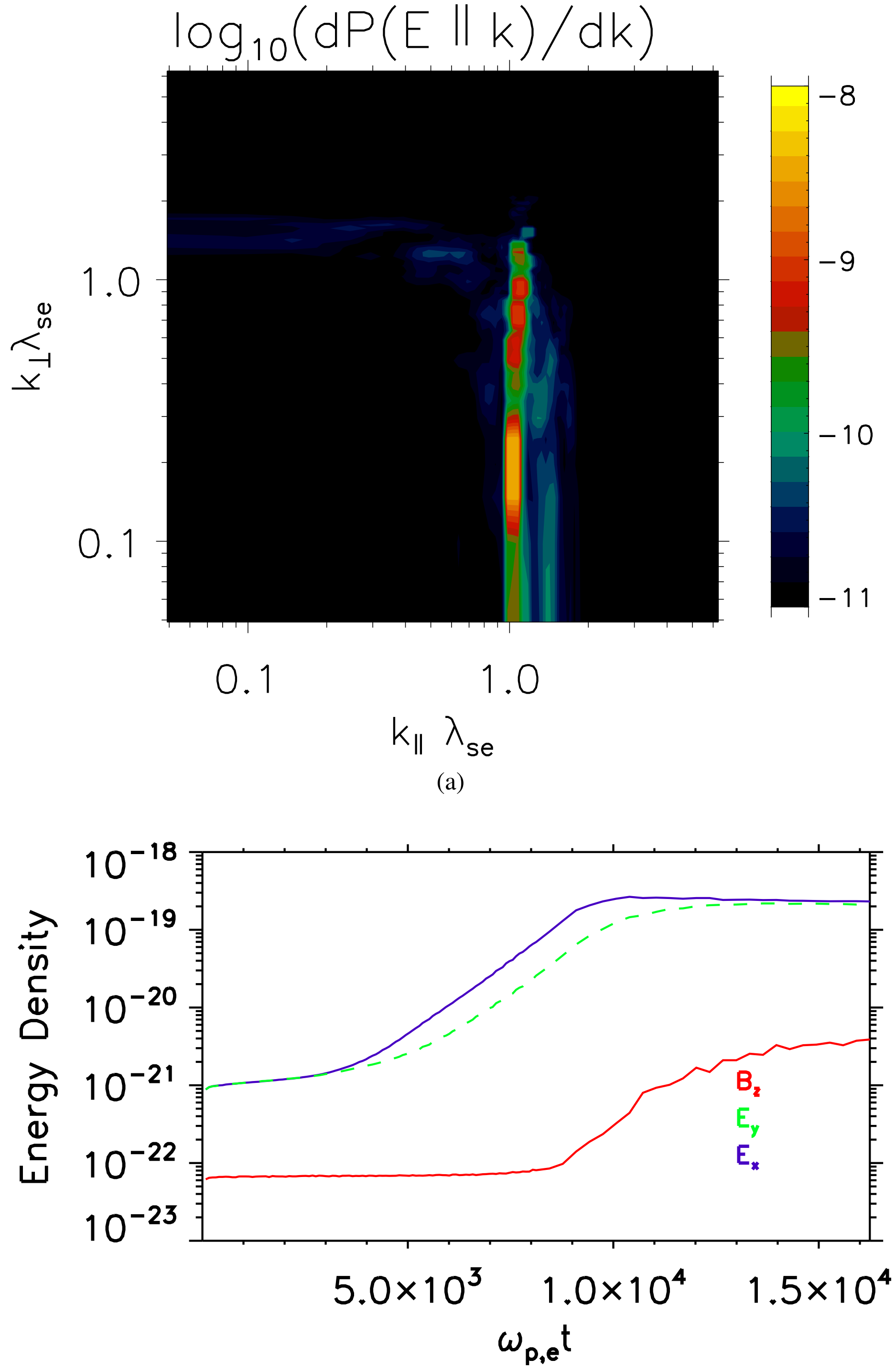

(a)

(b)

Fig. 5.8 Figure (a):Two-dimensional Fourier spectrum of **E** ∥ **k** at $\omega_{pe}t = 5036$ in units of $\omega_{p,e}cm_e/e$, Figure (b): Time evolution of the energy densities of electric and magnetic field, respectively, in SI units for run 2.

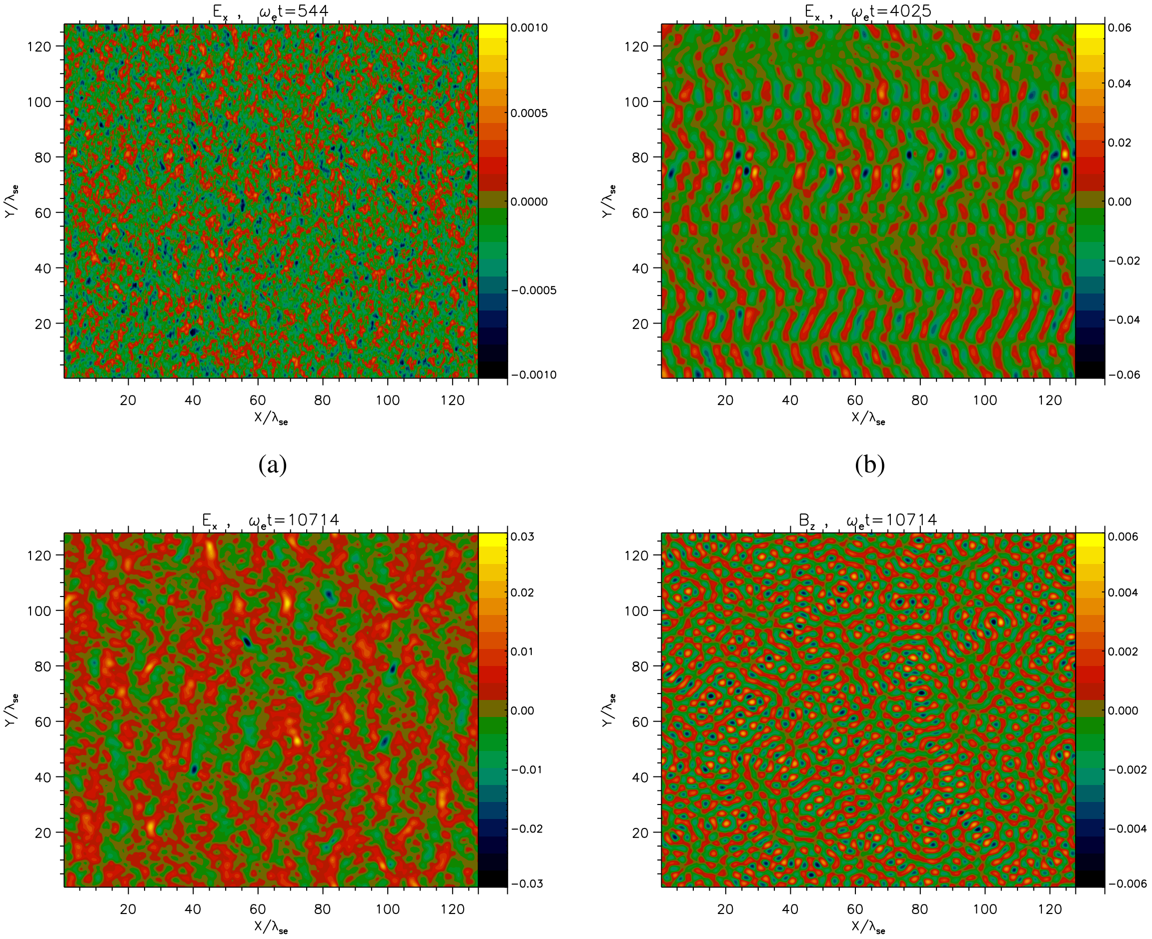

(a) (b)

(c) (d)

Fig. 5.9 Panels(a)-(c) 2D plot of the electric field $E_x$ for three different plasma times of $\omega_{pe}t = 564, 4025, 10714$ in units of $\omega_{p,e}cm_e/e$, (d): 2D plot of the transverse magnetic field $B_z$ at $\omega_{pe}t = 10714$ in units of $\omega_{p,e}m_e/e$ for Run3.

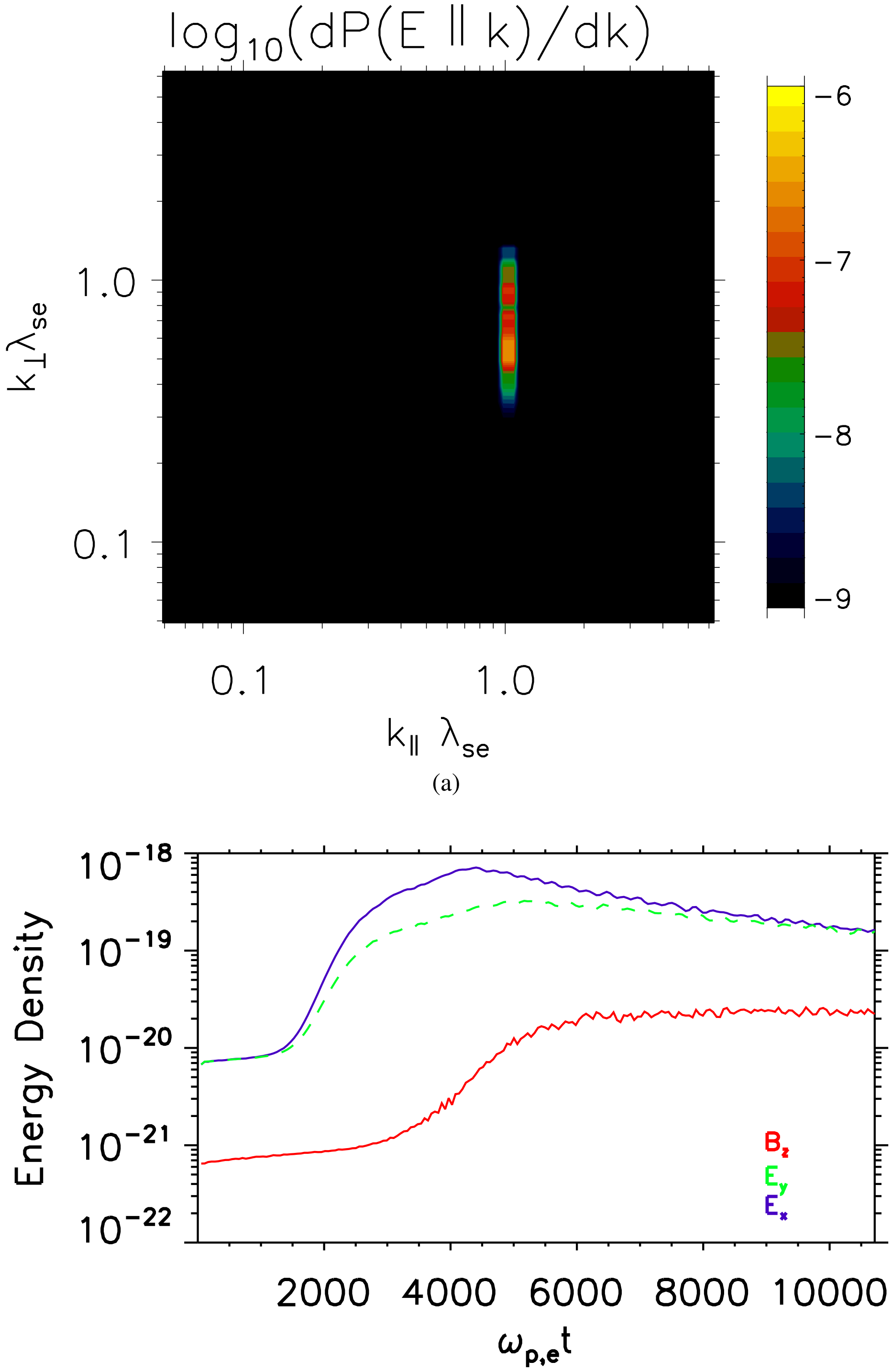

(a)

(b)

Fig. 5.10 Figure (a):Two-dimensional Fourier spectrum of $\mathbf{E} \parallel \mathbf{k}$ at $\omega_{pe}t = 2448$ in units of $\omega_{p,e}cm_e/e$, Figure (b): time evolution of the energy densities of electric and magnetic field, respectively, in SI units for run 3.

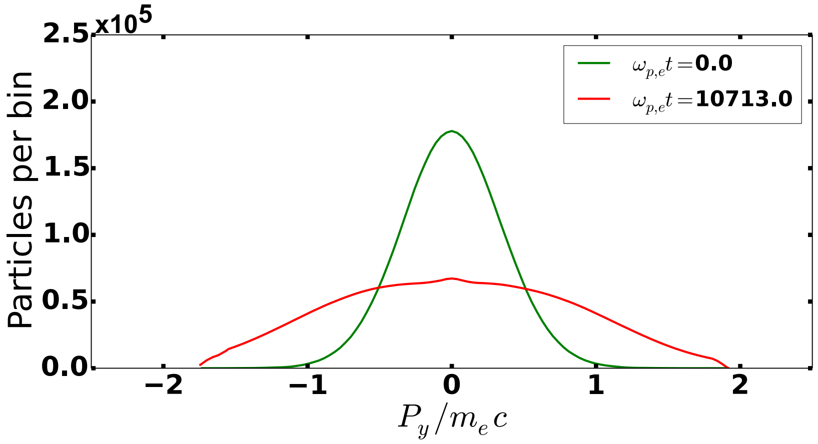

Fig. 5.11 Beam momentum distribution in $p_y$ for run 3 at two points in time.

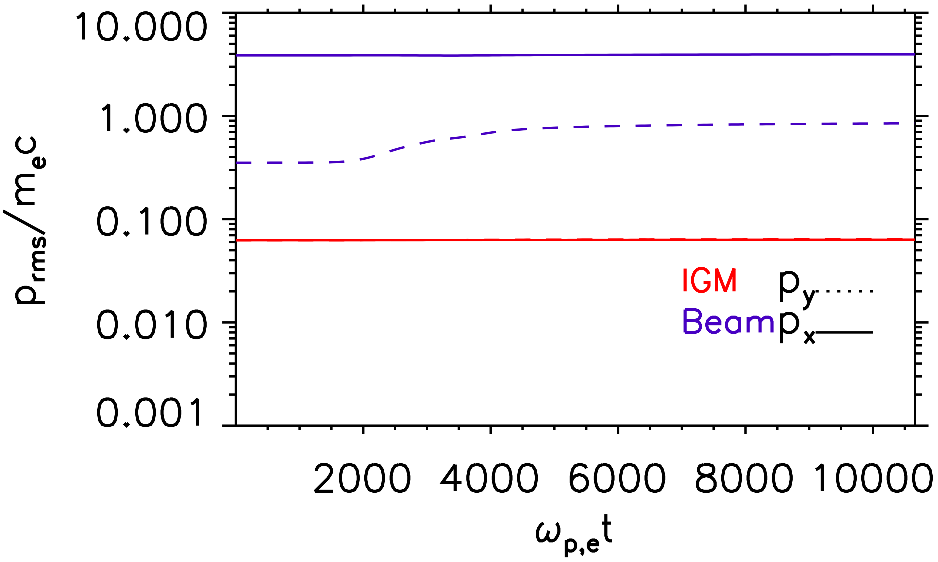

Fig. 5.12 Time evolution of the momentum spread of the beam, $p_{\mathrm{rms}}$, for run 3.

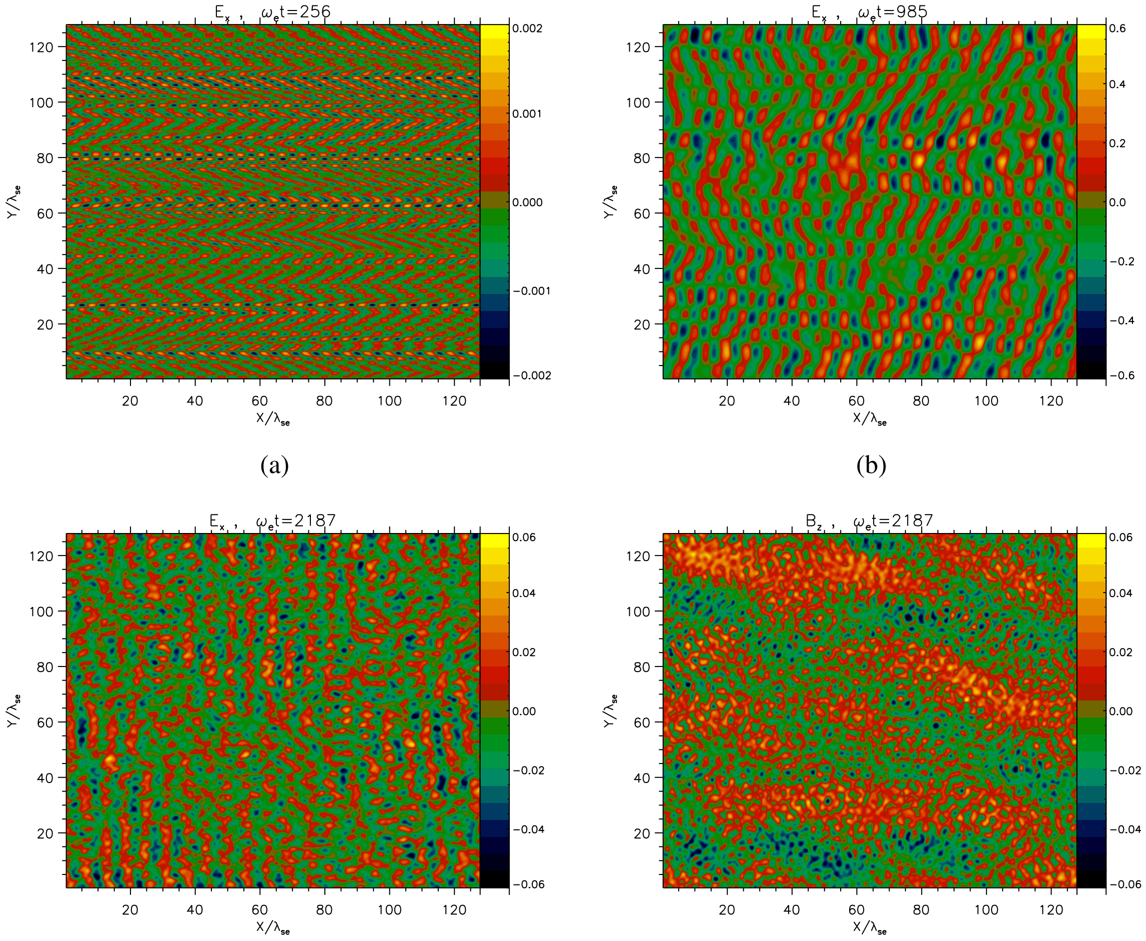

(a) (b)

(c) (d)

Fig. 5.13 Panels(a)-(c) 2D plot of the electric field $E_x$ for three different plasma times of $\omega_{pe}t = 256, 985, 2187$ in units of $\omega_{p,e}cm_e/e$, (d): 2D plot of the transverse magnetic field $B_z$ at $\omega_{pe}t = 2187$ in units of $\omega_{p,e}m_e/e$ for Run 4.

### Run 4

Finally, run 4 considers a situation in which all three constraints on the beam parameters are violated. Unlike runs 1 and 2, the fastest electrostatic mode develops for wave vectors that are quasi-perpendicular to the beam, as is easily seen in figure 5.14a. Figures 5.13a to 5.13d presents the 2D plots of the electric field $E_x$ and magnetic field $B_z$ for three different plasma times of $\omega_{pe}t = 256, 985, 2187$ in units of $\omega_{p,e}cm_e/e$ and $\omega_{p,e}m_e/e$, respectively.

The numerical growth rate perfectly agrees with the analytical estimation for a cold beam, and is about $2.2 \times 10^{-2}\omega_{pe}$ , which is larger than in runs 1, 2, and 3. Furthermore, figure 5.14b demonstrates that the electric-field energy density assumes a considerably higher value than in three other runs on account of a higher growth rate. At the same time, the Weibel

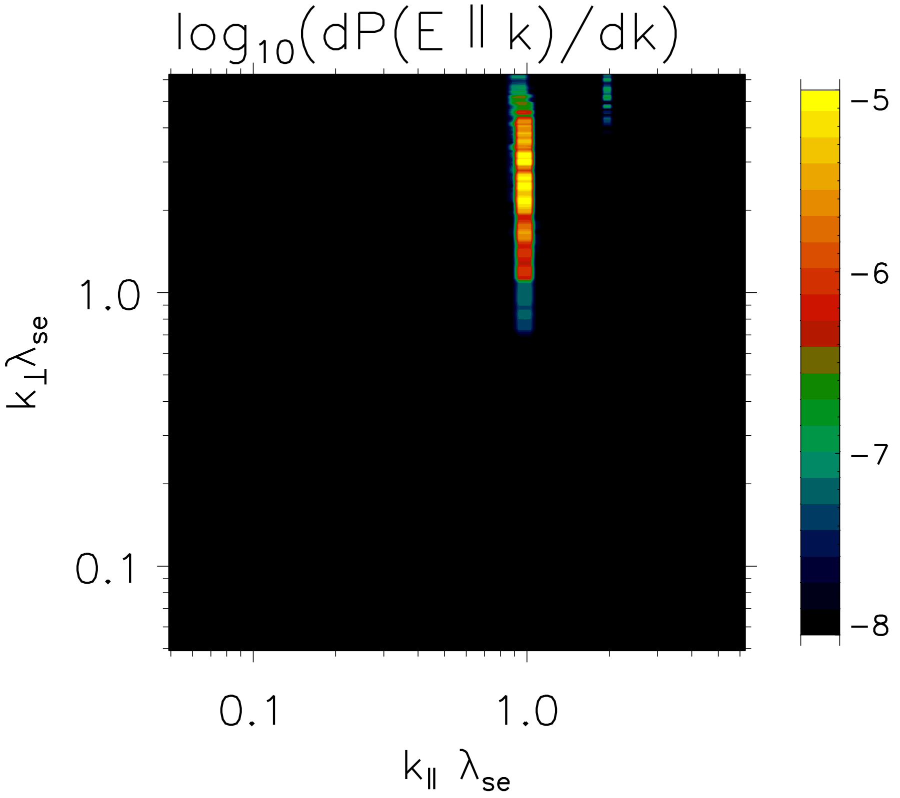

(a)

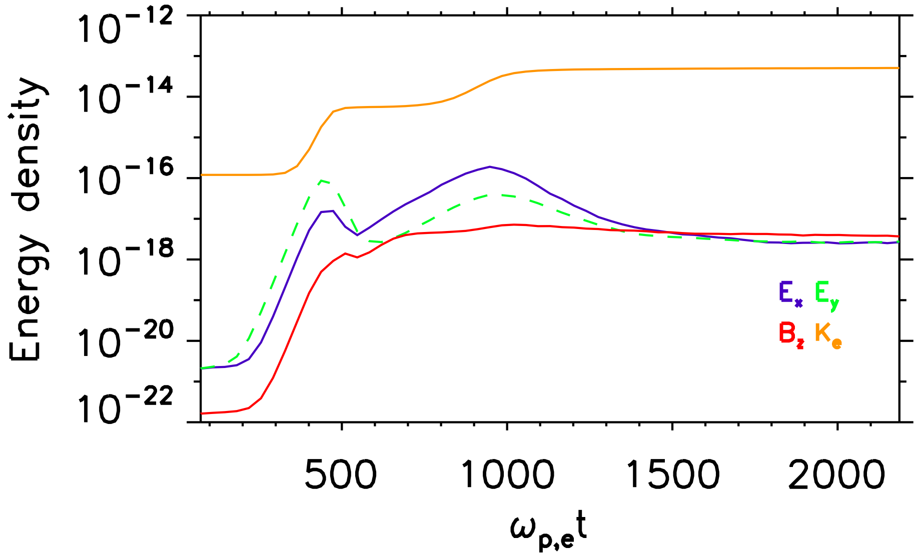

(b)

Fig. 5.14 Figure (a):Two-dimensional Fourier spectrum of **E** $\parallel$ **k** at $\omega_{pe}t = 401$ in units of $\omega_{p,e}cm_e/e$, Figure (b): Time evolution of the energy densities of electric and magnetic field, respectively, in SI units for run 4.

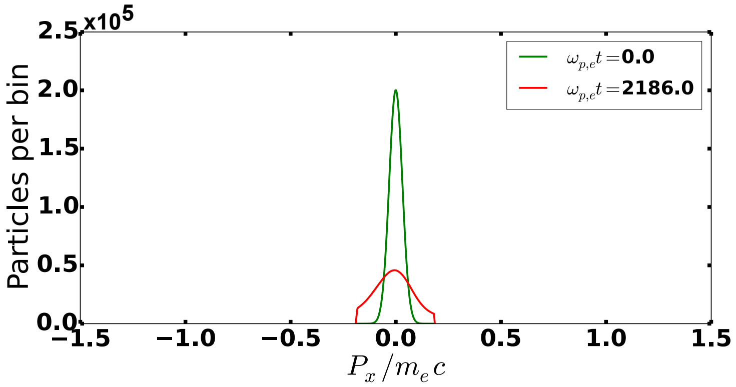

(a)

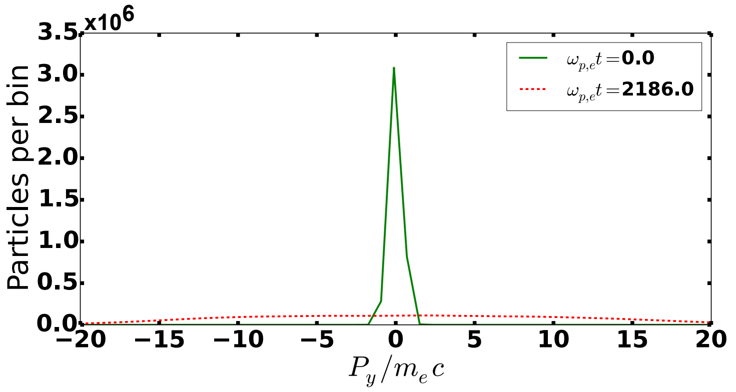

(b)

Fig. 5.15 Momentum distribution for run 4 at two points in time: (a) for $p_x$ of IGM, (b) for $p_y$ of Beam.

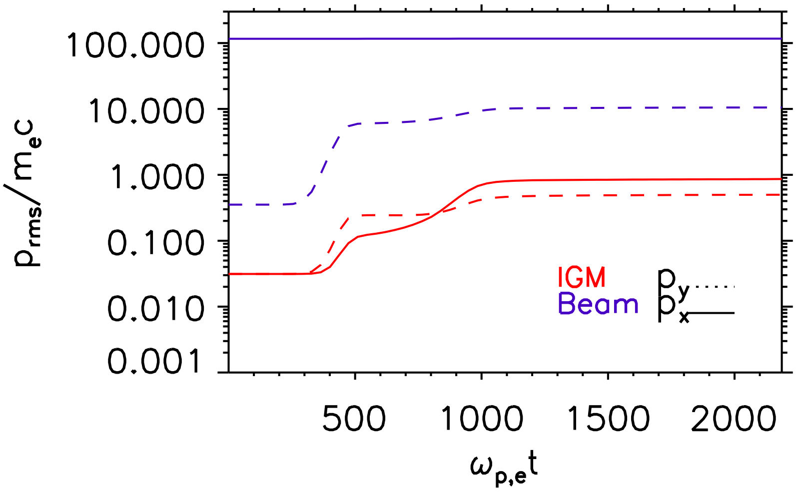

Fig. 5.16 Time evolution of the momentum spread of the beam, $p_{\rm rms}$, for run 4.

mode is destabilized resulting in a strong growth of magnetic field to a field strength even larger (see the red line in figure 5.14b) than that of the electric field. Actually, the orange line in figure 5.14b indicates that the dominant energy transfer is that to IGM electrons ($\sim 0.5\%$), while the magnetic field receives only $\sim 10^{-5}\%$.

This affects the momentum distribution of both the beam and IGM, as we show in figures 5.15a-5.15b. In figure 5.16 we also see a remarkable increase in the momentum spread of the beam and the IGM. This run 4 is similar to the simulations by Sironi and Giannios (2014) who observed a similar beam-plasma evolution.

### 5.1.5 Summary

The largest difficulty is the impossibility to simulate realistic blazar-induced beams, even with modern computational resources. Therefore, parameters must be found that permit numerical modelling with similar physical properties. Two important criteria of the realistic pair beams have been noticed before: (i) the beam/IGM energy density ratio is much smaller than unity (Kempf et al., 2016), and (ii) the electrostatic mode evolves in the kinetic regime (Miniati and Elyiv, 2013). However, the simple estimation presented in the introduction shows that the Weibel mode can potentially compete with the kinetic electrostatic instability. To clarify this point, we have used a simple analytical model and demonstrated that the Weibel mode is actually stable for realistic parameters. This adds a third criterion for the pair beams.

Previous PIC studies of the blazar-induced pair beams (Kempf et al., 2016; Sironi and Giannios, 2014) considered only some of these requirements on the beam-plasma system. In contrast, we have performed a simulation (run 1), for which all of them are taken into account. Then, we have compared this case with three other simulations (runs 2-4), for which some criteria were violated. The results of run 1 indicate that the pair beam does not experience any significant modification. The electrostatic growth rate turns out to be relatively small, and non-linear effects stabilize the beam very efficiently. However, once the electrostatic instability becomes reactive (runs 3-4), as is the case for the studies of Kempf et al. (2016) and Sironi and Giannios (2014), the beam momentum distribution widens drastically in the transverse direction. A significant widening of the beam could in principle account for the observed low flux of cascade gamma rays in the GeV band on account of temporal smearing, but that requires a widening by a factor $\gg 10$. In any case beam widening is only observed if the instability develops in the reactive regime, and that is not relevant for realistic pair beams arising from interactions of AGN gamma rays with extragalactic background light. Also, if the beam/IGM energy density ratio is high, then the beam effectively heats the IGM (run 4), as was seen in the simulations by Sironi and Giannios (2014).

To summarize, we have improved modelling of plasma instabilities for blazar-induced pair beams by including three relevant criteria for the beam. Our results suggest that such instabilities play a negligible role and cannot suppress the flux of cascade gamma rays in the GeV band within our simulation time, but the beam can relaxate on much larger time scales. More details are presented in our discussion of the relaxation time and the conclusions in sections 5.2.3 and 5.2.3.

## 5.2 The electrostatic instability for realistic pair beams

In this section, the simulations results for the case of non-monoenergetic pair beams will be presented. The motivation was to clarify contradicting statements by Schlickeiser et al. (2013) and Miniati and Elyiv (2013). As elaborated in appendix B.1, of interest are BL Lac objects with an intrinsic emission spectrum harder than $E^{-2}$ that extends to at least a few TeV, so that the cascade emission falls into the energy band accessible with the *Fermi*-LAT. This led to a broad pair spectrum ($10^1 < \gamma < 10^8$). Gamma-rays with $E_\gamma = 10$ TeV have a mean-free path of roughly 80 Mpc, i.e., they pair-produce in voids and provide well-detectable cascade emission around 10 GeV. Then, pair beams produced at $D_\gamma \simeq 50$ Mpc represent the best test case for the role of electrostatic instabilities in voids. Based on our analytical representation discussed earlier in section 3.5, the conditions for choosing the parameters for case of wide beam are presented in subsection 5.2.1, followed by the set up of the simulation presented in subsection 5.2.2. Then, we proceed with the simulations in subsection 5.2.3. Finally, the results are presented in subsection 5.2.4.

### 5.2.1 Choice of parameters

As discussed earlier in section 5.1.2 and in our first paper (Rafighi et al., 2017), a realistic blazar-induced pair beam propagating through IGM cannot be simulated numerically due to its very small number density. Nevertheless, a range of beam and plasma parameters can be found such that the problem is numerically accessible with a PIC code, and the physical picture can be extrapolated to the realistic situation. In fact, several conditions must be satisfied (Kempf et al., 2016; Rafighi et al., 2017):

1. The beam/plasma energy-density ratio must be less than unity;
2. The Weibel mode has to be stable;
3. The electrostatic instability should develop in the kinetic regime.

Earlier simulation studies by Kempf et al. (2016); Rafighi et al. (2017); Sironi and Giannios (2014) considered only a monoenergetic Maxwellian beam which is not a good representation of the real situation, because the true pair distribution is highly non-monoenergetic. Maxwellian beams are easy to generate in a simulation (Zenitani, 2015), and an efficient method of inserting a non-Maxwellian beam would be the superposition of two or more Maxwellian beams. As the production of pairs with high center-of-momentum energy is Klein-Nishina-suppressed, and $p_\perp$ is Lorentz-invariant, the Maxwellian beams to be superposed should have the same rest-frame temperature ($kT_b \approx 200$ keV), but will differ in their gamma-factors. Here we present simulations for a composite beam with a normalized distribution function

$$f(p_z,p_\perp) = \frac{w_1\mu_R}{4\pi(m_ec)^3\Gamma_1K_2(\mu_R)}e^{-\mu_R\Gamma_1\left[\left(1+\frac{p_z^2+p_\perp^2}{(m_ec)^2}\right)^{1/2}-\beta_1\frac{p_z}{m_ec}\right]}+ \frac{w_2\mu_R}{4\pi(m_ec)^3\Gamma_2K_2(\mu_R)}e^{-\mu_R\Gamma_2\left[\left(1+\frac{p_z^2+p_\perp^2}{(m_ec)^2}\right)^{1/2}-\beta_2\frac{p_z}{m_ec}\right]}. \tag{5.6}$$

We choose the beam Lorentz factors $\Gamma_1 = 5$ for beam 1 and $\Gamma_2 = 20$ for beam 2. Furthermore, we use $\mu_R = m_ec^2/(k_BT_b)$ and $\beta_{1,2} = (1-1/\Gamma_{1,2}^2)^{1/2}$. The relative weight factors of the beams are $w_1 = 0.9$ (beam 1) and $w_2 = 0.1$ (beam 2). The beam momentum distribution integrated over the transverse momentum is shown in figure 5.17 and designed to resemble the high-energy part of the expected pair distribution displayed in figure B.2. Our discussion of the linear growth rate in section 3.5.3 indicated that it is this high-energy part that matters. We shift it to low Lorentz factors to render the PIC simulations numerically stable. The simulation time is long enough to follow the electrostatic instability, while keeping it in the kinetic regime. The linear growth rate of the electrostatic instability is displayed in figure 5.18. The growth rate has its peak value in the quasi-parallel direction, $20-25°$ to the beam which approximately reproduces the growth rate for the realistic pair beam (figure 3.5b).

We chose the beam/plasma density ratio equal to $\alpha = 2\times10^{-4}$ and the background plasma temperature 2 keV. Then the beam/plasma energy density ratio is about $\varepsilon = 0.66$ which is smaller than 1. Moreover, the Weibel mode is stable, since the condition $\langle p_\perp\rangle > \langle p_\parallel\rangle\,(\alpha/\langle\Gamma\rangle)^{1/2}$ is fulfilled for the beam (Rafighi et al., 2017).

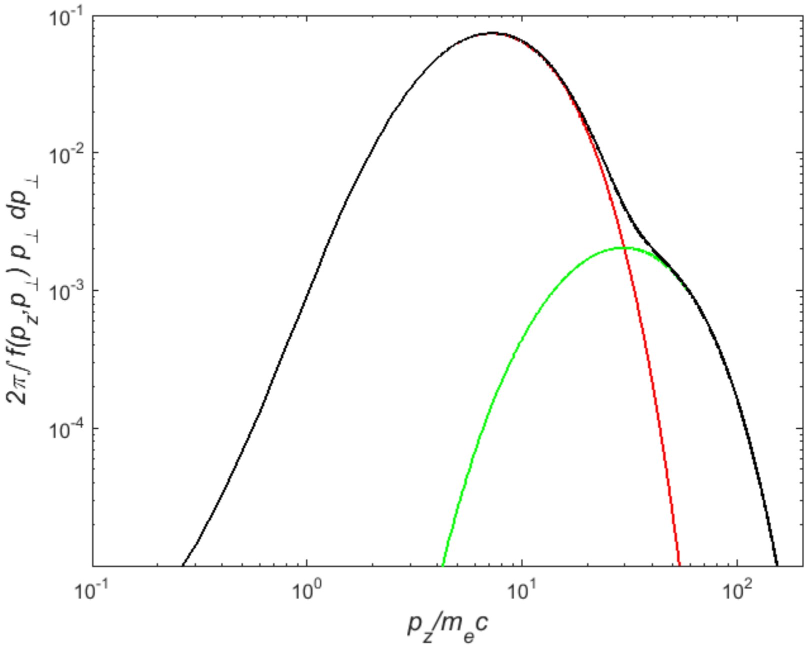

Fig. 5.17 Composite beam distribution function used for PIC simulations. Red: beam 1 ($T_b = 200$ keV, $\Gamma_1 = 5$, $w_1 = 0.9$). Green: beam 2 ($T_b = 200$ keV, $\Gamma_2 = 20$, $w_2 = 0.1$). Black: the total distribution.

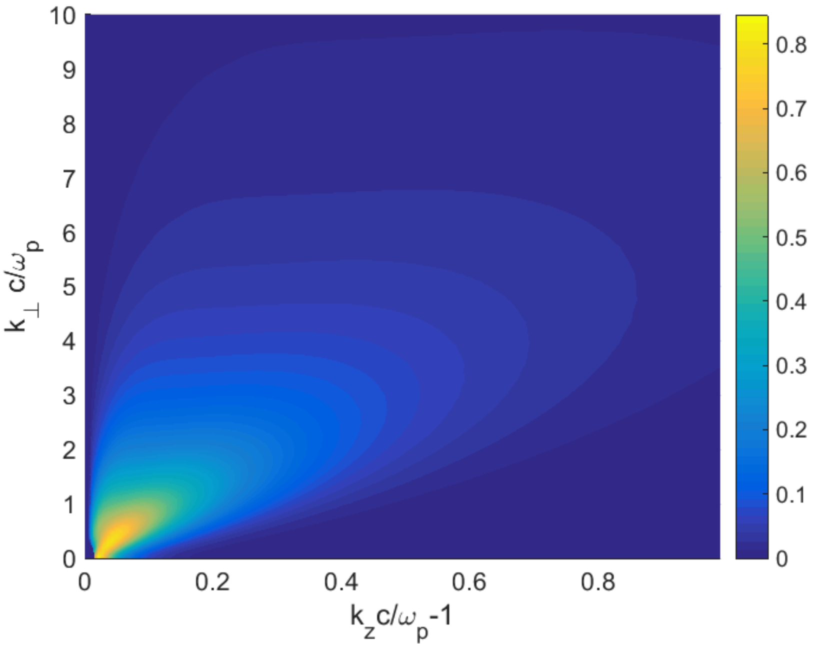

Fig. 5.18 Normalized growth rate, $\omega_i/(\pi\omega_p(n_b/n_p))$, for the composite distribution function used in PIC simulations and displayed in figure 5.17.

Table 5.2 Simulation parameters for composite beams with $\Gamma_1 = 5$ and $\Gamma_2 = 20$.

| Parameter | | run 1 | run 2 |
|---|---|---|---|
| Density ratio | $\alpha$ | $2 \times 10^{-4}$ | $2 \times 10^{-4}$ |
| Plasma temperature | $T_p$ | 2 keV | 2 keV |
| Beam temperature | $T_b$ | 200 keV | 200 keV |
| Weight for beam 1 | $w_1$ | 1 | 0.9 |
| Weight for beam 2 | $w_2$ | 0 | 0.1 |
| Energy density ratio | $\varepsilon$ | 0.5 | 0.66 |

### 5.2.2 Simulation setup

As mentioned earlier in section 5.2.1, we used two beams with relative factors of $w_1 = 0.9$ (beam 1) and $w_2 = 0.1$ (beam 2). For comparison between one- and two-beam systems, we also ran a simulation with $w_1 = 1$ and $w_2 = 0$. In this case, $\varepsilon = 0.5$, the electrostatic instability develops likewise in the kinetic regime, and the Weibel mode is stable (Rafighi et al., 2017). The parameters of our simulations are summarized in Table 5.2, where for run 1 and run 2 the density ratio, plasma and beam temperatures, are the same but the weight of beam 1 and 2 and also the energy density ratios are varied.

Our PIC simulations were performed with EPOCH 2D (Arber et al., 2015). Additionally, we have introduced the algorithm of Zenitani (2015) to generate the relativistic Maxwellian distribution for the beams. The simulation plane was chosen to be the z-y plane with periodic boundary conditions. The pair beam propagates along the z-axis through the electron-proton plasma. The beam and plasma particles have the real mass ratio and fill the whole simulation box. The density ratio, $\alpha = 2 \times 10^{-4}$, is set with numerical weights. The simulation box is presented by $2048 \times 512$ cells, each one-fourth of the skin length in size, $\lambda_e = \frac{c}{\omega_{pe}} = 4\Delta_z$. Tests demonstrated a sufficient suppression of self-heating and statistical noise for our simulation setup that involves 400 computational particles per species and cell, a 6th-order field particle pusher, and a triangular-shaped cloud (TSC) shape function. The electrostatic instability grows in a very narrow band of wavenumbers. Therefore, to obtain proper results, the grid frequency should be high enough in order to resolve at least several points within the instability region (Shalaby et al., 2017). Figure 5.19 demonstrates the electric power spectrum for different skin lengths. It is well seen that sufficient resolution for grid frequencies of the narrow resonance at which the electrostatic instability operates is achieved for $\lambda_s = 3\Delta_x$.

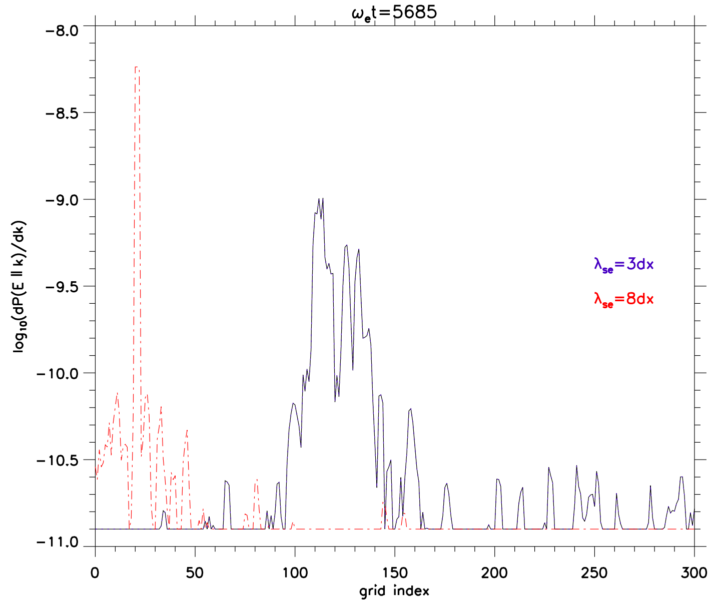

Fig. 5.19 Electric field power spectrum from test runs to check the resolution of grid frequencies for different skin lengths, all other parameters are fixed.

### 5.2.3 Simulations

Figure 5.20 compares the energy-density evolution of the electric and magnetic fields for runs 1 and 2. The linear growth rate of the electric field in the simulations agrees quite well with the theoretical calculations, providing $\omega_i = 10^{-3}\omega_p$ for run 1 and $\omega_i = 9\times10^{-4}\omega_p$ for run 2, at least during the initial phase. Already after $5000\omega_p^{-1}$ wave growth proceeds at a reduced pace. The numerical experiments also reproduce the slightly faster growth in run 1 compared to run 2. Although the second, high-energy beam provides additional high-energy particles, their effect on the growth rate is negligible. Thus, the growth rate is mainly determined by beam 1, and the slightly higher density ratio, $\alpha$, in run 1 leads to a marginally larger growth rate of the electrostatic instability.

Figures 5.21a and 5.21b illustrate the Fourier spectrum of the parallel electric field for runs 1 and 2, respectively, at the same time, $\omega_p t \approx 10152$. The dimensionless Fourier amplitude is defined as

$$\tilde{E}(k_{m,n}) \quad = \quad \frac{e}{m_e c\omega_p}\frac{1}{N_z N_y}\sum_{i=0}^{N_z-1}\sum_{j=0}^{N_y-1}\mathbf{e}_k \quad \cdot \quad \mathbf{E}(z_i,y_j)\,\exp\left(2\pi\imath\left[\frac{mi}{N_z}+\frac{nj}{N_y}\right]\right) \qquad , \quad (5.7)$$

where $m$ and $n$ are the index numbers of the wave-vector components in the $z$ and $y$ directions, respectively, and $\mathbf{e}_k$ is the unit wave vector. With this definition, the electrostatic field energy

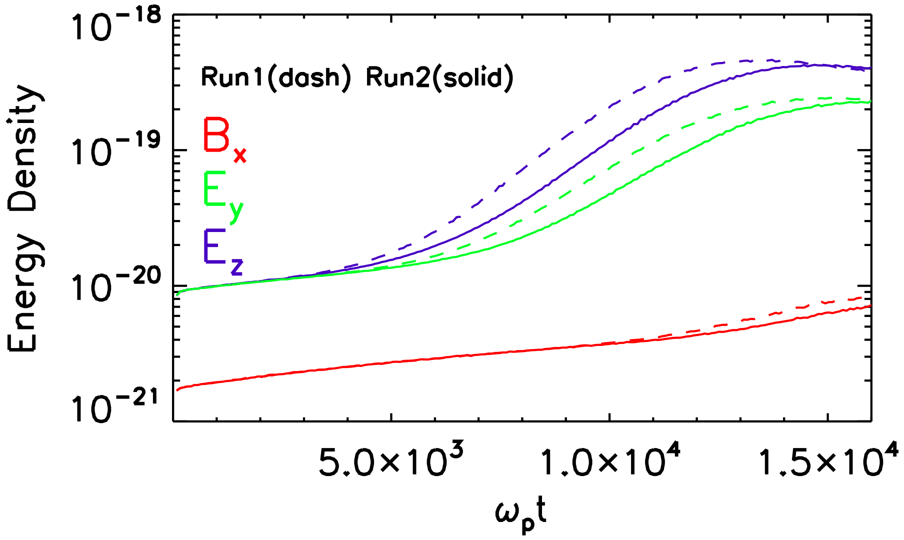

Fig. 5.20 Time evolution of the energy densities of electric and magnetic field, respectively, in SI units for run 1 (dashed lines) and run 2 (solid lines).

density, $U_{\text{ES}}$, is

$$U_{\text{ES}} = \frac{n_e m_e c^2}{2} \sum_{m=0}^{N_z-1} \sum_{n=0}^{N_y-1} |\tilde{E}(k_{m,n})|^2. \tag{5.8}$$

The peak growth of the electric field is observed as expected in the quasi-parallel direction to the beam (in agreement with the linear growth rate, figure 5.18), and the wave intensity in run 1 is also a bit higher than in run 2. In total, the wave energy density represents only a fraction $\lesssim 10^{-2}$ of the beam energy, and the beam does not suffer a significant loss of energy.

### Nonlinear instability saturation

We now demonstrate that the electrostatic instability in our simulations does not saturate on account of nonlinear Landau (NL) damping with rate (Breizman et al., 1972)

$$\omega_{NL} = \frac{3(2\pi)^{1/2}}{64} \int d^3k' \frac{W_k(\mathbf{k}')}{n_e m_e u_i} \frac{(\mathbf{k}\mathbf{k}')^2}{(kk')^2} \frac{k^2-k'^2}{|\mathbf{k}-\mathbf{k}'|} \exp\left[-\frac{1}{2}\left(\frac{3u_e^2}{2\omega_p u_i} \frac{k^2-k'^2}{|\mathbf{k}-\mathbf{k}'|}\right)^2\right], \tag{5.9}$$

where $u_{e,i} = (T_{\text{IGM}}/m_{e,i})^{1/2}$ denotes the thermal velocity of IGM electrons and ions, and $W_k(\mathbf{k})$ is the spectral energy density of the electric field. With the discrete Fourier amplitudes

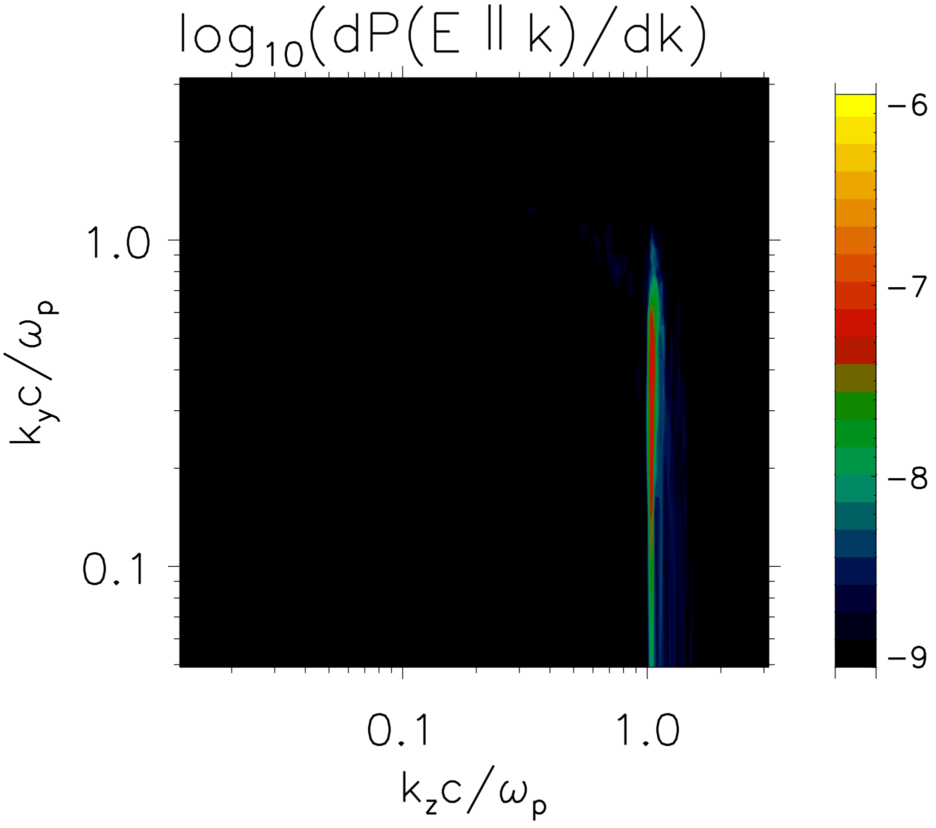

(a)

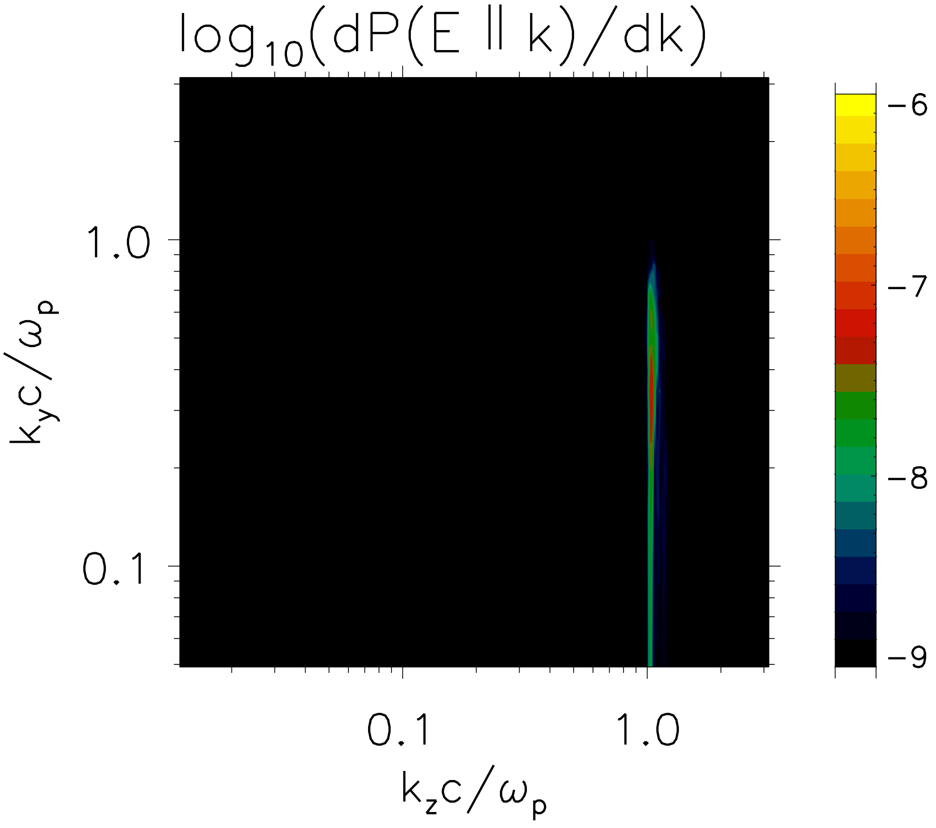

(b)

Fig. 5.21 (a) Two-dimensional Fourier spectrum of $\mathbf{E} \parallel \mathbf{k}$ (in units $(\omega_{p,e} c m_e / e)^2$) at $\omega_p t \approx 10152$ for run 1. (b) The same as (a), but for run 2.

calculated according to equation. 5.7 the nonlinear damping rate is

$$\omega_{NL} = \frac{3(2\pi)^{1/2}}{128}\frac{c^2}{u_i}\sum_{m=0}^{N_z-1}\sum_{n=0}^{N_y-1}|\tilde{E}(k_{m,n})|^2 \times \frac{(\mathbf{kk}')^2}{(kk')^2}\frac{k^2-k'^2}{|\mathbf{k}-\mathbf{k}'|}\exp\left[-\frac{1}{2}\left(\frac{3u_e^2}{2\omega_p u_i}\frac{k^2-k'^2}{|\mathbf{k}-\mathbf{k}'|}\right)^2\right]. \tag{5.10}$$

The range of wave vectors in which NL damping is efficient, is determined by the Gaussian “cut-off" in the integrand of equation 5.9. Therefore, we are interested in wave vectors for which the argument of the e-function is below unity,

$$\frac{|k^2-k'^2|}{|\mathbf{k}-\mathbf{k}'|} < \xi\frac{\omega_p}{c}, \tag{5.11}$$

where $\xi = (2\sqrt{2}/3)(m_e/m_i)^{1/2}(m_ec^2/T_{\mathrm{IGM}})^{1/2}$. In our simulations, $kT_{\mathrm{IGM}} = 2$ keV and hence $\xi \approx 0.22$. As the growth rate is sharply peaked near $k_z \simeq \pm\omega_p/c$, and we also have $P_k(-\mathbf{k}) = P_k(\mathbf{k})$ for the real-valued electric field, we find from equation 5.11 that the NL scattering is essentially always efficient for $k_z{}' \simeq -k_z$ and conditionally efficient for $k_z{}' \simeq k_z$, if $k_y \approx -k_y'$. Figures 5.21a and 5.21b indicate a high wave intensity in a stretch $0.2 \lesssim k_yc/\omega_p \lesssim 0.5$, which is well resolved with the $\Delta k_yc/\omega_p \simeq 0.05$ afforded by the simulation grid. The grid resolution in beam direction is chosen sufficiently high to resolve the resonance, $\Delta k_zc/\omega_p \simeq 0.0123$. Around $\omega_pt \approx 10{,}000$, we observe a high intensity extending over at least five grid points (in $k$), and the peak value is less than 50% of the total intensity at these five grid points. We conclude that the grid resolves the intensity at the resonance sufficiently well to permit NL damping in the simulation.

Using the simulation data, we obtain at the wave vector of peak growth $\omega_{NL} \approx 10^{-5}\omega_p$, which is much smaller than the maximum linear growth rate $\omega_i \approx 10^{-3}\omega_p$, and we conclude that NL damping is not responsible for the saturation of the electrostatic instability in our simulations.

Another crucial stabilization mechanism of the electrostatic mode is the modulation instability presented by Galeev et al. (1977); Papadopoulos (1975), which is same as the oscillating two-stream instability. Under such instability, high-frequency resonant waves produces cavities of electron density but enhanced electrostatic wave energy density. This leads to reduced wave-particle interaction, transferring wave energy from resonant phase speeds to non-resonant superluminal phase speeds and making the linear instabilities less efficient. Under the condition

$$\frac{U_{ES}}{n_e T_e} > \max\left[\frac{\Delta k}{k}(k\lambda_D)^2,\ \frac{m_e}{m_p}\right] \tag{5.12}$$

the growth rate of the modulation instability can be found as (Papadopoulos, 1975)

$$\omega_M = \omega_p \left(\frac{m_e}{m_p}\frac{U_{ES}}{n_e T_e}\right)^{1/2} . \tag{5.13}$$

Here, $\Delta k$ is the characteristic width of the electric field spectrum. For runs 1 and 2 (see figure 5.18), the saturation energy of the electric field is $U_{ES} \approx 10^{-19}$ J/m$^3$. The IGM plasma density in the simulations is $n_e = 0.25$ m$^{-3}$ which yields $U_{ES}/(n_e T_e) \approx 5 \cdot 10^{-3}$. Since the electric field energy is localized near the wave number $k \approx \omega_p/c$, $(k\lambda_D)^2 \approx 4 \cdot 10^{-3}$, and condition (5.12) is fulfilled for both simulation runs. The damping rate is $\omega_M \approx 1.6 \cdot 10^{-3}\omega_p > \omega_i$, and so it is the modulation instability that stabilizes the electrostatic mode in our simulations.

Having established that the electrostatic instability has a short growth time compared to other timescales of interactions of the pair beam, we now have to estimate the saturation level and energy transfer rate. In our PIC simulations, the modulation instability saturates the waves at an energy density that corresponds to 1% of the energy density of the beam. Saturation does not imply a vanishing energy transfer, and in fact the beam interacts with the wavefield as long as it not cooled by inverse-Compton scattering or deflected out of resonance by the ambient magnetic field. Following the beam's propagation through the saturated wave field for the mean-free path for Compton scattering, $\lambda_{\mathrm{IC}}$, is impossible with PIC simulations, and so we resort to analytical estimates.

Saturation is defined as the statistical balance between the driving, cascading, and damping of waves. Writing the driving rate in the Fourier power as $2\omega_i\,|P_k|^2$, one would use Parseval's theorem to calculate the energy transfer rate per volume $V$, accounting for equipartition between the kinetic energy and electrostatic energy in the electrostatic mode.

$$\frac{dU_{\mathrm{beam}}}{dt} = -2\frac{dU_{\mathrm{ES}}}{dt} = -\frac{2\,\varepsilon_0}{V}\int d\mathbf{k}\;|P_k|^2\,\omega_i\;. \tag{5.14}$$

The inverse loss time scale for beam energy then is

$$\tau_{\mathrm{loss}}^{-1} = \left|\frac{d\ln U_{\mathrm{beam}}}{dt}\right| \simeq \frac{2\,\varepsilon_0}{V\,U_{\mathrm{beam}}}\int d\mathbf{k}\;|P_k|^2\,\omega_i\;. \tag{5.15}$$

Written for the 2D discrete Fourier power available from our simulation, equation (5.14) assumes the form

$$\frac{dU_{\text{beam}}}{dt} = -2n_e m_e c^2 \sum_{m=0}^{N_z-1} \sum_{n=0}^{N_y-1} |\tilde{E}(k_{m,n})|^2 \, \omega_i(m,n) \; , \tag{5.16}$$

and the inverse loss time is

$$\tau_{\text{loss}}^{-1} \simeq \frac{2n_e m_e c^2}{U_{\text{beam}}} \sum_{m=0}^{N_z-1} \sum_{n=0}^{N_y-1} |\tilde{E}(k_{m,n})|^2 \, \omega_i(m,n) \; . \tag{5.17}$$

The symmetry in $P_k$ permits performing the sum over only one quadrant of $\mathbf{k}$ space and then applying a factor of 4 plus another small factor that accounts for extending the wave spectrum from the 2D simulation behaviour to the 3D real-world geometry. The energy transfer rate is hence estimated by folding the wave power spectrum close to the saturation level with the linear growth rate. This is a conservative estimate, because already at moderately nonlinear amplitudes the growth rate is observed to fall below 70% of its initial value.

At time $t \approx 10^4/\omega_p$, our numerical results provide $dU_{\text{beam}}/dt \approx 6 \cdot 10^{-21}$ J/(m$^3$·s) and $\tau_{\text{loss}} \approx 5 \cdot 10^5/\omega_p$. The wave intensity remains near the peak value for a time period of $\lesssim 5 \cdot 10^3/\omega_p$, which is much shorter than the estimated loss time. The estimated energy loss is below the percent level, and indeed only a tiny beam energy loss can be observed in the simulations. Numerically, we would have obtained the same result if we had replaced $\omega_i(m,n)$ in equation (5.14) with half of its peak value,

$$\frac{dU_{\text{beam}}}{dt} \simeq -2\,U_{\text{ES}}\,\omega_{i,\max} \; . \tag{5.18}$$

We shall use this formula when estimating the loss rate of realistic beams.

### Nonlinear instability saturation for realistic Blazar-induced Pair Beams

We shall now discuss the saturation process and level for realistic beam parameters. We begin with the modulation instability as the damping process that we found to dominate in our simulation. Let us introduce additional scaling: $\gamma = 10^6\gamma_6$, $T_{\text{IGM}} = 10^4\,T_4$ K. Then, the peak linear growth rate of the electrostatic mode can be written as

$$\omega_{i,\max} \simeq \left(1.88 \cdot 10^{-7}\right) \omega_p \frac{n_{b20}}{n_{e7}} = 5.64 \cdot 10^{-9} \omega_p \; , \tag{5.19}$$

where, in the last expression, we inserted $n_{b20} = 0.03$ as for the pair distribution shown in figure B.2. Note that the estimate (5.19) is by a factor 10 higher than that in Miniati and

Elyiv (2013), who additionally considered IC-cooled pair beams. We shall now estimate the wave intensity for which the modulation instability is strong enough to halt further wave growth. equations (5.12)-(5.13) read

$$\delta = \frac{U_{\mathrm{ES}}}{n_b\,\gamma_b\,m_e c^2} > \max\left[4\cdot 10^{-5}\,\frac{\Delta k}{k}\,\frac{n_{e7}\,T_4^2}{n_{b20}\,\gamma_6},\ 0.1\,\frac{n_{e7}T_4}{n_{b20}\,\gamma_6}\right], \tag{5.20}$$

$$\omega_M/\omega_p = 5.2\cdot 10^{-3}\sqrt{\frac{\delta\,n_{b20}\,\gamma_6}{n_{e7}\,T_4}}. \tag{5.21}$$

Setting $\omega_M = \omega_{i,\mathrm{max}}$ would require $\delta \approx 10^{-11}$, for which condition (5.20) is not fulfilled, and the result of Papadopoulos (1975) does not apply. Instead, since $\omega_M \ll k v_{T,i}$, where $v_{T,i} = \sqrt{T_{\mathrm{IGM}}/m_i}$, we should use the growth rate and threshold condition of the modulation instability, equations (10)-(11) derived by Baikov (1977). We write them, respectively, in the form

$$\omega_M = -\Gamma_L + |\Delta|\left(-1 - 0.25\frac{U_{ES}}{n_e T_e}\frac{\omega_p}{\Delta}\right)^{1/2}, \tag{5.22}$$

$$\delta_M = \frac{U_{\mathrm{ES}}}{n_b\,\gamma_b\,m_e c^2} > \delta_{\mathrm{min}} = \frac{4\,n_e T_e}{n_b\,\gamma_b\,m_e c^2}\,\frac{\Gamma_L^2 + \Delta^2}{|\Delta|\,\omega_p} \tag{5.23}$$

Here, $\Gamma_L$ is the damping rate due to particle collisions and linear Landau damping, whereas $\Delta$ is the mismatch between the Langmuir frequency and the frequency of the unstable oscillations. In the cold-beam limit, it is easy to find (Baikov, 1977):

$$\Delta \approx -\frac{\omega_p}{2^{4/3}}\left(\frac{n_b}{n_e\gamma}\right)^{1/3}\left(\sin^2\theta + \frac{\cos^2\theta}{\gamma^2}\right)^{1/3}, \tag{5.24}$$

where $\theta$ is the angle between the wave vector and the beam. For the realistic beam, the strongest mode develops at the angle $\theta \approx 0.33$ rad (see figure 3.5b), yielding, for typical parameters,

$$\Delta \approx -8.8\cdot 10^{-8}\,\omega_p\left(\frac{n_{b20}}{n_{e7}\gamma_6}\right)^{1/3}. \tag{5.25}$$

Since the collision frequency $\nu_{ei} \approx 10^{-13}\omega_p$, we have $\Gamma_L \ll \Delta$, and the threshold condition for the modulation instability (5.23) finally becomes

$$\delta_{\mathrm{min}} \simeq 6\cdot 10^{-6}\,T_4\,\gamma_6^{-4/3}\left(\frac{n_{e7}}{n_{b20}}\right)^{2/3} \simeq 10^{-5}, \tag{5.26}$$

where again the last expression applies for the parameters of the pair distribution shown in figure B.2, $n_{b20} = 0.03$ and $\gamma_6 = 4$. Now we solve equation 5.22 for $\omega_M = \omega_{i,\max}$ and find

$$\delta_M \simeq \delta_{\min} \left[ 1 + 4.7\,\gamma_6^{2/3} \left( \frac{n_{b20}}{n_{e7}} \right)^{4/3} \right] \simeq 10^{-5} \,. \tag{5.27}$$

To be noted from this expression is that while formally $\delta_M$ is larger than the threshold value, it is numerically very similar for the parameters of realistic pair beams.

Turning to NL damping, it can easily be seen that the Gaussian in equation (5.9) essentially always returns to unity, since the cutoff scale $\xi \approx 14$ (see equation. (5.11)). Most electrostatic energy grows near the resonance wave number $\omega_p/c$ (see figure 3.5b), and so we can analytically estimate the second and third factors of the integrand in equation (5.9) and find them approximately equal to $\mathrm{k} - \mathrm{k}'$. Writing $\Delta k = \mathrm{k} - \mathrm{k}' \approx 0.1\,\omega_p/c$, we obtain

$$\begin{aligned} \omega_{\mathrm{NL}} &\approx 10^{-3}\,\omega_p \left( \frac{\Delta k\; c}{\omega_p} \right) \frac{\delta\, n_{b20}\,\gamma_6}{n_{e7}\,T_4^{1/2}} \\ &\approx 10^{-4}\,\omega_p \frac{\delta\, n_{b20}\,\gamma_6}{n_{e7}\,T_4^{1/2}}. \end{aligned} \tag{5.28}$$

The estimate for $\Delta k$ is very rough, but our result only weakly depends on this parameter, as will be seen below. For the pair distribution shown in figure B.2, $n_{b20} = 0.03$, $\gamma_6 = 4$, setting $\omega_{\mathrm{NL}} = \omega_{i,\max}$ leads to

$$\delta_{NL} \approx 5 \cdot 10^{-4}. \tag{5.29}$$

This corresponds to a higher wave intensity as that found for the modulation instability (see equation 5.27), and we conclude that the modulation instability provides a stronger limitation on the beam intensity than does NL damping. Note that Schlickeiser et al. (2012b) and Miniati and Elyiv (2013) used equation (5.12) as the threshold condition for the modulation instability, which we show not to be applicable for the realistic parameters.

Using our result for $\delta_M$, where we adopted $n_b = n_{b,20} 10^{-20}\ \mathrm{cm}^{-3}$ and $n_e = n_{e,7} 10^{-7}\ \mathrm{cm}^{-3}$, we can estimate the relaxation time of the blazar-induced pair beam using equation (5.18),

$$\begin{aligned} \tau_{\mathrm{loss}}^{-1} &\simeq 2\,\delta_M\,\omega_{i,\max} \\ &\simeq (6 \cdot 10^{-11}\ \mathrm{s}^{-1})\,T_4\,\gamma_6^{-4/3} \left( \frac{n_{b20}}{n_{e7}} \right)^{1/3} \,. \end{aligned} \tag{5.30}$$

This loss rate is to be compared with that for inverse-Compton scattering at redshift $z$,

$$\tau_{\mathrm{IC}}^{-1} \simeq (1.3 \cdot 10^{-14}\ \mathrm{s}^{-1})\, \gamma_6\, (1+z)^4 \,. \tag{5.31}$$

For the ratio of timescales, we find with the realistic parameters $n_{b20} = 0.03$ and $\gamma_6 = 4$, and introducing the redshift scaling for the IGM density,

$$\begin{aligned} \frac{\tau_{\mathrm{loss}}}{\tau_{\mathrm{IC}}} &\simeq 2.2 \cdot 10^{-4}\, \frac{\gamma_6^{7/3}}{T_4} \left(\frac{n_{e7}}{n_{b20}}\right)^{1/3} (1+z)^5 \\ &\simeq 0.02\, (1+z)^5 \,, \end{aligned} \tag{5.32}$$

indicating that for redshift $z \lesssim 1.2$ plasma instabilities drain the energy of the pair beam faster than comptonization of the microwave background would. This estimate is very weakly dependent on the density of the pair beam and that of the IGM, and so the distance from the AGN is of moderate importance, as is the TeV-band luminosity. It does strongly vary with the choice of pair Lorentz factors. With our nominal $\gamma_6 = 4$, the pairs would upscatter the microwave background to about 10 GeV in gamma-ray energy, i.e. into the energy range where the *Fermi*-LAT has the optimal sensitivity for the cascade signal. A number of comments are in order:

1. In our simulations, the peak growth rate was somewhat reduced during the nonlinear phase, which would imply a longer loss time if TeV-scale pair beams behaved in the same way.

2. Any other cascading or loss mechanism beyond the modulation and the nonlinear Landau damping considered here would also increase the loss time, because it would reduce the saturation amplitude, $\delta_M$.

3. Substantial uncertainty derives from the exact form of the pair spectrum, and Miniati and Elyiv (2013) find a peak growth rate around 10% of our result only by allowing for efficient cooling, which would translate to a 10 times longer loss time. Typically, the exact primary gamma-ray spectrum is not known, in particular, neither the spectral index nor the cutoff energy, and so it is not possible to completely predict the pair spectrum.

4. We calculate the bulk energy loss of the pair beam without consideration of its energy dependence. It is possible that the energy loss primarily affects the pairs that are also instrumental in driving the electrostatic mode, while leaving unaffected those pairs that are most efficient in producing the gamma-ray cascade signal in the GeV band.

All of the above suggests that the result (5.32) should be seen as a lower limit with significant uncertainty. Thus, we conclude that the blazar-induced pair beam at moderate redshift $z \approx 0.2$ will lose its energy with similar efficiency to inverse-Compton scattering and to the interaction with plasma waves.

### 5.2.4 Summary

To study the non-linear beam evolution, we used PIC simulations. In contrast to earlier studies Kempf et al. (2016); Rafighi et al. (2017); Sironi and Giannios (2014), we now considered a non-monoenergetic beam via a superposed relativistic Maxwellians of two beams, albeit at small beam Lorentz factor following Rafighi et al. (2017). We find that the beam energy losses about 1% of its initial energy and the saturation level of the electrostatic waves is determined by the modulation instability. However the beam relaxation timescale $\approx 5.6 \cdot 10^5/\omega_p$ based on analytical analysis is much longer than the time covered by our simulation ($\approx 1.5 \cdot 10^4/\omega_p$). A more detailed presentation of the summary and results is presented in Chapter 6.

# Chapter 6

# Summary and conclusions

In virtue of all the advancements in science and technology, human mind is facing more and more complicated issues to solve. Astrophysics is no exception to that, providing astrophysicists tools to overcome the new challenges.

New Cherenkov telescopes such as HESS, VERITAS and Fermi satellite, have discovered many blazars as sources of very high-energy gamma rays ($E \geq 100$ GeV) (de Naurois (2015)). Interacting with the extragalactic background light (EBL), these very energetic photons create electron-positron pairs that in turn produce an inverse-Compton cascade in the GeV band. Observations with Fermi-LAT indicate (Neronov and Vovk (2010)) that the GeV gamma-ray flux from some blazars is lower than that predicted from the full electromagnetic cascade (Neronov and Semikoz (2009)). The works of Neronov and Vovk (2010); Taylor et al. (2011) suggests a possible explanation is deflection in intergalactic magnetic field of strength $B \geq 3 \times 10^{-16}$ Gauss.

Furthermore, an alternative theory involves beam dissipation by plasma instabilities (Breizman, 1990; Breizman and Riutov, 1974; Bret, 2006; Bret et al., 2004, 2005, 2010; Godfrey et al., 1975; Lominadze and Mikhailovskii, 1979). Several analytical studies have covered the electrostatic instability of blazar-induced pair beams. Broderick et al. (2012) and Schlickeiser et al. (2012b) considered a monoenergetic beam with no momentum spread, for which the electrostatic mode reaches its maximum growth rate at a wave vector quasiperpendicular to the beam direction. Miniati and Elyiv (2013) analysed the electrostatic mode for a steady-state pair distribution given by the balance between the pair production and inverse-Compton losses. They found the maximum growth rate in a direction almost parallel to the beam, in contrast to the case of a cold beam (Schlickeiser et al., 2012b).

In this work, we established parameter regimes for PIC simulations that permit extrapolation to the very low density and monoenergetic pair beams relevant to the scenarios by Schlickeiser et al. (2012b) and Miniati and Elyiv (2013). We also investigated the impact of non-monoenergetic beam distribution functions. We have presented results of both our linear analysis in Chapter 3 and our PIC simulations in Chapter 5. In our simulations we also verify the results of Sironi and Giannios (2014) and Kempf et al. (2016) where they considered only some of the requirements on the beam-plasma system.

In sections 3.4 and 5.1, based on our first publication related to this thesis (Rafighi et al., 2017), we used a simple analytical model and demonstrated that the Weibel mode is actually stable for realistic parameters which adds a third criterion for the pair beams in addition to the ones noticed by earlier PIC simulations. In contrast to the simulations by Sironi and Giannios (2014) and Kempf et al. (2016), we performed a simulation (run 1) (see 5.1.4), for which all of them are taken into account. Then, we have compared this case with three other simulations, for which some criteria were violated. The results of run 1 indicate that the pair beam does not experience any significant modification within the simulation time, but the beam can relaxate on much larger time scales. The electrostatic growth rate turns out to be relatively small, and non-linear effects stabilize the beam very efficiently.

In sections 3.5 and 5.2, based on our second publication related to this thesis (Vafin et al., 2018), we also revisited the growth rate of the electrostatic instability under conditions relevant for a realistic blazar-induced pair beams propagating through the IGM. Our goal was to clarify somewhat contradicting statements by Schlickeiser et al. (2013) and Miniati and Elyiv (2013) and to establish the energy loss rate of pair beams for driving the waves.

We calculated the energy distribution function of blazar-induced pairs without modification by IC scattering, since we intended to study the effect of the electrostatic instability. We assumed a power-law spectrum $\propto E^{-1.8}$ for the blazar emission and used the models of Finke et al. (2010) and Fabian and Barcons (1992) to describe the EBL spectrum. We found a broad pair spectrum ($10^1 < \gamma < 10^8$) similar to that in Miniati and Elyiv (2013). This spectrum contains a pronounced low-energy part arising from interaction with the X-ray background radiation that is missing in the treatment of Schlickeiser et al. (2012a,b, 2013). Then, we used the newly evaluated pair distribution to study the growth rate of the electrostatic instability and did not find any significant effect of low-energy pairs with $\gamma < 10^4$, lending support to the results of Schlickeiser et al. (2012b, 2013).

We investigated the growth rate of the instability for arbitrary wave vectors with and without angular spread. If the beam has no angular spread, then the growth rate reaches its maximum at wave vectors perpendicular to the beam. However, for a realistic finite angular spread, the growth rate is the largest at wave vectors quasiparallel to the beam direction, and the maximum growth rate is reduced. Both findings are in agreement with Miniati and Elyiv (2013). We note that the growth rate at oblique wave vectors is only by a factor of 2-4 smaller than the maximum growth rate, which can be crucial for the non-linear evolution of the beam.

We also found that the maximum growth rate for a finite angular spread is by more than a factor of 10 larger than the peak growth rate of the strictly parallel electrostatic mode studied by Schlickeiser et al. (2013).

Miniati and Elyiv (2013) took into account the IC cooling of all beam electrons and positrons, not only those with $\gamma > 10^7$. From their results, it follows that the IC scattering reduces the maximum growth rate by about an order of magnitude. As we investigate the viability of the instability providing the dominant energy loss, we need to consider an uncooled beam, and hence the larger linear growth rate. The strong dependence of the growth rate on the shape of the pair spectrum suggests that there may also be substantial variation in the growth rate arising from the shape of the primary gamma-ray spectrum produced by the blazar, in particular, the spectral index and the cutoff energy.

To study the nonlinear beam evolution, we used PIC simulations. In contrast to earlier studies (Kempf et al., 2016; Rafighi et al., 2017; Sironi and Giannios, 2014), we now considered a non-monoenergetic beam. We find that the beam energy losses remain at a very low level (about 1% of its initial energy). Furthermore, the saturation level of the electrostatic waves is determined by the modulation instability. However the beam relaxation timescale $\approx 5.6 \cdot 10^5/\omega_p$ based on analytical analysis is much longer than the time covered by our simulation ($\approx 1.5 \cdot 10^4/\omega_p$).

Our analytical analysis then permits extrapolation to realistic pair beams. We determine the linear growth rate of the electrostatic instability and find that also in this case the modulation instability is a faster saturation process than is nonlinear Landau damping. Miniati and Elyiv (2013) arrived at the opposite conclusion, but used a less accurate threshold condition of the modulation instability. Balance of growth and damping determines that saturation level, from which we analytically estimate that the energy-loss time scale for beam instabilities is slightly smaller than that for comptonization of the microwave background, so that the electrostatic beam stability could at least reduce the intensity of the gamma-ray cascade emission in the GeV band. The uncertainties in the estimate are large though, and there is a significant dependence on redshift.

If the effective loss length is indeed slightly reduced by beam instabilities, the flux of the cascade signal is correspondingly smaller. Any magnetic deflection of the beam would then have to be accomplished over this smaller pathlength and would hence require a stronger magnetic field. An interesting possibility is that the intergalactic magnetic field increases the transverse momentum spread and hence reduces the growth rate of the electrostatic instability. A strictly homogeneous magnetic field would also diverge the electron beam and the positron beam, which might trigger other plasma instabilities.

Ultimately, the magnetic field deflection is still the main candidate to explain the lack of GeV-band cascade signal from blazars. However, the non-linear relaxation of the realistic blazar-induced beams is subject for future investigations, as it is not fully understood yet. Indeed it is an open and exciting subject of research for the junior and senior researchers in this field.

# References

A. A. Abdo. The First Catalog of Active Galactic Nuclei Detected by the Fermi Large Area Telescope. *Astrophys. J.*, 715:429–457, 2010. doi: 10.1088/0004-637X/715/1/429.

A A. Abdo et al. Bright AGN Source List from the First Three Months of the Fermi Large Area Telescope All-Sky Survey. *Astrophys. J.*, 700:597–622, 2009. doi: 10.1088/0004-637X/700/1/597.

A. A. Abdo et al. Spectral Properties of Bright Fermi-Detected Blazars in the Gamma-Ray Band. *The Astrophysical Journal*, 710(2):1271, 2010. URL http://stacks.iop.org/0004-637X/710/i=2/a=1271.

F. A. Aharonian, P. S. Coppi, and H. J. Voelk. Very high energy gamma rays from active galactic nuclei: Cascading on the cosmic background radiation fields and the formation of pair halos. , 423:L5–L8, March 1994. doi: 10.1086/187222.

F.A. Aharonian. TeV gamma rays from {BL} lac objects due to synchrotron radiation of extremely high energy protons. *New Astronomy*, 5(7):377 – 395, 2000. ISSN 1384-1076. doi: https://doi.org/10.1016/S1384-1076(00)00039-7. URL http://www.sciencedirect.com/science/article/pii/S1384107600000397.

T D Arber, K Bennett, C S Brady, A Lawrence-Douglas, M G Ramsay, N J Sircombe, P Gillies, R G Evans, H Schmitz, A R Bell, and C P Ridgers. Contemporary particle-in-cell approach to laser-plasma modelling. *Plasma Physics and Controlled Fusion*, 57(11):113001, 2015. URL http://stacks.iop.org/0741-3335/57/i=11/a=113001.

I. S. Baikov. Parametric instabilities produced by a relativistic electron beam in a plasma. *Physica B+C*, 92:267–280, October 1977. doi: 10.1016/0378-4363(77)90029-8.

L. Bassani and A. J. Dean. Extragalactic $\gamma$-ray astronomy. *Space Science Reviews*, 35(4):367–398, Aug 1983. ISSN 1572-9672. doi: 10.1007/BF00169232. URL https://doi.org/10.1007/BF00169232.

Volker Beckmann and Chris R. Shrader. The AGN phenomenon: open issues. *PoS*, INTEGRAL2012:069, 2013.

CK Birdsall and AB Langdon. *Plasma physics via computer simulation*. Series in plasma physics and fluid dynamics. CRC Press, Hoboken, NJ, 2004. URL http://cds.cern.ch/record/2019089.

Jay P Boris. Relativistic plasma simulation-optimization of a hybrid code. In *Proc. Fourth Conf. Num. Sim. Plasmas, Naval Res. Lab, Wash. DC*, pages 3–67, 1970.

G. E. P. Box and Mervin E. Muller. A note on the generation of random normal deviates. *Ann. Math. Statist.*, 29(2):610–611, 06 1958. doi: 10.1214/aoms/1177706645. URL https://doi.org/10.1214/aoms/1177706645.

B. N. Breizman. *RvPP*, 15:61, 1990.

B. N. Breizman and D. D. Riutov. Powerful relativistic electron beams in a plasma and in a vacuum /theory/. *Nuclear Fusion*, 14:873–907, December 1974.

B. N. Breizman, D. D. Ryutov, and P. Z. Chebotaev. Nonlinear Effects in the Interaction Between an Ultrarelativistic Electron Beam and a Plasma. *JETP*, 35:741, 1972.

A. Bret. Oblique electromagnetic instabilities for an ultra relativistic electron beam passing through a plasma. *EPL (Europhysics Letters)*, 74(6):1027, 2006. URL http://stacks.iop.org/0295-5075/74/i=6/a=1027.

A. Bret. CfA Plasma Talks. *ArXiv e-prints*, May 2012.

A. Bret, M.-C. Firpo, and C. Deutsch. Collective electromagnetic modes for beam-plasma interaction in the whole *k* space. *Phys. Rev. E*, 70:046401, Oct 2004. doi: 10.1103/PhysRevE.70.046401. URL https://link.aps.org/doi/10.1103/PhysRevE.70.046401.

A. Bret, M.-C. Firpo, and C. Deutsch. Electromagnetic instabilities for relativistic beam-plasma interaction in whole *k* space: Nonrelativistic beam and plasma temperature effects. *Phys. Rev. E*, 72:016403, Jul 2005. doi: 10.1103/PhysRevE.72.016403. URL https://link.aps.org/doi/10.1103/PhysRevE.72.016403.

A. Bret, L. Gremillet, and M. E. Dieckmann. Multidimensional electron beam-plasma instabilities in the relativistic regime. *Physics of Plasmas*, 17(12):120501, 2010. doi: 10.1063/1.3514586. URL http://dx.doi.org/10.1063/1.3514586.

Avery E. Broderick, Philip Chang, and Christoph Pfrommer. The Cosmological Impact of Luminous TeV Blazars. I. Implications of Plasma Instabilities for the Intergalactic Magnetic Field and Extragalactic Gamma-Ray Background. *The Astrophysical Journal*, 752(1):22, 2012. URL http://stacks.iop.org/0004-637X/752/i=1/a=22.

O. Buneman. Dissipation of Currents in Ionized Media. *Physical Review*, 115:503–517, August 1959. doi: 10.1103/PhysRev.115.503.

O Buneman. TRISTAN: The 3-D Electromagnetic Particle Code. In *Computer Space Plasma Physics: Simulations Techniques and Software*. 1993.

M. Böttcher, A. Reimer, K. Sweeney, and A. Prakash. Leptonic and Hadronic Modeling of Fermi-detected Blazars. *The Astrophysical Journal*, 768(1):54, 2013. URL http://stacks.iop.org/0004-637X/768/i=1/a=54.

F. Califano, R. Prandi, F. Pegoraro, and S. V. Bulanov. Nonlinear filamentation instability driven by an inhomogeneous current in a collisionless plasma. *Phys. Rev. E*, 58:7837–7845, Dec 1998. doi: 10.1103/PhysRevE.58.7837. URL https://link.aps.org/doi/10.1103/PhysRevE.58.7837.

Philip Chang, Avery E. Broderick, and Christoph Pfrommer. The Cosmological Impact of Luminous TeV Blazars. II. Rewriting the Thermal History of the Intergalactic Medium. *The Astrophysical Journal*, 752(1):23, 2012. URL http://stacks.iop.org/0004-637X/752/i=1/a=23.

Fermi/LAT Collaboration. The Second Catalog of Active Galactic Nuclei Detected by the Fermi Large Area Telescope. *Astrophys. J.*, 743:171, 2011. doi: 10.1088/0004-637X/743/2/171.

Fermi/LAT Collaboration. The Third Catalog of Active Galactic Nuclei Detected by the Fermi Large Area Telescope. *The Astrophysical Journal*, 810(1):14, 2015a. URL http://stacks.iop.org/0004-637X/810/i=1/a=14.

Fermi/LAT Collaboration. The Third Catalog of Active Galactic Nuclei Detected by the Fermi Large Area Telescope. *Astrophys. J.*, 810(1):14, 2015b. doi: 10.1088/0004-637X/810/1/14.

Asantha Cooray. Extragalactic background light measurements and applications. *Royal Society Open Science*, 3(3), 2016. doi: 10.1098/rsos.150555. URL http://rsos.royalsocietypublishing.org/content/3/3/150555.

L. A. Cottrill, A. B. Langdon, B. F. Lasinski, S. M. Lund, K. Molvig, M. Tabak, R. P. J. Town, and E. A. Williams. Kinetic and collisional effects on the linear evolution of fast ignition relevant beam instabilities. *Physics of Plasmas*, 15(8):082108, 2008. doi: 10.1063/1.2953816. URL http://dx.doi.org/10.1063/1.2953816.

P. A. Davidson. *An Introduction to Magnetohydrodynamics*. Cambridge University Press, March 2001.

John M. Dawson. Particle simulation of plasmas. *Rev. Mod. Phys.*, 55:403–447, Apr 1983. doi: 10.1103/RevModPhys.55.403. URL https://link.aps.org/doi/10.1103/RevModPhys.55.403.

M. de Naurois. The Very High Energy Sky from 20 GeV to Hundreds of TeV - Selected Highlights. In A. S. Borisov, V. G. Denisova, Z. M. Guseva, E. A. Kanevskaya, M. G. Kogan, A. E. Morozov, V. S. Puchkov, S. E. Pyatovsky, G. P. Shoziyoev, M. D. Smirnova, A. V. Vargasov, V. I. Galkin, S. I. Nazarov, and R. A. Mukhamedshin, editors, *34th International Cosmic Ray Conference (ICRC2015)*, volume 34 of *International Cosmic Ray Conference*, page 21, July 2015.

Mathieu de Naurois and Daniel Mazin. Ground-based detectors in very-high-energy gamma-ray astronomy. *Comptes Rendus Physique*, 16(6):610 – 627, 2015. ISSN 1631-0705. doi: https://doi.org/10.1016/j.crhy.2015.08.011. URL http://www.sciencedirect.com/science/article/pii/S1631070515001462. Gamma-ray astronomy / Astronomie des rayons gamma.

Charles D. Dermer, Massimo Cavadini, Soebur Razzaque, Justin D. Finke, James Chiang, and Benoit Lott. Time Delay of Cascade Radiation for TeV Blazars and the Measurement of the Intergalactic Magnetic Field. *The Astrophysical Journal Letters*, 733(2):L21, 2011. URL http://stacks.iop.org/2041-8205/733/i=2/a=L21.

Charles Dennison Dermer and Berrie Giebels. Active galactic nuclei at gamma-ray energies. *Comptes Rendus Physique*, 17(6):594 – 616, 2016. ISSN 1631-0705. doi: https://doi.org/10.1016/j.crhy.2016.04.004. URL http://www.sciencedirect.com/science/article/pii/S163107051630024X. Gamma-ray astronomy / Astronomie des rayons gamma - Volume 2.

M. E. Dieckmann, J. T. Frederiksen, A. Bret, and P. K. Shukla. Evolution of the fastest-growing relativistic mixed mode instability driven by a tenuous plasma beam in one and two dimensions. *Physics of Plasmas*, 13(11):112110, 2006. doi: 10.1063/1.2390687. URL https://doi.org/10.1063/1.2390687.

Eli Dwek and Frank Krennrich. The extragalactic background light and the gamma-ray opacity of the universe. *Astroparticle Physics*, 43(Supplement C):112 – 133, 2013. ISSN 0927-6505. doi: https://doi.org/10.1016/j.astropartphys.2012.09.003. URL http://www.sciencedirect.com/science/article/pii/S0927650512001752. Seeing the High-Energy Universe with the Cherenkov Telescope Array - The Science Explored with the CTA.

A. Elyiv, A. Neronov, and D. V. Semikoz. Gamma-ray induced cascades and magnetic fields in the intergalactic medium. *Phys. Rev. D*, 80:023010, Jul 2009. doi: 10.1103/PhysRevD.80.023010. URL https://link.aps.org/doi/10.1103/PhysRevD.80.023010.

T.Zh. Esirkepov. Exact charge conservation scheme for Particle-in-Cell simulation with an arbitrary form-factor. *Computer Physics Communications*, 135(2):144 – 153, 2001. ISSN 0010-4655. doi: https://doi.org/10.1016/S0010-4655(00)00228-9. URL http://www.sciencedirect.com/science/article/pii/S0010465500002289.

V. F. Hess. Über Beobachtungen der durchdringenden Strahlung bei sieben Freiballonfahrten. *Physikalische Zeitschrift*, 13:1084–1091, November 1912.

A. C. Fabian and X. Barcons. The Origin of the X-Ray Background. *Annual Review of Astronomy and Astrophysics*, 30(1):429–456, 1992. doi: 10.1146/annurev.aa.30.090192.002241. URL https://doi.org/10.1146/annurev.aa.30.090192.002241.

K. Fang. Contribution to individual blazar spectrum from the cascade of very-high energy gamma rays. Masters thesis, Graduate Theses and Dissertations, Paper 11461, Iowa State University, 2010.

C. E. Fichtel, D. L. Bertsch, J. Chiang, B. L. Dingus, J. A. Esposito, J. M. Fierro, R. C. Hartman, S. D. Hunter, G. Kanbach, D. A. Kniffen, P. W. Kwok, Y. C. Lin, J. R. Mattox, H. A. Mayer-Hasselwander, L. McDonald, P. F. Michelson, C. von Montigny, P. L. Nolan, K. Pinkau, H.-D. Radecke, H. Rothermel, P. Sreekumar, M. Sommer, E. J. Schneid, D. J. Thompson, and T. Willis. The first energetic gamma-ray experiment telescope (EGRET) source catalog. , 94:551–581, October 1994. doi: 10.1086/192082.

Justin D. Finke, Soebur Razzaque, and Charles D. Dermer. Modeling the Extragalactic Background Light from Stars and Dust. *The Astrophysical Journal*, 712(1):238, 2010. URL http://stacks.iop.org/0004-637X/712/i=1/a=238.

F Fiuza, M Marti, R A Fonseca, L O Silva, J Tonge, J May, and W B Mori. Efficient modeling of laser–plasma interactions in high energy density scenarios. *Plasma Physics and Controlled Fusion*, 53(7):074004, 2011. URL http://stacks.iop.org/0741-3335/53/i=7/a=074004.

D. J. Fixsen. The Temperature of the Cosmic Microwave Background. *The Astrophysical Journal*, 707(2):916, 2009. URL http://stacks.iop.org/0004-637X/707/i=2/a=916.

Steven R. Furlanetto, S. Peng Oh, and Frank H. Briggs. Cosmology at low frequencies: The 21cm transition and the high-redshift Universe. *Physics Reports*, 433(4):181 – 301, 2006. ISSN 0370-1573. doi: https://doi.org/10.1016/j.physrep.2006.08.002. URL http://www.sciencedirect.com/science/article/pii/S0370157306002730.

A. A. Galeev, R. Z. Sagdeev, V. D. Shapiro, and V. I. Shevchenko. Relaxation of high-current electron beams and the modulational instability. *Sov. Phys. JETP*, 45(2):266, 1977.

B. B. Godfrey. Numerical Cherenkov Instabilities in Electromagnetic Particle Codes. *Journal of Computational Physics*, 15:504–521, August 1974. doi: 10.1016/0021-9991(74)90076-X.

Brendan B. Godfrey and Jean-Luc Vay. Suppressing the numerical Cherenkov instability in FDTD PIC codes. *Journal of Computational Physics*, 267(Supplement C):1 – 6, 2014. ISSN 0021-9991. doi: https://doi.org/10.1016/j.jcp.2014.02.022. URL http://www.sciencedirect.com/science/article/pii/S0021999114001429.

Brendan B. Godfrey, William R. Shanahan, and Lester E. Thode. Linear theory of a cold relativistic beam propagating along an external magnetic field. *The Physics of Fluids*, 18(3):346–355, 1975. doi: 10.1063/1.861144. URL http://aip.scitation.org/doi/abs/10.1063/1.861144.

Andrew D. Greenwood, Keith L. Cartwright, John W. Luginsland, and Ernest A. Baca. On the elimination of numerical Cerenkov radiation in PIC simulations. *Journal of Computational Physics*, 201(2):665 – 684, 2004. ISSN 0021-9991. doi: https://doi.org/10.1016/j.jcp.2004.06.021. URL http://www.sciencedirect.com/science/article/pii/S0021999104002608.

R. C. Hartman, D. L. Bertsch, S. D. Bloom, A. W. Chen, P. Deines-Jones, J. A. Esposito, C. E. Fichtel, D. P. Friedlander, S. D. Hunter, L. M. McDonald, P. Sreekumar, D. J. Thompson, B. B. Jones, Y. C. Lin, P. F. Michelson, P. L. Nolan, W. F. Tompkins, G. Kanbach, H. A. Mayer-Hasselwander, A. Mücke, M. Pohl, O. Reimer, D. A. Kniffen, E. J. Schneid, C. von Montigny, R. Mukherjee, and B. L. Dingus. The Third EGRET Catalog of High-Energy Gamma-Ray Sources. *The Astrophysical Journal Supplement Series*, 123(1):79, 1999. URL http://stacks.iop.org/0067-0049/123/i=1/a=79.

H.E.S.S. Collaboration. Search for extended $\gamma$-ray emission around AGN with H.E.S.S. and Fermi-LAT. *A&A*, 562:A145, 2014. doi: 10.1051/0004-6361/201322510. URL http://dx.doi.org/10.1051/0004-6361/201322510.

J.A. Hinton and W. Hofmann. Teraelectronvolt Astronomy. *Annual Review of Astronomy and Astrophysics*, 47(1):523–565, 2009. doi: 10.1146/annurev-astro-082708-101816. URL https://doi.org/10.1146/annurev-astro-082708-101816.

R. W. Hockney and J. W. Eastwood. *Computer simulation using particles*. CRC Press, 1988.

E. M. Hu, T.-S. Kim, L. L. Cowie, A. Songaila, and M. Rauch. The Distribution of Column Densities and B Values in the Lyman-Alpha Forest. , 110:1526, October 1995. doi: 10.1086/117625.

A. Kempf, P. Kilian, and F. Spanier. Energy loss in intergalactic pair beams: Particle-in-cell simulation. *A & A*, 585:A132, 2016. doi: 10.1051/0004-6361/201527521. URL https://doi.org/10.1051/0004-6361/201527521.

T.-S. Kim, E. M. Hu, L. L. Cowie, and A. Songaila. The Redshift Evolution of the Ly alpha Forest. , 114:1–13, July 1997. doi: 10.1086/118446.

David Kirkman and David Tytler. Intrinsic Properties of the z = 2.7 Ly Forest from Keck Spectra of Quasar HS 1946+7658. *The Astrophysical Journal*, 484(2):672, 1997. URL http://stacks.iop.org/0004-637X/484/i=2/a=672.

Kneiske, T. M., Bretz, T., Mannheim, K., and Hartmann, D. H. Implications of cosmological gamma-ray absorption - II. Modification of gamma-ray spectra. *A & A*, 413(3):807–815, 2004. doi: 10.1051/0004-6361:20031542. URL https://doi.org/10.1051/0004-6361:20031542.

Edward W. Kolb and Michael S. Turner. *The Early Universe*, volume 69. Addison-Wesley, 1990.

Hannu E. J Koskinen. *Physics of space storms from the solar surface the Earth*. Springer ; Published in association with Praxis Pub., Berlin; London; Chichester, UK, 2011. ISBN 9783642003196 3642003192. URL http://dx.doi.org/10.1007/978-3-642-00319-6.

W. L. Kruer and J. M. Dawson. Sideband Instability. *The Physics of Fluids*, 13(11):2747–2751, 1970. doi: 10.1063/1.1692859. URL http://aip.scitation.org/doi/abs/10.1063/1.1692859.

W. L. Kruer, J. M. Dawson, and R. N. Sudan. Trapped-Particle Instability. *Phys. Rev. Lett.*, 23:838–841, Oct 1969. doi: 10.1103/PhysRevLett.23.838. URL https://link.aps.org/doi/10.1103/PhysRevLett.23.838.

Girish Kulkarni, Joseph F. Hennawi, Jose Oñorbe, Alberto Rorai, and Volker Springel. Characterizing the Pressure Smoothing Scale of the Intergalactic Medium. *The Astrophysical Journal*, 812(1):30, 2015. URL http://stacks.iop.org/0004-637X/812/i=1/a=30.

L. D. Landau. On the vibrations of the electronic plasma. *J. Phys.(USSR)*, 10:25–34, 1946. [Zh. Eksp. Teor. Fiz.16,574(1946)].

D. G. Lominadze and A. B. Mikhailovskii. Longitudinal waves and two-stream instability in a relativistic plasma. *Sov. Phys. JETP*, 49:483, Jul 1979. URL http://www.jetp.ac.ru/cgi-bin/dn/e_049_03_0483.pdf.

P. Madau, A. Meiksin, and M. J. Rees. 21 Centimeter Tomography of the Intergalactic Medium at High Redshift. , 475:429–444, February 1997. doi: 10.1086/303549.

Piero Madau. The intergalactic medium. *arXiv:astro-ph/0005106*, 2000.

K. Mannheim. The proton blazar. , 269:67–76, March 1993.

L. Maraschi, G. Ghisellini, and A. Celotti. A jet model for the gamma-ray emitting blazar 3C 279. , 397:L5–L9, September 1992. doi: 10.1086/186531.

J. C. Mather, E. S. Cheng, R. E. Eplee, Jr., R. B. Isaacman, S. S. Meyer, R. A. Shafer, R. Weiss, E. L. Wright, C. L. Bennett, N. W. Boggess, E. Dwek, S. Gulkis, M. G. Hauser, M. Janssen, T. Kelsall, P. M. Lubin, S. H. Moseley, Jr., T. L. Murdock, R. F. Silverberg, G. F. Smoot, and D. T. Wilkinson. A preliminary measurement of the cosmic microwave background spectrum by the Cosmic Background Explorer (COBE) satellite. , 354: L37–L40, May 1990. doi: 10.1086/185717.

B.E. Meierovich and S.T. Sukhorukov. Equilibrium structure of relativistic beams. *Sov. Phys. JETP*, 41(5):895, 1975.

Francesco Miniati and Andrii Elyiv. Relaxation of Blazar-induced Pair Beams in Cosmic Voids. *The Astrophysical Journal*, 770(1):54, 2013. URL http://stacks.iop.org/0004-637X/770/i=1/a=54.

David Campbell Montgomery and Derek A Tidman. *Plasma kinetic theory*. New York : McGraw-Hill, 1964. Based on lectures given at the Goddard Space Flight Center of N.A.S.A. during the spring semester of 1962-63.

S. Naoz, S. Noter, and R. Barkana. The first stars in the Universe. , 373:L98–L102, November 2006. doi: 10.1111/j.1745-3933.2006.00251.x.

A. Neronov and D. V. Semikoz. Sensitivity of $\gamma$-ray telescopes for detection of magnetic fields in the intergalactic medium. *Phys. Rev. D*, 80:123012, Dec 2009. doi: 10.1103/PhysRevD.80.123012. URL https://link.aps.org/doi/10.1103/PhysRevD.80.123012.

Andrii Neronov and Ievgen Vovk. Evidence for Strong Extragalactic Magnetic Fields from Fermi Observations of TeV Blazars. *Science*, 328(5974):73–75, 2010. ISSN 0036-8075. doi: 10.1126/science.1184192. URL http://science.sciencemag.org/content/328/5974/73.

K. Papadopoulos. Nonlinear stabilization of beam plasma interactions by parametric effects. *The Physics of Fluids*, 18(12):1769–1777, 1975. doi: 10.1063/1.861096. URL http://aip.scitation.org/doi/abs/10.1063/1.861096.

R. Plaga. Detecting intergalactic magnetic fields using time delays in pulses of $\gamma$-rays. , 374: 430–432, March 1995. doi: 10.1038/374430a0.

Planck Collaboration. Planck 2015 results. IX. Diffuse component separation: CMB maps. , 594, September 2016. doi: 10.1051/0004-6361/201525936.

Joel R. Primack, Rudy C. Gilmore, and Rachel S. Somerville. Diffuse Extragalactic Background Radiation. *AIP Conference Proceedings*, 1085(1):71–82, 2008. doi: 10.1063/1.3076779. URL http://aip.scitation.org/doi/abs/10.1063/1.3076779.

M. Punch, C. W. Akerlof, M. F. Cawley, M. Chantell, D. J. Fegan, S. Fennell, J. A. Gaidos, J. Hagan, A. M. Hillas, Y. Jiang, A. D. Kerrick, R. C. Lamb, M. A. Lawrence, D. A. Lewis, D. I. Meyer, G. Mohanty, K. S. O'Flaherty, P. T. Reynolds, A. C. Rovero, M. S. Schubnell, G. Sembroski, T. C. Weekes, and C. Wilson. Detection of TeV photons from the active galaxy Markarian 421. , 358:477, August 1992. doi: 10.1038/358477a0.

I. Rafighi, S. Vafin, M. Pohl, and J. Niemiec. Plasma effects on relativistic pair beams from TeV blazars: PIC simulations and analytical predictions. *A & A*, 607:A112, 2017. doi: 10.1051/0004-6361/201731127. URL https://doi.org/10.1051/0004-6361/201731127.

Gwen C. Rudie, Charles C. Steidel, and Max Pettini. The Temperature-Density Relation in the Intergalactic Medium at Redshift z = 2.4. *The Astrophysical Journal Letters*, 757(2): L30, 2012. URL http://stacks.iop.org/2041-8205/757/i=2/a=L30.

R. Schlickeiser. *Cosmic Ray Astrophysics*. Springer Berlin Heidelberg, 2002.

R. Schlickeiser. Covariant kinetic dispersion theory of linear waves in anisotropic plasmas. I. General dispersion relations, bi-Maxwellian distributions and nonrelativistic limits. *Physics of Plasmas*, 11(12):5532–5546, 2004. doi: 10.1063/1.1806828. URL http://dx.doi.org/10.1063/1.1806828.

R. Schlickeiser. General properties of small-amplitude fluctuations in magnetized and unmagnetized collision poor plasmas. I. The dielectric tensor. *Physics of Plasmas*, 17(11): 112105, 2010. doi: 10.1063/1.3505309. URL https://doi.org/10.1063/1.3505309.

R. Schlickeiser, R. Vainio, M. Böttcher, I. Lerche, M. Pohl, and C. Schuster. Conversion of relativistic pair energy into radiation in the jets of active galactic nuclei. *A & A*, 393(1): 69–87, 2002. doi: 10.1051/0004-6361:20020975. URL https://doi.org/10.1051/0004-6361:20020975.

R. Schlickeiser, A. Elyiv, D. Ibscher, and F. Miniati. The Pair Beam Production Spectrum from Photon-Photon Annihilation in Cosmic Voids. *The Astrophysical Journal*, 758(2): 101, 2012a. URL http://stacks.iop.org/0004-637X/758/i=2/a=101.

R. Schlickeiser, D. Ibscher, and M. Supsar. Plasma Effects on Fast Pair Beams in Cosmic Voids. *The Astrophysical Journal*, 758(2):102, 2012b. URL http://stacks.iop.org/0004-637X/758/i=2/a=102.

R. Schlickeiser, S. Krakau, and M. Supsar. Plasma Effects on Fast Pair Beams. II. Reactive versus Kinetic Instability of Parallel Electrostatic Waves. *The Astrophysical Journal*, 777 (1):49, 2013. URL http://stacks.iop.org/0004-637X/777/i=1/a=49.

Mohamad Shalaby, Avery E. Broderick, Philip Chang, Christoph Pfrommer, Astrid Lamberts, and Ewald Puchwein. Importance of Resolving the Spectral Support of Beam-plasma Instabilities in Simulations. *The Astrophysical Journal*, 848(2):81, 2017. URL http://stacks.iop.org/0004-637X/848/i=2/a=81.

Lorenzo Sironi and Dimitrios Giannios. Relativistic Pair Beams from TeV Blazars: A Source of Reprocessed GeV Emission rather than Intergalactic Heating. *The Astrophysical Journal*, 787(1):49, 2014. URL http://stacks.iop.org/0004-637X/787/i=1/a=49.

V. Springel, S. D. M. White, A. Jenkins, C. S. Frenk, N. Yoshida, L. Gao, J. Navarro, R. Thacker, D. Croton, J. Helly, J. A. Peacock, S. Cole, P. Thomas, H. Couchman, A. Evrard, J. Colberg, and F. Pearce. Simulations of the formation, evolution and clustering of galaxies and quasars. , 435:629–636, June 2005. doi: 10.1038/nature03597.

A. M. Taylor, I. Vovk, and A. Neronov. Extragalactic magnetic fields constraints from simultaneous GeV–TeV observations of blazars. *A & A*, 529:A144, 2011. doi: 10.1051/0004-6361/201116441. URL https://doi.org/10.1051/0004-6361/201116441.

D. J. Thompson, D. L. Bertsch, B. L. Dingus, J. A. Esposito, A. Etienne, C. E. Fichtel, D. P. Friedlander, R. C. Hartman, S. D. Hunter, D. J. Kendig, J. R. Mattox, L. M. McDonald, C. von Montigny, R. Mukherjee, P. V. Ramanamurthy, P. Sreekumar, J. M. Fierro, Y. C. Lin, P. F. Michelson, P. L. Nolan, S. K. Shriver, T. D. Willis, G. Kanbach, H. A. Mayer-Hasselwander, M. Merck, H.-D. Radecke, D. A. Kniffen, and E. J. Schneid. The Second EGRET Catalog of High-Energy Gamma-Ray Sources. , 101:259, December 1995. doi: 10.1086/192240.

Michele Trenti and Massimo Stiavelli. Formation Rates of Population III Stars and Chemical Enrichment of Halos during the Reionization Era. *The Astrophysical Journal*, 694(2):879, 2009. URL http://stacks.iop.org/0004-637X/694/i=2/a=879.

C. Megan Urry and Paolo Padovani. Unified Schemes for Radio-Loud Active Galactic Nuclei. *Publications of the Astronomical Society of the Pacific*, 107(715):803, 1995. URL http://stacks.iop.org/1538-3873/107/i=715/a=803.

S. Vafin, I. Rafighi, M. Pohl, and J. Niemiec. The Electrostatic Instability for Realistic Pair Distributions in Blazar/EBL Cascades. *The Astrophysical Journal*, 857(1):43, 2018. URL http://stacks.iop.org/0004-637X/857/i=1/a=43.

J.-L. Vay, C.G.R. Geddes, E. Cormier-Michel, and D.P. Grote. Numerical methods for instability mitigation in the modeling of laser wakefield accelerators in a Lorentz-boosted frame. *Journal of Computational Physics*, 230(15):5908 – 5929, 2011. ISSN 0021-9991. doi: https://doi.org/10.1016/j.jcp.2011.04.003. URL http://www.sciencedirect.com/science/article/pii/S0021999111002270.

Jean-Luc Vay, Irving Haber, and Brendan B. Godfrey. A domain decomposition method for pseudo-spectral electromagnetic simulations of plasmas. *Journal of Computational Physics*, 243(Supplement C):260 – 268, 2013. ISSN 0021-9991. doi: https://doi.org/10.1016/j.jcp.2013.03.010. URL http://www.sciencedirect.com/science/article/pii/S0021999113001873.

John Villasenor and Oscar Buneman. Rigorous charge conservation for local electromagnetic field solvers. *Computer Physics Communications*, 69(2):306 – 316, 1992. ISSN 0010-4655. doi: https://doi.org/10.1016/0010-4655(92)90169-Y. URL http://www.sciencedirect.com/science/article/pii/001046559290169Y.

Mark Vogelsberger, Shy Genel, Volker Springel, Paul Torrey, Debora Sijacki, Dandan Xu, Greg Snyder, Dylan Nelson, and Lars Hernquist. Introducing the Illustris Project: simulating the coevolution of dark and visible matter in the universe. *Monthly Notices of the Royal Astronomical Society*, pages 1518–1547, 2014. doi: 10.1093/mnras/stu1536. URL +http://dx.doi.org/10.1093/mnras/stu1536.

Steven S. Vogt, Steven L. Allen, Bruce C. Bigelow, L. Bresee, T. Cantrall William E. Brown, Albert Conrad, M. Couture, C. Delaney, Harland W. Epps, Darrie Hilyard, David F. Hilyard, E. Horn, D. Kanto Neal Jern, Michael J. Keane, Robert I. Kibrick, James W. Lewis, Jack Osborne, Gerard H. Pardeilhan, Terry Pfister, T. Ricketts, Lloyd B. Robinson, Richard J. Stover, Dean Tucker, Janice M. Ward, and Mingzhi Wei. HIRES the high-resolution echelle spectrometer on the Keck 10-m Telescope. *Proc.SPIE*, 2198:2198 – 2198 – 14, 1994. doi: 10.1117/12.176725. URL https://doi.org/10.1117/12.176725.

K. M. Watson, S. A. Bludman, and M. N. Rosenbluth. Statistical Mechanics of Relativistic Streams. I. *The Physics of Fluids*, 3(5):741–747, 1960. doi: 10.1063/1.1706120. URL http://aip.scitation.org/doi/abs/10.1063/1.1706120.

T. C. Weekes, M. F. Cawley, D. J. Fegan, K. G. Gibbs, A. M. Hillas, P. W. Kowk, R. C. Lamb, D. A. Lewis, D. Macomb, N. A. Porter, P. T. Reynolds, and G. Vacanti. Observation of TeV gamma rays from the Crab nebula using the atmospheric Cerenkov imaging technique. , 342:379–395, July 1989. doi: 10.1086/167599.

Kane Yee. Numerical solution of initial boundary value problems involving maxwell's equations in isotropic media. *IEEE Transactions on Antennas and Propagation*, 14(3): 302–307, May 1966. ISSN 0018-926X. doi: 10.1109/TAP.1966.1138693.

Peter H. Yoon and Ronald C. Davidson. Exact analytical model of the classical weibel instability in a relativistic anisotropic plasma. *Phys. Rev. A*, 35:2718–2721, Mar 1987. doi: 10.1103/PhysRevA.35.2718. URL https://link.aps.org/doi/10.1103/PhysRevA.35.2718.

Seiji Zenitani. Loading relativistic Maxwell distributions in particle simulations. *Physics of Plasmas*, 22(4):042116, 2015. doi: 10.1063/1.4919383. URL http://dx.doi.org/10.1063/1.4919383.

# Appendix A

# Appendix for monoenergetic beams

## A.1 Derivation of the dispersion equation for $p_{\perp,b} = p_{\|,p} = p_{\perp,p} = 0$ and $k_{\|} = 0$

In the case $p_{\perp,b} = p_{\|,p} = p_{\perp,p} = 0$, the beam and plasma distributions, respectively, reads

$$f_b(\mathbf{p}) = \frac{n_b}{(p^+_{\|,b} - p^-_{\|,b})}\delta(p_z)\delta(p_y)\left[\theta\left(p_x - p^-_{\|,b}\right) - \theta\left(p_x - p^+_{\|,b}\right)\right], \tag{A.1}$$

$$f_p(\mathbf{p}) = n\delta(p_x)\delta(p_y)\delta(p_z), \tag{A.2}$$

where $\delta(x)$ is the Dirac delta function. The dielectric tensor is given by Breizman (1990) and Schlickeiser (2004):

$$\varepsilon_{i,j} = \delta_{i,j} + \sum_{a=p,b}\frac{4\pi e^2}{\omega^2}\int d^3p\left(v_i\frac{\partial f_a(\mathbf{p})}{\partial p_j} - \frac{v_i v_j k_l}{\mathbf{kv} - \omega}\frac{\partial f_a(\mathbf{p})}{\partial p_l}\right). \tag{A.3}$$

Evaluating the dielectric tensor (A.3) for the distribution functions (A.1)-(A.2) and for the wave vector $\mathbf{k} = (0,0,k)$ yields

$$\varepsilon_{zy} = \varepsilon_{yz} = \varepsilon_{yx} = \varepsilon_{xy} = 0, \tag{A.4}$$

$$\varepsilon_{zz} = \varepsilon_{yy} = 1 - \frac{\omega_p^2}{\omega} - \frac{\omega_b^2}{\omega^2}U_1, \tag{A.5}$$

$$\varepsilon_{xx} = 1 - \frac{\omega_p^2}{\omega^2} - \frac{\omega_b^2}{\omega^2}\left[\left(\frac{kc}{\omega}\right)^2 U_1 + \left(1 - \left(\frac{kc}{\omega}\right)^2\right)U_2\right], \tag{A.6}$$

$$\varepsilon_{xz} = \varepsilon_{zx} = -\frac{\omega_b^2}{\omega^2}\frac{kc}{\omega}U_3, \tag{A.7}$$

where

$$U_1 = \frac{m_e c}{p_{\parallel,b}^+ - p_{\parallel,b}^-}\ln\left|\frac{p_{\parallel,b}^+ + [(p_{\parallel,b}^+)^2 + m_e^2c^2]^{1/2}}{p_{\parallel,b}^- + [(p_{\parallel,b}^-)^2 + m_e^2c^2]^{1/2}}\right|, \tag{A.8}$$

$$U_2 = \frac{m_e c}{p_{\parallel,b}^+ - p_{\parallel,b}^-}\left(\frac{p_{\parallel,b}^+}{[(p_{\parallel,b}^+)^2 + m_e^2c^2]^{1/2}} - \frac{p_{\parallel,b}^-}{[(p_{\parallel,b}^-)^2 + m_e^2c^2]^{1/2}}\right), \tag{A.9}$$

$$U_3 = \frac{m_e c}{2(p_{\parallel,b}^+ - p_{\parallel,b}^-)}\ln\left|\frac{(p_{\parallel,b}^+)^2 + m_e^2c^2}{(p_{\parallel,b}^-)^2 + m_e^2c^2}\right|. \tag{A.10}$$

Here, we have introduced $\omega_b^2 = 8\pi n_b e^2/m_e$. The dispersion equation reads:

$$\det(\Lambda_{i,j}) = \det\left(\varepsilon_{i,j} + \frac{k_i k_j c^2}{\omega^2} - \left(\frac{kc}{\omega}\right)^2\delta_{i,j}\right) = \Lambda_{yy}(\Lambda_{zz}\Lambda_{xx} - \Lambda_{zx}^2) = 0. \tag{A.11}$$

Thus, the dispersion equation for electromagnetic fluctuations is

$$\begin{aligned}\left[1 - \frac{\omega_p^2}{\omega} - \frac{\omega_b^2}{\omega^2}U_1\right]\Bigg\{1 - \left(\frac{kc}{\omega}\right)^2 - \frac{\omega_p^2}{\omega^2} - \\ - \frac{\omega_b^2}{\omega^2}\left[\left(\frac{kc}{\omega}\right)^2 U_1 + \left(1 - \left(\frac{kc}{\omega}\right)^2\right)U_2\right]\Bigg\} - \\ - \left(\frac{\omega_b^2}{\omega^2}\frac{kc}{\omega}U_3\right)^2 = 0.\end{aligned} \tag{A.12}$$

## A.2 Derivation of the dispersion equation for $p_{\parallel,b} = 0$ and $k_\parallel = 0$

For $p_{\parallel,b} = 0$, the distribution function of the beam reads

$$\begin{aligned}f_b(\mathbf{p}) = \frac{n_b}{4p_{\perp,b}^2}\left[\theta\left(p_z + p_{\perp,b}\right) - \theta\left(p_z - p_{\perp,b}\right)\right] \times \\ \times \left[\theta\left(p_y + p_{\perp,b}\right) - \theta\left(p_y - p_{\perp,b}\right)\right]\delta(p_x - p_0).\end{aligned} \tag{A.13}$$

We will assume $p_{\perp,b} \ll p_0$. We will still model background protons with the distribution (A.2), whereas the distribution function of the background electrons is given by Eq. (3.50).

Moreover, we will assume that the background electrons are non-relativistic, $p_{\|,p} = m_e v_{\|,p}$ and $p_{\perp,p} = m_e v_{\perp,p}$. Now, it is easy to find that again $\varepsilon_{zy} = \varepsilon_{yz} = \varepsilon_{yx} = \varepsilon_{xy} = 0$, but

$$\varepsilon_{zz} = 1 - \frac{\omega_{p,p}^2}{\omega^2} - \frac{\omega_{p,e}^2}{\omega^2 - (kv_{\perp,p})^2} - \frac{\omega_b^2/\Gamma}{\omega^2 - (ku)^2}, \tag{A.14}$$

$$\varepsilon_{yy} = 1 - \frac{\omega_p^2 + \omega_b^2/\Gamma}{\omega^2} - \frac{(kv_{\perp,p})^2 \omega_{p,e}^2}{3\omega^2(\omega^2 - (kv_{\perp,p})^2)} - \frac{(ku)^2 \omega_b^2/\Gamma}{3\omega^2(\omega^2 - (ku)^2)}, \tag{A.15}$$

$$\varepsilon_{xx} = 1 - \frac{\omega_p^2 + \omega_b^2/\Gamma^3}{\omega^2} - \frac{(kv_{\|,p})^2 \omega_{p,e}^2}{3\omega^2(\omega^2 - (kv_{\perp,p})^2)} - \frac{(kV_0)^2 \omega_b^2/\Gamma}{\omega^2(\omega^2 - (ku)^2)}, \tag{A.16}$$

$$\varepsilon_{xz} = \varepsilon_{zx} = -\frac{kV_0 \omega_b^2/\Gamma}{\omega(\omega^2 - (ku)^2)}, \tag{A.17}$$

where $\omega_{p,e} = (4\pi ne^2/m_e)^{1/2}$, $\omega_{p,p} = (4\pi ne^2/m_p)^{1/2}$ ($m_p$ is the proton mass), $u = V_0 p_{\perp,b}/p_0$.

Finally, the Weibel instability is described by the equation

$$\begin{aligned}&\left[1 - \frac{\omega_{p,p}^2}{\omega^2} - \frac{\omega_{p,e}^2}{\omega^2 - (kv_{\perp,p})^2} - \frac{\omega_b^2/\Gamma}{\omega^2 - (ku)^2}\right] \times \\ &\quad \times \left[1 - \frac{(kc)^2 + \omega_p^2 + \omega_b^2/\Gamma^3}{\omega^2} - \frac{(kv_{\|,p})^2 \omega_{p,e}^2}{3\omega^2(\omega^2 - (kv_{\perp,p})^2)} - \right. \\ &\quad\quad \left. - \frac{(kV_0)^2 \omega_b^2/\Gamma}{\omega^2(\omega^2 - (ku)^2)}\right] - \left[\frac{kV_0 \omega_b^2/\Gamma}{\omega(\omega^2 - (ku)^2)}\right]^2 = 0.\end{aligned} \tag{A.18}$$

## A.3 Approximation for $\alpha_{kin}$ at large values of $\mu_R$

For $\mu_R \gg 1$, we can use the series expansion

$$c(p^2 + m_e^2 c^2)^{1/2} - V_0 p_x \approx \frac{mc^2}{\Gamma} + \frac{(p_x - p_0)^2}{2m_e \Gamma^3} + \frac{p_z^2 + p_y^2}{2m_e \Gamma}. \tag{A.19}$$

Then Eq. (3.59) can be approximated as (Meierovich and Sukhorukov, 1975; Watson et al., 1960)

$$f_b(\mathbf{p}) = \frac{n_b}{\pi^{3/2} p_{\perp,b}^2 p_{\|,b}} e^{-\frac{p_z^2 + p_y^2}{p_{\perp,b}^2} - \frac{(p_x - p_0)^2}{p_{\|,b}^2}}, \tag{A.20}$$

or

$$f_b(\mathbf{v}) = \frac{n_b}{\pi^{3/2} v_{\perp,b}^2 v_{\parallel,b}} e^{-\frac{v_z^2+v_y^2}{v_{\perp,b}^2} - \frac{(v_x-v_0)^2}{v_{\parallel,b}^2}}, \tag{A.21}$$

where $p_{\perp,b}^2 = 2m_e k_B T_b$, $p_{\parallel,b}^2 = 2\Gamma^2 m_e k_B T_b$, $v_{\perp,b}^2 = 2k_B T_b/(m_e\Gamma^2)$, $v_{\parallel,b}^2 = 2k_B T_b/(m_e\Gamma^4)$. It is easy to find that

$$p_{\perp,b} = (2-\pi/2)^{1/2} \frac{mc}{\mu_R^{1/2}} \tag{A.22}$$

$$v_{\parallel,b} = \left(\langle (v_x - \langle v_x\rangle)^2 \rangle\right)^{1/2} \approx \left(\frac{k_B T_b}{m_e \Gamma^4}\right)^{1/2} \tag{A.23}$$

and

$$\alpha_{kin} = \frac{1}{\Gamma^3 \mu_R^{3/2}}. \tag{A.24}$$

# Appendix B

# Realistic pair beams

## B.1 Realistic pair spectrum

To investigate the growth rate of the electrostatic instability, it is necessary to evaluate the energy distribution of realistic blazar-induced pairs. Let us consider a fiducial source of high-energy photons with spectrum $F(E_\gamma, z) = dN_\gamma/dE_\gamma$. Of interest are BL Lac objects with an intrinsic emission spectrum harder than $E^{-2}$ that extends to at least a few TeV; otherwise, the cascade emission would be subdominant and would not fall into the energy band accessible with the *Fermi*-LAT. Only a few of the AGNs known in the GeV band qualify (Abdo et al., 2010). For our fiducial BL Lac, we assume a simple power-law spectrum observable at Earth,

$$F(E_\gamma, z=0) = \left(10^{-9}\,\frac{\text{ph.}}{\text{cm}^2\,\text{s}\,\text{GeV}}\right)\left(\frac{E_\gamma}{\text{GeV}}\right)^{-1.8}\Theta((E_\gamma - E_{\gamma,min})(E_{\gamma,max} - E_\gamma)), \quad \text{(B.1)}$$

where $E_{\gamma,min} = 0.5$ GeV and $E_{\gamma,max} = 50$ TeV. The low-energy limit is irrelevant for our work, and a high-energy limit is chosen to explore a case with high pair-beam density and hence strong driving of plasma instabilities. The differential flux at 1 TeV corresponds to 15% of that of the Crab nebula and is typical of BL Lacs in the flaring state (Hinton and Hofmann, 2009). The AGN is placed at redshift $z = 0.15$, corresponding to a luminosity distance $D_\mathrm{L} \simeq 720$ Mpc.

Gamma-ray emission from jets of AGNs has a finite opening angle, and at the site of pair production, at the distance $D_\gamma$ from the AGN, the gamma-ray flux is

$$F(E_\gamma, D_\gamma) = \frac{D_\mathrm{L}^2}{D_\gamma^2} F(E_\gamma, z=0)\ , \quad \text{(B.2)}$$

where the energy is measured at $z = 0$. As the density of the pair-beam scales with that of the primary gamma rays, it is important to establish at what distance the bulk of pair production happens. Primary gamma rays with $E_\gamma = 40$ TeV produce cascade emission above 100 GeV, where the sensitivity of *Fermi*-LAT deteriorates. They also get absorbed within a few Mpc from the AGN, i.e., close to, or in, a cosmological filament where a magnetic field stronger than the fG-level likely exists. Gamma-rays with $E_\gamma = 10$ TeV have a mean-free path of roughly 80 Mpc, i.e., they pair-produce in voids, and provide well-detectable cascade emission around 10 GeV. Then, pair beams produced at $D_\gamma \simeq 50$ Mpc represent the best test case for the role of electrostatic instabilities in voids, because one considers the highest beam densities at the location of main energy transfer under the constraint of cascade visibility. For our fiducial AGN, the total number of gamma rays then is

$$N_\gamma = \int dE_\gamma\, F(E_\gamma, D_\gamma = 50\,\mathrm{Mpc}) \simeq 1.5 \cdot 10^{-17}\ . \tag{B.3}$$

Note that at $D_\gamma \simeq 50$ Mpc, absorption has already diminished the gamma-ray flux above 10 TeV.

The spectrum of the EBL is denoted as $f(\varepsilon, z) = dn_\gamma/d\varepsilon$. We define a small redshift interval, $\delta z$, for which $z_b(i)$ $(i = 0, 1, 2...)$ represents the boundaries and $z_c(i)$ the center of the interval. In this redshift interval, the evolution of $F(E_\gamma, z)$ can be linearised as done by Fang (2010)

$$F(E_\gamma, z_b(i\,+\,1)) \;=\; F(E_\gamma, z_b(i))e^{-\delta\tau(E_\gamma, z_c(i))} \;\approx\; F(E_\gamma, z_b(i))[1\,-\,\delta\tau(E_\gamma, z_c(i))], \tag{B.4}$$

where the optical depth for the small step $\delta z$ in redshift is

$$\delta\tau(E_\gamma, z) = c\delta z \frac{dt}{dz}\int_0^2 dx \frac{x}{2}\int_{e_th}^\infty d\varepsilon f(\varepsilon, z)(1+z)^3\sigma_{\gamma\gamma}(\beta). \tag{B.5}$$

Here,

$$\frac{dt}{dz} = \frac{1}{H_0(1+z)}\left[(1+z)^2(1+\Omega_m z) - z(z+2)\Omega_\Lambda\right]^{-1/2}, \tag{B.6}$$

with Hubble constant $H_0 = 70$ km s$^{-1}$ Mpc$^{-1}$, $\Omega_m = 0.3$, $\Omega_\Lambda = 0.7$, $c$ is the speed of light, while

$$\sigma_{\gamma\gamma}(\beta) = \frac{3\sigma_T}{16}(1-\beta^2)\left[2\beta(\beta^2-2) + (3-\beta^4)\ln\left(\frac{1+\beta}{1-\beta}\right)\right] \tag{B.7}$$

describes the cross-section for pair production, where the Thompson cross-section $\sigma_T = 6.65\times 10^{-25}$ cm$^2$, $\beta = (1-4m_e^2c^4/s)^{1/2}$, $s = 2E_\gamma\varepsilon x(1+z)$, $x = 1-\cos\theta$, and $m_e$ is the electron mass.

The distribution function of newly produced electrons and positrons can be expressed as (Fang, 2010)

$$\begin{aligned}\delta f_b(\gamma, z_b(i+1)) = \frac{dn_b}{d\gamma} = c\delta z \frac{dt}{dz}\frac{(1+z_c(i))^2}{4}\int_0^\infty dE_\gamma F(E_\gamma, z_b(i))E_\gamma^2 \int_1^\infty d\gamma^* \times \\ \int_{\gamma^-}^{\gamma^+} \frac{d\gamma_{CM}}{\sqrt{(\gamma^{*2}-1)\,(\gamma_{CM}^2-1)}}\frac{1}{\gamma_{CM}^5}\,\delta\left(\gamma^* - \frac{\gamma_{max}}{\gamma_{CM}}\right)\int_{\varepsilon_{min}}^\infty \frac{d\varepsilon}{\varepsilon^2} f(\varepsilon, z_c(i))\sigma_{\gamma\gamma}(\beta),\end{aligned} \tag{B.8}$$

where $\gamma^{\pm} = \gamma\gamma^* \pm \sqrt{(\gamma^{*2}-1)\,(\gamma^2-1)}$, $\beta = \sqrt{1-\gamma_{CM}^2/\gamma_{max}^2}$, $\gamma_{max} = E_\gamma(1+z_c(i))/(2m_ec^2)$, and $\varepsilon_{min} = E_\gamma(1+z_c(i))/(4\gamma_{CM}^2)$. Here, $\gamma_{CM}$ is the gamma-factor of the center-of-mass frame of the interacting photons and $\gamma^*$ is the gamma-factor of pairs in that frame. Integrating Eq. (B.8) over $\gamma_{CM}$ and introducing the new variable $x = \gamma_{max}/\gamma^*$, Eq. (B.8) becomes

$$\begin{aligned}\delta f_b(\gamma, z_b(i+1)) = c\delta z \frac{dt}{dz}\frac{(1+z_c(i))^2}{4} \times \\ \int_0^\infty dE_\gamma\, F(E_\gamma, z_b(i))E_\gamma^2 \int_0^{\gamma_{max}} dx\, \frac{\Theta\left((x-\gamma^-)\,(\gamma^+-x)\right)}{x^5\sqrt{((\gamma_{max}/x)^2-1)\,(x^2-1)}}\int_{\varepsilon_{min}}^\infty \frac{d\varepsilon}{\varepsilon^2} f(\varepsilon, z_c(i))\sigma_{\gamma\gamma}(\beta),\end{aligned} \tag{B.9}$$

where $\Theta$ is the Heaviside step function, $\beta = \sqrt{1-x^2/\gamma_{max}^2}$, $\varepsilon_{min} = E_\gamma(1+z_c(i))/(4x^2)$, and $\gamma^{\pm} = \gamma\gamma_{max}/x \pm \sqrt{(\gamma^2-1)((\gamma_{max}/x)^2-1)}$. Thus, for given $F(E_\gamma, z_b(i))$ and $f(\varepsilon, z_c(i))$, Eq. (B.9) yields the increment of the pair distribution function.

The energy spectrum of low-energy EBL photons is modeled by a combination of stellar radiation and cosmic X-ray background. For the stellar radiation, we used results by Finke et al. (2010) for the redshift 0.2, also available online,[1] whereas the X-ray background radiation is described by empirical fits found by Fabian and Barcons (1992). Note that Schlickeiser et al. (2013) used an EBL spectrum of Wien-type,

$$f(\varepsilon) = \frac{N_0}{\Gamma(3)k_BT_W}\left(\frac{\varepsilon}{k_BT_W}\right)^2 \exp\left(-\frac{\varepsilon}{k_BT_W}\right), \tag{B.10}$$

where $\Gamma$ denotes the Gamma function, $k_BT_W = 0.1$ eV, and $N_0 = 1$ cm$^{-3}$. Fig. B.1 compares model spectra of the EBL. It is obvious that the Wien-type distribution Eq. (B.10) is not a good description of the realistic EBL spectrum given by stellar radiation and CXB. Thus, in the present work, we will use an analytical approximation (see Appendix B.2) for the

---

[1] http://www.phy.ohiou.edu/∼finke/EBL/index.html

spectral models by Finke et al. (2010); (shown as a red curve in Fig. B.1) along with the approximations by Fabian and Barcons (1992).

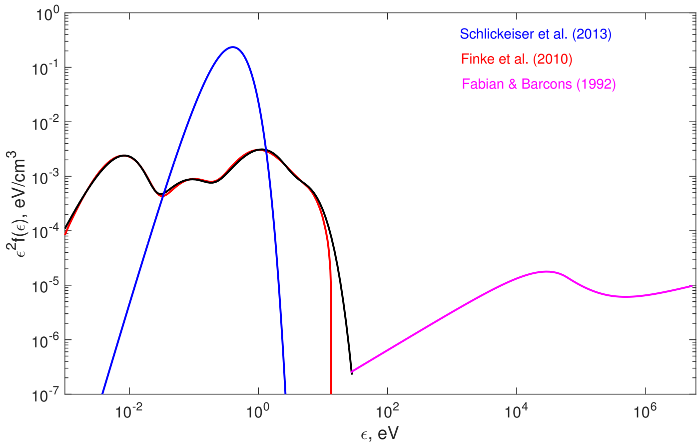

Fig. B.1 EBL energy-density spectrum for different models. Blue: the Wien-type distribution used by Schlickeiser et al. (2013); (see also Eq. B.10). Red: stellar radiation model by Finke et al. (2010) at redshift 0.2. Black: our analytical approximation for the red line (Appendix B.2). Magenta: empirical model of the X-ray background (Fabian and Barcons, 1992).

Electron-positron pairs produced by gamma-ray absorption will eventually loose their energy by Comptonization of the microwave background, unless plasma instabilities drain their energy more rapidly. In any case, the mean-free path for Comptonization,

$$\lambda_{\rm IC} \simeq (75\ \mathrm{kpc}) \left( \frac{10^7}{\gamma} \right) \tag{B.11}$$

provides the upper limit for the pathlength along which the pair beam can build up. A 10 TeV gamma ray produces electrons and positron with mean energy 5 TeV, or $\gamma = 10^7$, and reradiates gamma-rays with energies around 10 GeV that should be easily observable with the Fermi-LAT. We use the pathlength $\lambda = \lambda_{\rm IC}(\gamma = 10^7)$ to calculate the pair spectrum.

Fig. B.2 shows the pair spectrum at distance 50 Mpc from a blazar resulting from interactions of high-energy gamma rays with a spectrum following Eq. (B.1) and low-energy EBL photons (Fabian and Barcons, 1992; Finke et al., 2010). The total number density of pairs is about $3 \times 10^{-22}$ cm$^{-3}$. The red and the blue curve illustrate results of our calculation (Eq. B.10), while the black one shows the approximation found by Schlickeiser et al. (2012a), that is close to our results only beyond the peak at $\gamma > 10^6$. The rising flank of the black curve at $\gamma \approx 10^{4.7}$ is much steeper and it does not show a second peak at lower energies. It is clear that the peak of the pair distribution at $\gamma \approx 5 \times 10^2$ results from the cosmic background radiation, which was not included in the model by Schlickeiser et al. (2013). In Appendix

B.3, we give an analytical approximation for the red curve in Fig. B.2 used in this work to evaluate the linear growth rate of the electrostatic instability.

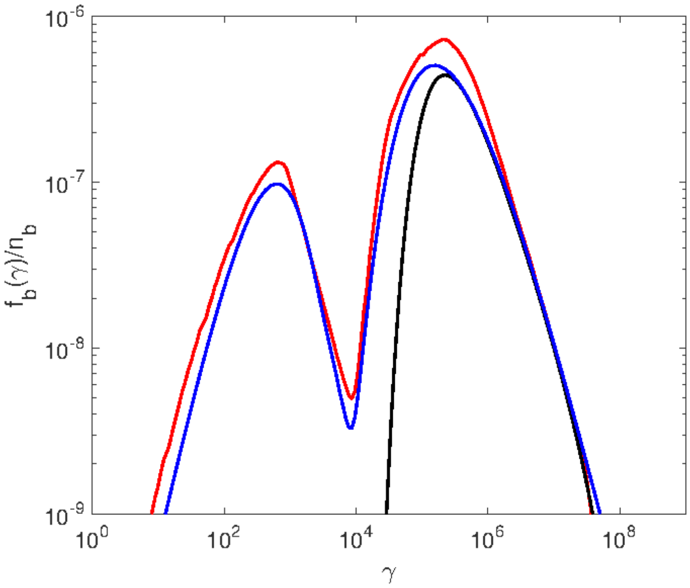

Fig. B.2 Normalized pair spectrum at the distance 50 Mpc from the source. Red: numerical solution of Eq. (B.9) using the Finke model model and the CXB fit. Blue: our approximation for the red curve (Eq. (B.13)). Black: pair spectrum for the EBL approximation by Schlickeiser et al. (2013).

## B.2 Approximation for the stellar radiation spectrum at redshift 0.2

We approximate the energy spectrum of stellar radiation at redshift $z = 0.2$ by

$$f(\varepsilon) = \sum_{i=1}^{4} \frac{N_i}{\Gamma(1+q_i) k_B T_i} \left( \frac{\varepsilon}{k_B T_i} \right)^{q_i} \exp\left( -\frac{\varepsilon}{k_B T_i} \right), \tag{B.12}$$

where $\varepsilon$ is in eV, $f(\varepsilon)$ in eV$^{-1}$ cm$^{-3}$. Other parameters are listed in Table B.1.

Table B.1 Fitting parameters for the approximation Eq. (B.12)

| $i$ | $q_i$ | $k_BT_i$, eV | $N_i$, cm$^{-3}$ |
|---|---|---|---|
| 1 | 0.5 | $3.3\times10^{-3}$ | 0.78 |
| 2 | 0 | 0.53 | 0.01 |
| 3 | 0 | 0.04 | 0.035 |
| 4 | 0 | 2 | 0.0007 |

## B.3 Approximation for the pair distribution function

The pair distribution function can be approximated as

$$\frac{f_b(\gamma)}{n_b} = N_1\left(\frac{\gamma}{\gamma_1}\right)^{-b_1}\exp\left(-\sqrt{\frac{\gamma_1}{\gamma}}\right)\Theta[(\gamma-6\times10^3)(10^8-\gamma)] + N_2\left(\frac{\gamma}{\gamma_2}\right)^{b_2}\exp\left(-\left(\frac{\gamma}{\gamma_2}\right)^{0.7}\right) + N_3\left(\frac{\gamma}{\gamma_3}\right)^{b_3}\exp\left(-\frac{\gamma}{\gamma_3}\right), \quad \text{(B.13)}$$

where the fitting parameters are summarized in Table B.2.

The approximation used by Schlickeiser et al. (2012a) is

$$\frac{f_b(\gamma)}{n_b} \approx \frac{\gamma^{1/2-\alpha}}{\gamma_c^{3/2-\alpha}\Gamma(\alpha-3/2)}\frac{\exp(-\gamma_c/\gamma)}{1+(\gamma/\gamma_b)^{3/2}}, \quad \text{(B.14)}$$

where $\gamma_c = M_c/\ln\tau_0$, $\gamma_b = M_c\tau_0^{2/3}/2^{7/3}$, $\tau_0 = 10^3$, $M_c = 2\times10^6$, $\alpha = 1.8$.

Table B.2 Fitting parameters for the approximation Eq. (B.13)

| $i$ | $b_i$ | $\gamma_i$ | $N_i$ |
|---|---|---|---|
| 1 | 1.6 | $10^{6.2}$ | $3\times10^{-7}$ |
| 2 | 1.8 | $10^{2.2}$ | $1.1\times10^{-7}$ |
| 3 | 1.8 | $10^{3.2}$ | $1.8\times10^{-8}$ |

# Publications

---

Publications related to this thesis:

- "Plasma effects on relativistic pair beams from TeV blazars: PIC simulations and analytical predictions."Rafighi et al. (2017).
- "The electrostatic instability for realistic pair distributions in Blazar/EBL cascades."Vafin et al. (2018).

Parts of this thesis and the appendices have previously been published. Reprinted (adapted) with permission from (Vafin et al. (2018)) - Published by The Astrophysical Journal.

# Acknowledgements

First and foremost, I would like to express my immense appreciation to my supervisor, Prof. Dr. Martin Karl Wilhelm Pohl for all the years of his guidance and support during my PhD studies. This thesis would not have been possible without his patience, kindness, constructive feedbacks and advices. I would also like to thank Prof. Dr. Wolf-Rainer Hamann for his continuous support ever since I moved to Germany, not only for the scientific issues and challenges but also for his real life advices.

Special appreciation is acknowledged to Dr. Sergei Vafin for his great feedbacks and collaborations regarding our common publications, for reviewing the thesis and being a friend. Most of the analytical work in our publications were done by Sergei which was the base of all simulations I performed. Also I would like to extend my sincere gratitude to the reviewers Prof. Dieter Horns & Prof. Christoph Pfrommer, the chairman Prof. Stephan Geier and committee members Prof. Wolf-Rainer Hamann and Dr. Lida Oskinova.

For almost the first two years of my PhD studies, my wife and I had to live in two different continents but our hearts were always close. Words can not express my appreciation to my wife Maryam. My heartfelt appreciation to her for being there for me all these years; in tough times and happy times. Her presence has always been the utmost comforting.

I would also like to take this opportunity to express my gratitude to my office mates Dr. Robert Rettig and Dr. Volkmar Wieland for the great discussions and memorable days we shared. My appreciation extends to all the colleagues in Potsdam University and DESY specially, Dr. Reinaldo Santos de Lima, Dr. Maria del Valle, Dr. Helge Todt, Ines Tietgen, Alina Wilhelm, Clemens Hoischen,Yousof Mardoukhi, Dr. Vahid Rezanejad and so many more. I am very thankful to Andrea Brockhaus for all the years of support during my PhD studies. It was not feasible to overcome the bureaucratic issues without her.

I thank my friends and family and beloved ones, specially my sisters and my parents who have been passionately supporting me throughout my life.